

Inverse Modelling at Recovery Glacier, Antarctica

Christine Eis

June 12, 2019

University of Bremen

Department of Geosciences

PhD Thesis

**Inverse Modelling at Recovery Glacier,
Antarctica**

Christine Eis

June 12, 2019

- 1. Reviewer* **Prof. Dr. Angelika Humbert**
Alfred Wegener Institute, Helmholtz Centre for Polar- and
Marine Research
University of Bremen, Department of Geosciences
- 2. Reviewer* **Prof. Dr. Eberhard Bänsch**

Friedrich-Alexander University Erlangen-Nürnberg, Depart-
ment of Mathematics
- Supervisor* **Prof. Dr. Angelika Humbert**

Christine Eis

Inverse Modelling at Recovery Glacier, Antarctica

PhD Thesis, June 12, 2019

Reviewers: Prof. Dr. Angelika Humbert and Prof. Dr. Eberhard Bänsch

Supervisor: Prof. Dr. Angelika Humbert

University of Bremen

Department of Geosciences

Abstract

Recovery Glacier flowing into Filchner Ice Shelf drains about 8 % of the East Antarctic Ice Sheet with velocities up to about 900 m a^{-1} . Its future ice loss will probably be the largest of the East Antarctic Ice Sheet over the next millennia. The evolution of Recovery Glacier can be predicted by models solving the equations of the momentum and mass balance. Ice dynamics are fundamentally driven by bedrock conditions underneath the ice, but these can not simply be measured yet. Several lakes are expected to exist underneath the onset of Recovery Glacier enhancing its flow. This thesis utilizes an inverse method implemented in the Ice Sheet System Model (ISSM) to acquire basal parameters. The technique minimizes the difference between horizontal surface velocities derived from remote sensing and computed by the model. A sensitivity analysis is carried out to capture the influence of a couple of parameters on the inversion of basal conditions. This includes the viscosity, initial values and lower boundaries of the controlled parameter as well as the quality of the observed velocities.

False values in the velocity field can lead to uncertainties in basal parameters because these are fitted to the observed velocities. In order to improve the quality of the input velocity field, it is necessary to remove false values in the remote sensing derived data and to fill gaps using a suitable interpolation method. This thesis presents a filtering method with three processing steps. It detects smooth segments, removes outliers using the median and constraints fluctuations of the flow direction. The approach removes false data points successfully, while preserving structures like shear margins and keeping 83 % of the data. Data gaps are filled comparing four different interpolation methods: linear interpolation, natural neighbor interpolation, minimum curvature with tension, and Kriging. By examining advantages and disadvantages of the approaches, the natural neighbor interpolation turns out to be the best method to fill the gaps in the Recovery Glacier velocity field.

The sensitivity analysis shows that the influence of filtering outliers and interpolation on basal parameters derived from inverse modelling is large at least near Recovery Glaciers grounding line and far upstream. Furthermore, the ice has to be relatively stiff to match the observed velocities best. The inversion is robust in the onset area of Recovery Glacier for all parameter sets, wherefore the results are used to complete the picture of Recovery Glaciers base.

Zusammenfassung

Der Recovery Gletscher, der in das Filchner Eisschelf fließt, drainiert etwa 8% des Ostantarktischen Eisschildes mit Geschwindigkeiten bis zu 900 m a^{-1} . In den nächsten Jahrtausenden wird vermutlich kein anderer Gletscher des Ostantarktischen Eisschildes so viel Masse verlieren wie dieser. Die Entwicklung des Recovery Gletschers kann von Modellen vorhergesagt werden, welche die Gleichungen der Impuls- und Massebilanz lösen. Die Dynamik des Eises wird fundamental durch Bedingungen am Felsbett unter dem Eis gesteuert, jedoch können diese bisher nicht einfach gemessen werden. In dieser Dissertation wird eine inverse Methode benutzt, um die notwendigen Parameter zu bestimmen. Diese ist in das Ice Sheet System Model (ISSM) implementiert. Die Methode minimiert die Differenz zwischen beobachteten und simulierten horizontalen Oberflächengeschwindigkeiten, welche durch Fernerkundung gewonnen bzw. vom Modell berechnet wurden. Um den Einfluss verschiedener Parameter auf die Invertierung von basalen Bedingungen zu untersuchen, wird eine Sensitivitätsanalyse durchgeführt. Diese untersucht die Abhängigkeit von der Viskosität, Startwerte und untere Grenzen des optimierten Parameters sowie die Qualität der beobachteten Geschwindigkeiten.

Fehlerhafte Geschwindigkeiten können zu Ungenauigkeiten in den basalen Parametern führen, da diese an die beobachteten Geschwindigkeiten angepasst werden. Um die Qualität des beobachteten Geschwindigkeitsfeldes zu verbessern, ist es notwendig falsche Werte in den aus Fernerkundung gewonnenen Daten zu entfernen und Lücken durch Verwendung von geeigneten Interpolationsverfahren zu füllen. Diese Dissertation stellt eine 3-Schritt-Filtermethode vor. Der Filter detektiert glatte Segmente, entfernt Ausreißer durch Abgleich mit dem Median und begrenzt die Änderung der Fließrichtung. Der Ansatz entfernt fehlerhafte Datenpunkte erfolgreich, während Strukturen, wie z.B. Scherzonen sowie insgesamt 83 % der Daten erhalten bleiben. Die Datenlücken werden vergleichend durch vier verschiedene Interpolationsverfahren gefüllt: lineare Interpolation, Voronoi Interpolation, minimale Krümmung mit Spannung und Kriging. Bei der Untersuchung von Vor- und Nachteilen der Verfahren, stellt sich die Voronoi Interpolation als am geeignetsten heraus um Lücken im Geschwindigkeitsfeld des Recovery Gletschers zu füllen.

Die Sensitivitätsanalyse zeigt, dass der Einfluss des Filters und der Interpolation zumindest nahe der Aufsatzlinie des Recovery Gletschers und in vorgelagerten Regionen groß ist. Weiterhin muss das Eis relativ steif angenommen werden um die beobachteten Geschwindigkeiten am besten wiederzugeben. Alle Parametersätze führen in der Region, in der die subglazialen Seen des Recovery Gletschers vermutet werden, zu ähnlichen basalen Gegebenheiten. Die Ergebnisse sind daher eine verlässliche Informationsbasis, um das Bild vom Bett des Recovery Gletschers zu vervollständigen.

Contents

Abstract	iv
Contents	vi
List of Abbreviations	ix
List of Symbols	xi
1 Introduction	1
1.1 The Antarctic Ice Sheet under Changing Climate	1
1.2 Thesis Outline	3
2 Recovery Glacier	4
2.1 Introduction	4
2.2 Previous Studies	5
2.3 Thesis Objectives	7
3 Ice Surface Velocities	8
3.1 Sensor Types	8
3.2 Deriving Velocities from Satellite Data	9
3.3 Velocity Data of Recovery Glacier	10
3.4 Postprocessing of Velocities - Preprocessing for Inverse Modelling . .	10
3.4.1 Removing Erroneous Values	10
3.4.2 Filling Gaps	11
4 Modelling Ice Flow	13
4.1 Fundamental Variables of Continuum Mechanics	13
4.2 Mass Balance	14
4.2.1 Mass Balance Boundary Conditions	15
4.3 Ice Thickness	15
4.4 Balance of Angular Momentum	15
4.5 Balance of Linear Momentum	16
4.5.1 Momentum Balance Boundary Conditions and Basal Friction .	17
4.6 Blatter/Pattyn's Higher-Order Model	19
4.7 Ice Sheet System Model	20

5	Inverse Problems	21
5.1	General Case	21
5.1.1	From Direct Problem to Minimization	21
5.1.2	Setting up a Minimization Problem	22
5.1.3	Calculation of the Cost Function Gradient	23
5.1.4	Solving the Minimization Problem	24
5.2	Special Case: Ice Dynamics	26
5.3	Inverse Methods in Glaciology	31
6	A Combined Approach for Filtering Ice Surface Velocity Fields Derived from Remote Sensing Methods	33
6.1	Introduction	35
6.2	Materials and Methods	37
6.2.1	Description of the Filter	37
6.3	Results	39
6.3.1	Artificial Flow Field	39
6.3.2	Filter Parameter Sensitivity Tests	39
6.3.3	Recovery Glacier	41
6.3.4	Other Locations	47
6.4	Discussion	53
6.5	Conclusions	55
6.6	Appendix	56
6.6.1	Intensity Offset Tracking	56
6.6.2	Filter Parameter Sensitivity Tests	58
7	An Evaluation of Gap Filling Methods for Glacier Surface Velocity Fields Derived from Remote Sensing	61
7.1	Introduction	63
7.2	Materials and Methods	65
7.2.1	A Velocity Field with Artificial Gaps	66
7.2.2	Recovery Glacier	66
7.2.3	Linear Interpolation	68
7.2.4	Minimum Curvature with Tension	69
7.2.5	Natural Neighbor Interpolation	70
7.2.6	Kriging	70
7.2.7	Quality Measures	73
7.3	Results	73
7.3.1	Application to a Velocity Field with Artificial Gaps	73
7.3.2	Application to Recovery Glacier	74
7.4	Discussion	79
7.5	Conclusions	83

8 Basal Properties of Recovery Glacier from Inverse Modelling and Observations	85
8.1 Introduction	87
8.2 The Modelling Approach	90
8.2.1 Balance Equations	90
8.2.2 Boundary Conditions	91
8.2.3 Constitutive Relation	92
8.2.4 Inversion	93
8.3 Model Setup	94
8.3.1 Numerics	95
8.3.2 Experimental Setups	95
8.4 Results	96
8.4.1 Optimal Parameter Choice and Sensitivity Tests	96
8.4.2 Basal Drag and Friction Coefficients	98
8.4.3 Basal drag, driving stress and basal sliding	100
8.5 Discussion	103
8.6 Conclusions	107
8.7 Appendix	108
8.7.1 Effect of Preprocessing of Remote Sensing Data for Inverse Modelling	108
8.7.2 Sensitivity to Enhancement Factor and Inversion Parameters	108
8.7.3 Effective Normal Pressure	109
9 Conclusion	111
9.1 Achievements	111
9.2 Outlook	112
Bibliography	114
List of Figures	124
List of Tables	126
Affirmation in Lieu of an Oath	127

List of Abbreviations

Abbreviation	Description
AIS	Antarctic Ice Sheet
ALOS PALSAR-2	Advances Land Observing Satellite Phased Array type L-band Synthetic Aperture Radar Mission
approx.	approximately
BFGS	Broyden-Fletcher-Goldfarb-Shanno update formula
BLMVM	Bounded-constrained Limited-Memory Variable-Metric method
CG	Conjugate Gradient method
DEM	Digital Elevation Model
DLR	German Aerospace Center
EAIS	East Antarctic Ice Sheet
EPSG	European Petroleum Survey Group Geodesy
FEM	Finite Elements Method
GNSS	Global Navigation Satellite System
HOM	Higher-Order Model
ICESat	Ice, Cloud and Land Elevation Satellite
InSAR	Interferometric Synthetic Aperture Radar
IPCC	Intergovernmental Panel on Climate Change
ISSM	Ice Sheet System Model
IW	Interferometric Wide
KKT	Karush-Kuhn-Tucker conditions
LinInt	Linear Interpolation
LMVM	Limited-Memory Variable-Metric method
MEaSURES	Making Earth System Data Records for Use in Research Environments

Abbreviation	Description
MinCurv	Minimum Curvature with Tension
NatInt	Natural Neighbor Interpolation
NEGIS	North East Greenland Ice Stream
NiSAR	NASA-ISRO Synthetic Aperture Radar Mission
PETSc	Portable, Extensible Toolkit for Scientific Computation
RAMP	RADARSAT-1 Antarctic Mapping Project
RCP	Representative Concentration Pathways
RG	Recovery Glacier
SAR	Synthetic Aperture Radar
SIA	Shallow Ice Approximation
SSA	Shallow Shelf Approximation
SLC	Single Look Complex
TAO	Toolkit for Advanced Optimization
TOPS	Terrain Observation with Progressive Scans
WAIS	West Antarctic Ice Sheet
WGS 84	World Geodetic System 1984
WRCP	World Climate Research Programme

List of Symbols

Symbol	Description	Unit
σ	Cauchy stress tensor	Pa
σ'	deviatoric stress tensor	Pa
σ'_e	effective deviatoric stress	Pa
p	pressure	Pa
t	time	s
$\dot{\epsilon}$	strain rate tensor	s^{-1}
$\dot{\epsilon}_e$	effective strain rate	s^{-1}
$\mathbf{v} = (v_x, v_y, v_z)$	velocity	$m a^{-1}$
Ω	angular velocity	rad
g	Earth gravity constant	$m s^{-2}$
\mathbf{g}	Earth gravity acceleration	$m s^{-2}$
T	temperature	K
W	microscopic water content	1
E	enhancement factor	1
p_a	atmospheric pressure	Pa
s	glacier surface	m
b	glacier base	m
$H = s - b$	ice thickness	m
ρ	ice density	$kg m^{-3}$
ρ_w	sea water density	$kg m^{-3}$
p_i	ice overburden pressure	Pa
p_w	water pressure	Pa
a_s	surface accumulation/ablation	$m s^{-1}$ ice equivalent
a_b	basal melting/freezing	$m s^{-1}$ ice equivalent
p, q, r, s	exponents of sliding law	1
N	basal effective pressure	Pa
k	basal friction parameter	$Pa^{(1-r)/2} s^{s/2} m^{-s/2}$
α	basal friction parameter	$kg^{1/2} m^{-1/2} s^{-1}$

Symbol	Description	Unit
τ_b	stress vector along basal tangential plane	Pa
v_b	basal velocity	$m s^{-1}$
n	stress exponent	1
A	rate factor	$Pa^{-n} s^{-1}$
B	ice viscosity parameter	$Pa s^{1/n}$
μ	viscosity	$Pa s$
τ_d	driving stress	Pa
\mathbb{R}	space of real numbers	
\mathbb{R}_+^*	space of strictly positive real numbers	
\mathcal{T}^n	tensor space of order n	
Ω	subdomain in 2D or 3D space	
\mathbf{x}	position vector in 2D or 3D space	
A^T	transpose of matrix A	
\mathcal{P}	parameter space	
\mathcal{Y}	solution space	
\mathcal{Y}_{obs}	space of observations	
\mathbf{y}_{obs}	observation	
\mathcal{V}	adjoint space	
Γ_b	basal boundary	
Γ_s	surface boundary	
Γ_u	Dirichlet boundary condition	
Γ_σ	Neumann boundary condition	

Introduction

” *Over the last two decades, the Greenland and Antarctic ice sheets have been losing mass, glaciers have continued to shrink almost worldwide, and Arctic sea ice and Northern Hemisphere spring snow cover have continued to decrease in extent.*

— IPCC REPORT

1.1 The Antarctic Ice Sheet under Changing Climate

The Antarctic Ice Sheet (AIS) is the largest coherent body of ice in the world with a volume of approx. $27 \times 10^6 \text{ km}^3$ and thereby also the largest reservoir of fresh water (Fretwell et al., 2013a). It corresponds to 58.3 m of sea level equivalent (Vaughan, Comiso, et al., 2013). The term *ice sheet* comes from its very thin geometry, which is in the first moment hard to envisage because it has a thickness of several kilometers. Nonetheless, it has a width-to-height ratio of about 1800 (Faria et al., 2018). For comparison: a typical A4 paper sheet has a width-to-height ratio of about 3000, hence they are in the same order of magnitude. The AIS has surface elevations up to approx. 4000 m (Slater et al., 2018) and therefore represents topographic barriers to atmospheric circulations and shows regional climate conditions, e.g. katabatic winds (King and Turner, 1997; Parish and Bromwich, 1987). The Antarctic Plateau is not only the coldest, but also one of the driest places on Earth with precipitation rates of less than 7 cm per year (Vaughan, Bamber, et al., 1999). Although this continent is one of the most remote parts of the world for human activities, it is strongly coupled to the climate system because the ice sheet interacts with atmosphere and ocean on a global scale (e.g. Bamber et al., 2007; Oerlemans, 2001). Therefore, the AIS is sensitive to climate change like all other components of the cryosphere and hence IPCC (2014) found that the ice mass loss from the AIS increased during the last decades. The WCRP Global Sea Level Budget Group (2018) stated a mean sea level contribution of $0.42 \pm 0.06 \text{ mm a}^{-1}$ since 2005, which is about 12 % of the total global

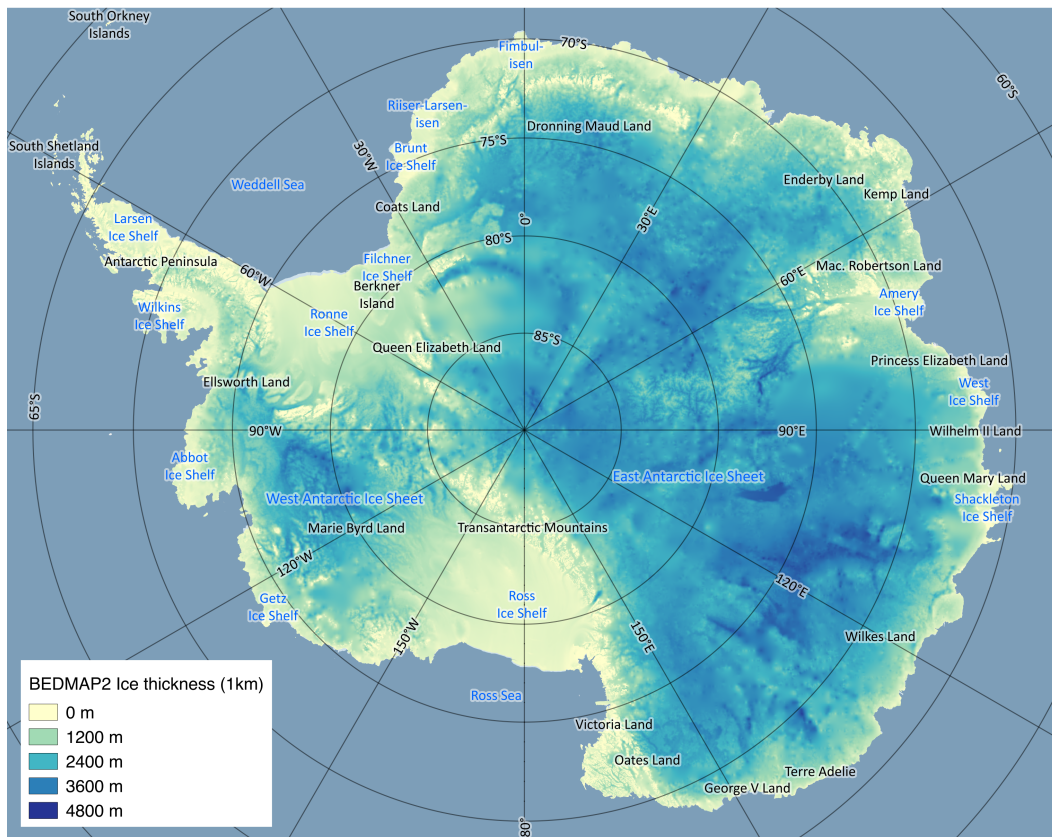


Fig. 1.1: Map of Antarctica with ice thickness data from Bedmap2 (Fretwell et al., 2013a).

mean sea level. In the 1993 to present time period they calculated a contribution of only 8 % ($0.25 \pm 0.1 \text{ mm a}^{-1}$). DeConto and Pollard (2016) demonstrated that the AIS could contribute to sea-level rise by more than 1 m until the end of the century and more than 15 m until 2500 under a climate scenario with stable emissions (RCP8.5). Furthermore, Darelius et al. (2016) and Rintoul et al. (2016) showed that even in some regions of the East Antarctic Ice Sheet (EAIS), which is believed to be stable since 14 million years, e.g. at Filchner Ice Shelf (Recovery Glacier basin) and Totten Ice Shelf, an influx of warm ocean water occurs, which may lead to a response in form of mass loss.

In turn, ice sheets have a fundamental sustainable impact on physical, biological and social systems (Vaughan, Comiso, et al., 2013). They affect e.g. oceanic and atmospheric temperature, global ocean circulation as well as marine ecosystems and global biogeochemical cycles (King and Turner, 1997; Schwerdtfeger, 1984). Therefore, a profound in-depth knowledge of all parts of glacier and ice sheet dynamics is absolutely essential. It is the basis of all further considerations, from ice sheet evolution projections over sea level change predictions to risk management in coastal regions (Vaughan, Comiso, et al., 2013).

1.2 Thesis Outline

This thesis investigates the basal conditions of a major ice stream of the EAIS, Recovery Glacier. A summary of previous studies of the Recovery catchment area is given in Chapter 2. The local conditions are introduced and it is argued why this region comes more and more into scientific focus. Chapter 3 outlines the application of remote sensing to derive ice surface velocities. It presents the most important instruments and methods as well as which data of Recovery Glacier are used to derive a fundamental parameter of glacier flow: basal friction. Which meaning this parameter has, can be understood by deriving the equations of ice dynamics, what is done in Chapter 4. This section also introduces the later used Higher-Order approximation as well as the Ice Sheet System Model (ISSM). As the background of the basal friction is clear, the question rises how to acquire information about basal conditions, since a simple measurement is not possible. The solution is presented in Chapter 5 by establishing an inverse problem minimizing the difference between modelled and observed surface velocities. First, the general inversion theory including cost functions, the Lagrangian, adjoint equations, and the steepest descent algorithm is introduced. After that, the theory is applied to the case of basal friction and different solution strategies are presented. Chapter 6 deals with the elimination of false values in observed surface velocities. A three step filtering procedure is tested and applied to Recovery Glacier's velocities in order to improve its quality. Existing data gaps are filled in Chapter 7. Four interpolation methods are analyzed to investigate their usefulness in application to surface velocity fields. Subsequent to these processing steps, the inversion of basal friction is carried out in Chapter 8. This includes a sensitivity analysis, which examines the influence of parameters of ice dynamics and inversion as well as the quality of the velocity field fed into the ice flow model. Chapter 9 summarizes the results and gives perspective ideas.

Recovery Glacier

” *I seemed to vow to myself that some day I would go to the region of ice and snow and go on and on till I came to one of the poles of the earth, the end of the axis upon which this great round ball turns.*

— ERNEST SHACKLETON
Polar Explorer

2.1 Introduction

Filchner-Ronne Ice Shelf is located at the confluence of WAIS and EAIS and is the second largest ice shelf after Ross Ice Shelf. It can be seen as two parts, Ronne Ice Shelf in the west and Filchner Ice Shelf in the east divided by Berkner Island. Filchner Ice Shelf is fed by 4 tributaries: Bailey Ice Stream, Slessor Glacier, Recovery Glacier, and Support Force Glacier (Figure 2.1). The drainage basin of Recovery Glacier is situated in Queen Maud Land, East Antarctica and has an area of about 996000 km^2 , which is about 8 % of the area of the EAIS (Rignot, Bamber, et al., 2008). The main ice stream of this basin is Recovery Glacier flowing into Filchner Ice Shelf by contributing 58 % of its total influx (Bell et al., 2007). This huge ice stream borders in the north the Shackleton Mountain Range overlooking Recovery Glacier with 400 m high cliffs (Fogwill et al., 2004). At the grounding line it is about 30 km wide and gets in contrast to other ice streams much wider in the upstream area, thus it has the shape of a funnel (Jezek, 1999). Recovery Glacier reaches far into EAIS with an impressive length of almost 1000 km. The ice stream has two tributary branches in the south, Ramp and Blackwall glaciers. The first one is approx. 270 km long, is about 250 km away from the grounding line, and reaches velocities of up to about 140 m a^{-1} . It is to a large extent crevasse free, which gives the impression that shear stresses occur in particular at the margins. Blackwall Glacier is located only 35 km upstream of the grounding line of Recovery Glacier and is less active (Jezek, Sohn, et al., 1998). The main trunk of Recovery Glacier itself is highly crevassed in many regions, which is assumed to be due to strong variations in the topography at

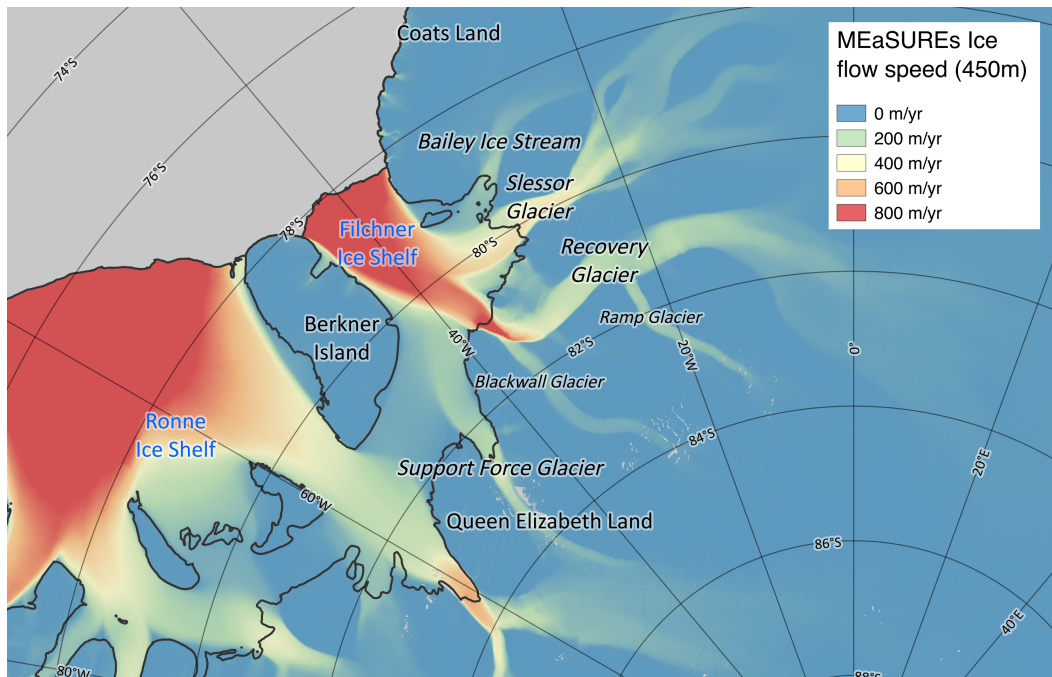


Fig. 2.1: Map of the Filchner ice shelf region with MEaSUREs flow speeds (Rignot et al., 2017).

the bedrock (Jezek, 1999). Recovery Glacier has a large fast flowing part reaching velocities up to approx. 870 m a^{-1} (Floricioiu et al., 2014).

2.2 Previous Studies

The first exploration of the Recovery Glacier region was in 1957 during the Commonwealth Trans-Antarctic Expedition (Lister and Pratt, 1959). For a long time it was one of the least known places on Earth because it was not covered by many satellites and also not further explored by expeditions (Bell et al., 2007). The first synthetic aperture radar (SAR) mapping of the region was available in 1997 as a result of the RADARSAT-1 Antarctic Mapping Project (RAMP) (Jezek, Floricioiu, et al., 2009). But the reason why Recovery Glacier came into the scientific focus, was mainly the alleged detection of subglacial lakes underneath the onset of the glacier by Bell et al. (2007), later called *Bell lakes*. Because of the presence of enhanced flow despite a low surface gradient, they supposed that these lakes have a high influence on the dynamics of the glacier leading to higher flow velocities downstream. In the following, a couple of studies investigated the region with respect to these subglacial lakes. B. Smith et al. (2009) used ICESat data from 2003 to 2008 and detected elevation changes on the AIS. By doing so, they proposed ten active lakes downstream of the previous detected Bell lakes. Le Brocq et al. (2008) suggested the presence of a large basin with water saturated deformable sediments in the Recovery region, which is fed by basal melt water. Based on ice penetrating

radar measurements, Langley et al. (2011) found only one of the Bell lakes water filled, while others were at a low stand maybe due to recent drainage events. The existence of the subglacial water system was confirmed by Fricker et al. (2014), who used data from ICESat and Operation IceBridge to investigate the activity of the Recovery lakes and found the system to be highly variable in short time scales. They also employed a simple model of subglacial hydrology to model flow paths between the lakes and found nine of them to be connected. During the ICEGRAV campaigns between 2010 and 2013 gravity, magnetic and ice penetrating radar measurements were carried out in the Recovery Glacier region and contributed, inter alia, to a better coverage of ice thickness and bedrock topography. Radar profiles acquired by these flights also suggest the existence of liquid water in two of the Bell lakes (Forsberg et al., 2018). Diez et al. (2018) used the new data to improve the bed topography map of the Recovery region. With these information they found that Recovery Glacier is controlled by its topography in the downstream area, whereas in the upstream area it is stronger controlled by variable basal conditions, fast flow is there supported by basal water. Another survey of ice thickness, ice structure and surface topography in the Recovery drainage basin was carried out in January 2014 (Humbert et al., 2018). The results of this campaign have led to doubt the existence of the Recovery lakes. Humbert et al. (2018) cannot find a proof for the presence of lakes at most of the suggested locations underneath Recovery Glacier. Therefore, it is not clear if subglacial lakes enhance the flow of the glacier or if there are other reasons for it. These findings improve the importance of studies on basal conditions and the dynamics of Recovery Glacier.

Golledge et al. (2017) stated that the largest part of ice loss from the EAIS in the future will likely come from the Recovery catchment area. This holds not only for this century, but also over subsequent millennia. Reasons for that mass loss may be the influx of warm deep ocean water into the sub-Filchner Ice Shelf cavity (Hellmer et al., 2012). This may cause a thinning of the ice shelf, which results in a decreased buttressing for the inflowing glaciers (Hellmer et al., 2012). Consequently, Recovery Glacier runs the risk of an acceleration, grounding line retreat and thus increased contribution to sea level rise. Therefore, the improvement of the understanding of ice dynamics especially in this vulnerable region is of paramount importance.

2.3 Thesis Objectives

This thesis takes up previous studies of the region by inspecting the conditions underneath Recovery Glacier from a modelling perspective. Thus, the main objective of this thesis is:

1. Deriving the spatial distribution of the basal friction coefficient in the Recovery catchment area by using an inverse method.

The inversion minimizes the misfit between modelled and observed velocities. Thus, remote sensing derived velocities serve as model input. False values in the observations can result in erroneous inverted basal conditions. Therefore, a second aim is:

2. Improvement of the quality of velocity fields derived from remote sensing by application of filtering and interpolation techniques.

Finally, it should be analyzed how strong the benefit of the processing steps is. The influence of the quality of the velocity input field and of other model parameters on the inversion results should be analyzed:

3. Conduct of a sensitivity analysis of the inversion of basal friction with regard to model parameters as well as quality of input surface velocities.

Ice Surface Velocities

“*What we’re able to do now is track the flow of the world’s ice from pole to pole and on every continent.*”

— **Ted Scambos**
Glaciologist

Surface velocities of glaciers can be acquired either by carrying out point measurements or by remote sensing. Point measurements of glacier velocity are sparse especially in remote parts of the world. They need the accomplishment of field campaigns under difficult weather conditions. For this purpose, in the past markers were installed on the glacier and their positions were surveyed over time (Cuffey and Paterson, 2010). With these information the displacement and therefore the surface velocity can be calculated (Cuffey and Paterson, 2010). Today, GPS antennas play this role, which are left on the glacier for a time period. However, comprehensive velocity fields can only derived by satellite remote sensing, thus this thesis focuses on this technique. The following sections give a short summary of instruments and methods used to calculate glacier velocities as well as introduce the velocity fields of Recovery Glacier utilized in the context of this thesis. It is further discussed how to handle gaps and false values in velocity fields. A detailed discourse on remote sensing and its application in glaciology can be found e.g. in Lubin and Massom (2006), Bamber (2007), and Campbell and Wynne (2011).

3.1 Sensor Types

There are basically two types of sensors used in glacier satellite remote sensing, whose images are processed in order to derive glacier velocities. They differ in the wavelength of the emitted signal send to the Earth surface, scattered back, and received from the antennas mounted on the satellite. On the one hand side there exist optical sensors using *visible* and *infra-red* wavebands, the other one uses the *microwave* part of the spectrum (Bamber, 2007). The first ones have the disadvantage that their images are effected by clouds and darkness. In polar regions, which are anyway not completely covered by many sensors because the inclination of

the orbit is often only around 80°, this worsens the temporal resolution significantly (Bamber, 2007). Conversely, microwave sensors can be used any time of the day, also in darkness. Additionally, clouds are unproblematic for them because they are invisible for these wavelengths (Bamber, 2007).

An advantage of visible and infra-red instruments is the long time series they provide. Landsat images are available already since 1972, however they are mostly used in mapping and monitoring variations in glacier extent (Bamber, 2007; Bolch et al., 2010; Pfeiffer et al., 2014; Wei et al., 2014). Indeed, images of visible sensors are also used to derive glacier surface velocities (Heid and Kääb, 2012b).

A great achievement was done by the development of a special microwave sensor: *synthetic aperture radar* (SAR). It records both phase and amplitude of the radar signal and therefore it is possible to simultaneously measure elevation and ice motion (Lubin and Massom, 2006). With the launch of ERS-1 in 1991 applications entered glaciology.

3.2 Deriving Velocities from Satellite Data

This section shortly presents the fundamentals of the most important methods used to derive surface velocity fields from satellite remote sensing data: feature tracking, InSAR, and speckle tracking.

Feature tracking uses features on the glacier (e.g. crevasses) to derive displacements. Therefore, two images with a time shift of some days are necessary. By mapping the location of the features and comparing them in the two images, the displacement can be calculated and thus also the ice velocity (Cuffey and Paterson, 2010). For this method the usage of both optical and radar sensor derived images is possible.

In featureless areas *Interferometric Synthetic Aperture Radar* (InSAR) can be applied, if the region is covered by SAR images. Ice movement returns in a shift in phase because of different return times of the transmitted radiation as a result of distance variation (Cuffey and Paterson, 2010). Thus, InSAR uses the phases of two SAR images from the same viewpoint to calculate their difference and thus produces an interferogram. With this information the displacement of the ice in view direction of the satellite can be derived (Bamber, 2007). By using images from intersecting orbits it is possible to calculate also the other velocity component (Cuffey and Paterson, 2010). Highest resolutions and accuracies of only a few $m a^{-1}$ can be achieved with InSAR (Joughin, B. Smith, Howat, Scambos, and Moon, 2010). However, interferometry often fails e.g. due to a too long repeat cycle (Joughin, 2002), surface melt (Cuffey and Paterson, 2010), meteorological conditioned noise, snowfall or winds (Strozzi et al., 2002).

However, there is an alternative to the InSAR technique, which has similarities with the feature tracking approach: *speckle* or *intensity offset tracking* (Strozzi et al., 2002;

Michel and Rignot, 1999; Gray, Mattar, Vachon, et al., 1998). A SAR image displays the intensity of the signal scattered back to the antenna. A main property of the signal received by a SAR system is speckle. It is a form of noise which arises from accumulated signals, which are scattered from the surface (Gupta, 2003). Speckle patterns can be correlated, thus the phases instead of the amplitudes (as with feature tracking) are correlated and features are not needed (Michel and Rignot, 1999; Gray, Mattar, Vachon, et al., 1998).

3.3 Velocity Data of Recovery Glacier

From August 2012 to December 2013 a TerraSAR-X campaign was carried out to derive a high resolution velocity field covering the entire Recovery Glacier two times. In this process, TerraSAR-X acquired data in left looking mode in intervals of eleven to 22 days. The German Aerospace Center (DLR) obtained in total 150 stripmap pairs with a size of $30 \times 45 \text{ km}^2$ (Floricioiu et al., 2014; Abdel Jaber, 2016) and used speckle tracking to derive the velocities. In the course of this work the velocity field will be further processed resulting in a velocity field with 6137×3074 data points with a grid spacing of 156 m in the Antarctic Polar Stereographic coordinate system (WGS 84 / EPSG:3031).

In order to cover the entire Recovery basin, the data set is completed by using the Making Earth System Data Records for Use in Research Environments (MEaSUREs) ice velocity map of Antarctica (Rignot et al., 2011b; Rignot et al., 2011c). This data set is used in every case where additional data are required. Nonetheless, this thesis focuses on the spatially higher resolved TerraSAR-X velocity data.

3.4 Postprocessing of Velocities - Preprocessing for Inverse Modelling

The remote sensing derived velocity fields can often not easily serve as input for models, because they contain errors and gaps. Dealing with these problems is discussed in detail in Sect. 6 and 7, wherefore this section only summarizes the most important aspects.

3.4.1 Removing Erroneous Values

Velocity fields often contain false values, also called outliers because they strongly deviate from surrounding data points. This differences can appear in form of both magnitude and direction of flow velocity. Reasons for such errors are manifold and

can occur in every processing stage described in Sect. 3.2. As an example, in the case of speckle tracking, low correlation between the speckle patterns of the two SAR images can lead to false displacements. Removing these outliers is essentially prior to modelling applications because these observations are used to fit models to reality. By feeding the model with a false picture of reality, it will not be able to reliably predict the future evolution. The present state is simply wrong and also small errors can propagate in further calculations. In order to avoid such effects, *filter* algorithms can be applied. By using this term, it has to be distinguished between the widely used meaning to replace values of data points by new values and the connotation used in this thesis: removing false values. With this meaning, the task of a filter reduces to the detection of false values. Determining new values can be done by another step in connection with filling gaps.

Detection of single false values is possible if they differ from surrounding data points with regard to its characteristics. Using such an approach, it is therefore necessary to define what surrounding points are. Often, a moving window is used to determine this subset. Afterwards, the characteristic, which should be inspected has to be calculated for the chosen subset, e.g. mean or median of the velocity magnitude in the subset of surrounding data points. How much a data point is allowed to deviate is generally defined by a threshold. Summarizing this, there are many steps which are adjustable and many parameters need to be defined, e.g. the size of a moving window and the threshold.

If there exist patches of false values, they can be detected by algorithms, which recognize patterns in the velocity field, which means areas including data points with similar attributes are collected. The subsequent procedure is basically the same as for single false values. False value patches differ in some characteristic from other patterns, e.g. in its size. With this, a threshold can be defined determining if a patch contains outliers.

Sect. 6 presents a filter combining three approaches, two of them rather detecting single false values, the other one detecting patches of outliers.

3.4.2 Filling Gaps

Removing false values in the velocity field results in gaps, i.e. locations where no velocity values exist. But there are also several other reason why gaps occur in remote sensing derived velocity fields. The most apparent one is that the region is not entirely covered by satellite images. Furthermore, failures in the processing chain can cause the lack of data. Specific reasons depend therefore on the method used to derive velocities from satellite data as well as on the data themselves. Feature tracking of images from optical sensors is e.g. not possible in cloud covered areas, what would cause gaps. However, the aim of this thesis is rather filling the gaps instead of inspecting their reasons. The question that rises is from where to get

data in gap positions. One possibility is to use velocities from other data sets, the other one is to estimate the velocities in gap positions. The latter approach is called interpolation and there exist several methods for doing so. Four of these methods, which may be suitable to fill gaps in velocity fields, are explained and tested in detail in Sect. 7.

Modelling Ice Flow

” *When you measure what you are speaking about and express it in numbers, you know something about it, but when you cannot express it in numbers your knowledge about is of a meagre and unsatisfactory kind.*

— WILLIAM THOMSON LORD KELVIN
Physicist

The dynamics of ice sheets and glaciers and therefore its future evolution is based on physical laws like the conservation of mass, momentum and energy. They are derived from continuum mechanics (see e.g. Liu (2002) and Hutter (1983) for an introduction) and complemented by constitutive equations (e.g. Glen’s flow law). The result is a system of partial differential equations bounded by initial and boundary conditions at all interfaces between the ice and its environment. Together with climate forcing the system of equations is utilized in models to predict the future development of glaciers and ice sheets.

A detailed derivation and description of the equations of ice dynamics can be found e.g. in Greve and Blatter (2009), Cuffey and Paterson (2010), and Hutter (1983). This chapter describes the basic equations of ice dynamics derived from continuum mechanics, the Full Stokes model as well as an approximation, Blatter/Pattyn’s Higher-Order model. An introduction of the Ice Sheet System Model (ISSM) follows, which is used for further computations.

4.1 Fundamental Variables of Continuum Mechanics

It is useful to introduce some fundamental variables of continuum mechanics at this point. The second-order tensor space is written as \mathcal{T}^2 . The *Cauchy stress tensor*

$\boldsymbol{\sigma} \in \mathcal{T}^2$ defines the state of stress at some point in the interior of a continuum and at its boundaries. With that the *pressure* is defined as

$$p = -\frac{1}{3}tr(\boldsymbol{\sigma}) \quad (4.1)$$

with the trace operator $tr(\cdot)$.

The *deviatoric stress tensor* $\boldsymbol{\sigma}' \in \mathcal{T}^2$ is a fraction of the Cauchy stress tensor:

$$\boldsymbol{\sigma} = \boldsymbol{\sigma}' - p\mathbf{I} \quad (4.2)$$

with the identity tensor $\mathbf{I} \in \mathcal{T}^2$.

The *strain-rate tensor* $\dot{\boldsymbol{\epsilon}} \in \mathcal{T}^2$ is defined as:

$$\dot{\boldsymbol{\epsilon}} = \left(\frac{1}{2} \left(\frac{\partial v_i}{\partial x_j} + \frac{\partial v_j}{\partial x_i} \right) \right)_{ij} \quad (4.3)$$

and describes the local rate-of-change of the materials deformation as a result of stress.

The *effective strain rate* and the *effective shear stress* are the second invariants of the their respective tensors, strain rate tensor and deviatoric stress tensor:

$$\dot{\epsilon}_e = \frac{1}{\sqrt{2}} \left(\sum_{i,j=1,\dots,3} \dot{\epsilon}_{ij}^2 \right)^{1/2} \quad (4.4)$$

$$\sigma'_e = \frac{1}{\sqrt{2}} \left(\sum_{i,j=1,\dots,3} \sigma'^2_{ij} \right)^{1/2} \quad (4.5)$$

4.2 Mass Balance

The law of *mass conservation* states that the mass of a closed system is constant over time. The local form reads:

Theorem 4.1 (Mass conservation). *Let $\Omega \subset \mathbb{R}^3$ be a material body of density $\rho : \Omega \times [0, \hat{t}] \rightarrow \mathbb{R}_+^*$ and velocity $\mathbf{v} : \Omega \times [0, \hat{t}] \rightarrow \mathbb{R}^3$ for a time frame $[0, \hat{t}]$. The mass conservation imposes:*

$$\forall \mathbf{x} \in \Omega \quad \forall t \in [0, \hat{t}], \quad \frac{d\rho}{dt} + \rho \nabla \cdot \mathbf{v} = 0 \quad (4.6)$$

Ice is usually assumed as *incompressible material*, what means that its volume stays constant for any applied pressure. This is not true for the entire ice sheet or glacier, because ice is more compact in deeper layers. However, strongest variations in ice

density occur in the upper 100 m of the ice column and influence the average over the entire ice column by maximal 2 % (Cuffey and Paterson, 2010). Therefore, the effect is neglected and with the condition of incompressibility the mass conservation (Eq. 4.6) reduces to:

$$\nabla \cdot \mathbf{v} = 0 \quad (4.7)$$

4.2.1 Mass Balance Boundary Conditions

The glaciers upper surface can be described by $s(x, y, t) - z = 0$ and the glaciers bed can be analogous described by $b(x, y, t) - z = 0$. Then the *kinematic boundary conditions* at the surface and at the base are:

$$\begin{aligned} \frac{\partial s}{\partial t} &= -v_x(s) \frac{\partial s}{\partial x} - v_y(s) \frac{\partial s}{\partial y} + v_z(s) + a_s \\ \frac{\partial b}{\partial t} &= -v_x(b) \frac{\partial b}{\partial x} - v_y(b) \frac{\partial b}{\partial y} + v_z(b) + a_b \end{aligned} \quad (4.8)$$

with surface velocities $v_i(s) = v_i(x, y, s(x, y))$, $i = x, y, z$, analogous base velocities, accumulation/ablation rate a_s and melting/freezing rate a_b .

4.3 Ice Thickness

The ice thickness evolution can be derived by vertical integration of Eq. 4.7 and application of the kinematic boundary conditions (Eq. 4.8):

$$\frac{\partial H}{\partial t} = -\frac{\partial}{\partial x} \int_s^b v_x dz - \frac{\partial}{\partial y} \int_s^b v_y dz + a_s - a_b \quad (4.9)$$

with ice thickness $H = s - b$.

4.4 Balance of Angular Momentum

The *conservation of angular momentum* states that the rate-of-change of angular momentum of some portion of a continuous body is equal to the total torque applied on it. Thus, Theorem 4.2 follows:

Theorem 4.2 (Balance of angular momentum). *Let $\Omega \subset \mathbb{R}^3$ be a material body and σ its Cauchy stress tensor. The balance of angular momentum imposes that the stress tensor is symmetric.*

$$\forall \mathbf{x} \in \Omega \forall t \in [0, \hat{t}], \sigma = \sigma^T \quad (4.10)$$

4.5 Balance of Linear Momentum

The local form of *linear momentum conservation* is the generalization of Newton's second law. It states that the time rate of change of the momentum of a body equals the sum of the forces acting on it and reads:

Theorem 4.3 (Balance of linear momentum). *Let $\Omega \subset \mathbb{R}^3$ be a material body of density $\rho : \Omega \times [0, \hat{t}] \rightarrow \mathbb{R}_+^*$, velocity $\mathbf{v} : \Omega \times [0, \hat{t}] \rightarrow \mathbb{R}^3$ and a body force $\rho \mathbf{b} : \Omega \times [0, \hat{t}] \rightarrow \mathbb{R}^3$ for a time frame $[0, \hat{t}]$. Let $\sigma : \Omega \times [0, \hat{t}] \rightarrow \mathcal{T}^2$ be the Cauchy stress tensor. The balance of linear momentum is:*

$$\forall \mathbf{x} \in \Omega \forall t \in [0, \hat{t}], \rho \frac{d\mathbf{v}}{dt} = \rho \left(\frac{\partial \mathbf{v}}{\partial t} + (\mathbf{v} \cdot \nabla) \mathbf{v} \right) = \rho \mathbf{b} + \nabla \cdot \sigma \quad (4.11)$$

The body forces acting on a glacier or ice sheet are the *gravitational force* $\rho \mathbf{g}$ and the *Coriolis force* $2\rho \boldsymbol{\Omega} \times \mathbf{v}$ with the angular velocity vector $\boldsymbol{\Omega}$ of the rotating reference frame. The momentum balance (Eq. 4.11) reads then:

$$\rho \left(\frac{\partial \mathbf{v}}{\partial t} + (\mathbf{v} \cdot \nabla) \mathbf{v} \right) = \nabla \cdot \sigma + \rho \mathbf{g} - 2\rho \boldsymbol{\Omega} \times \mathbf{v} \quad (4.12)$$

Hutter (1983) showed in a scaling analysis that the acceleration and inertia terms as well as the Coriolis force are negligible for glaciers and ice sheets. Therefore, the momentum balance (Eq. 4.12) reduces to:

$$0 = \nabla \cdot \sigma + \rho \mathbf{g} \quad (4.13)$$

Commonly ice is taken as *isotropic, incompressible viscous fluid* (Hooke, 2005) and therefore described by the following equation:

$$\sigma' = 2\mu \dot{\epsilon} \quad (4.14)$$

with the viscosity μ .

Theorem 4.4 (Full Stokes model). *Inserting Eq. 4.2 and 4.14 in the momentum balance (Eq. 4.13), the Full Stokes equations of ice flow follow:*

$$\begin{aligned} 2\nabla \cdot (\mu \dot{\epsilon}) - \nabla p + \rho \mathbf{g} &= \mathbf{0} \\ \nabla \cdot \mathbf{v} &= 0 \end{aligned} \quad (4.15)$$

These four equations contain the three velocity components $\mathbf{v} = (v_x, v_y, v_z)$, the pressure p and the viscosity μ as unknowns, therefore a *constitutive equation* is necessary. This should relate strain rate and stress and can be found in the widely used *Glen's flow law*, also called *Glen-Steinemann flow law* (Glen, 1953; Glen and Perutz, 1955; Steinemann, 1954):

$$\dot{\epsilon}_e = \left(\frac{\sigma'_e}{B} \right)^n \quad (4.16)$$

where n is the stress exponent, calculated from experiments as a value between 1.5 and 4.2, but usually taken as $n = 3$ (Cuffey and Paterson, 2010; Hooke, 2005). B is a viscosity parameter, which increases with ice stiffness. The relation was extended by Nye and Perutz (1957) to cover multiaxial states of stress resulting in *Glen-Nye flow law*:

$$\dot{\epsilon} = \frac{(\sigma'_e)^{n-1}}{B^n} \boldsymbol{\sigma}' = A(\sigma'_e)^{n-1} \boldsymbol{\sigma}' \quad (4.17)$$

A is the rate factor and was found to depend on temperature T and microscopic water content W . The relation neglects all other softening effects on the ice. Therefore, the flow law is further adapted using an Arrhenius equation (e.g. Gagliardini et al., 2013):

$$\mu = \frac{1}{2} A(T, W)^{-1/n} E^{-1/n} \dot{\epsilon}_e^{(1-n)/n} \quad (4.18)$$

where the *enhancement factor* E accounts for any softening due to other than thermodynamic factors.

4.5.1 Momentum Balance Boundary Conditions and Basal Friction

Boundary between ice and atmosphere

The boundary between ice and atmosphere is treated as a *free surface* because the atmospheric pressure p_a is negligible compared to the lithostatic pressure of ice.

$$\boldsymbol{\sigma} \cdot \mathbf{n} = -p_a \mathbf{n} \simeq 0 \quad (4.19)$$

Boundary between ice and water

Hydrostatic pressure p_w acts on the ice front, which can be described by

$$p_w = -\rho_w g z \quad (4.20)$$

with the density of the water ρ_w . Thus, the boundary condition at the ice-water interface is:

$$\boldsymbol{\sigma} \cdot \mathbf{n} = -p_w \mathbf{n} \quad (4.21)$$

Boundary between ice and bedrock

The interface between ice and bedrock is described by two boundary conditions. The first one is a Dirichlet boundary condition ensuring a *non-interpenetrating condition* between ice and bedrock:

$$\mathbf{v} \cdot \mathbf{n} = -a_b \quad (4.22)$$

This means that any motion perpendicular to the basal tangential plain is due to melting or freezing (a_b). The second one is a Neumann boundary condition which describes the *basal friction* and is also called *sliding law*. Often, a viscous relation between basal shear stress and basal speed is used (Cuffey and Paterson, 2010):

$$\|\mathbf{v}_b\| = k N^{-q} \|\boldsymbol{\tau}_b\|^p \quad (4.23)$$

with the vector norm $\|\cdot\|$, the velocity component tangential to the bedrock surface \mathbf{v}_b , the friction stress component tangential to the bedrock surface $\boldsymbol{\tau}_b$, positive constants k , q and p , and the effective pressure N at the base b . The effective pressure is a function of the ice overburden pressure p_i and the water pressure p_w and is defined as:

$$N = p_i - p_w = \rho g H + \rho_w g b \quad (4.24)$$

With the assumption of $p = 3$ and $q = 1$, this law gets a special case, *Weertman's relation* (Weertman, 1957):

$$\boldsymbol{\tau}_b = -k^2 N^r \|\mathbf{v}_b\|^{s-1} \mathbf{v}_b := -\alpha^2 \mathbf{v}_b \quad (4.25)$$

where $r = \frac{q}{p}$ and $s = \frac{1}{p}$. Later, it was shown that the relation also holds in more general cases for positive p and q (Cuffey and Paterson, 2010; Weertman and Birchfield, 1983). The parameter α depends on the bed roughness as well as on thermal and mechanical properties of the ice. It is not possible to measure k (and

thus also α) directly and even difficult to estimate its spatial distribution. However, it is a primal control on ice stream dynamics. Therefore, inverse methods (Ch. 5) are taken into account to adjust this parameter.

4.6 Blatter/Pattyn's Higher-Order Model

The Full Stokes model (Eq. 4.15) may be the most accurate model for ice dynamics, but it is computationally challenging because of large computational costs. Therefore, different approximations were developed for simplification, e.g. the shallow-ice or shallow-shelf approximations. This thesis is limited to the *Higher-Order model* (HOM) developed by Blatter (1995) and Pattyn (2003). In contrast to the Full Stokes equations the Higher-Order model is not a saddle point problem. Additionally, the vertical velocity and the horizontal velocities can be computed independently in this approach. Therefore, it is much less computational expensive than solving the Full Stokes model. For this purpose, two assumptions are necessary. The first one implies that the horizontal gradients of the vertical velocity are small compared to the vertical gradient of the horizontal velocities, which is indicated in a scaling analysis of Greve and Blatter (2009). The other assumption is that the variation in horizontal shear stress along the direction of shear is small compared to vertical changes of vertical stress, which means that the bridging effect (Van Der Veen and Whillans, 1989) is negligible.

Theorem 4.5 (Blatter/Pattyn's Higher-Order Model). *Under the following assumptions:*

- $\frac{\partial \sigma_{xz}}{\partial x} \ll \frac{\partial \sigma_{zz}}{\partial z}$ and $\frac{\partial \sigma_{yz}}{\partial y} \ll \frac{\partial \sigma_{zz}}{\partial z}$,
- $\frac{\partial v_z}{\partial x} \ll \frac{\partial v_x}{\partial z}$ and $\frac{\partial v_z}{\partial y} \ll \frac{\partial v_y}{\partial z}$

the Full Stokes model (Eq. 4.15) reduces to

$$\begin{aligned}
 \frac{\partial}{\partial x} \left(4\mu \frac{\partial v_x}{\partial x} + 2\mu \frac{\partial v_y}{\partial y} \right) + \frac{\partial}{\partial y} \left(\mu \frac{\partial v_x}{\partial y} + \mu \frac{\partial v_y}{\partial x} \right) + \frac{\partial}{\partial z} \left(\mu \frac{\partial v_x}{\partial z} \right) &= \rho g \frac{\partial s}{\partial x} \\
 \frac{\partial}{\partial x} \left(\mu \frac{\partial v_x}{\partial y} + \mu \frac{\partial v_y}{\partial x} \right) + \frac{\partial}{\partial y} \left(4\mu \frac{\partial v_y}{\partial y} + 2\mu \frac{\partial v_x}{\partial x} \right) + \frac{\partial}{\partial z} \left(\mu \frac{\partial v_y}{\partial z} \right) &= \rho g \frac{\partial s}{\partial y} \quad (4.26) \\
 v_z(x, y, z) &= v_z(x, y, b) - \int_{b(x,y)}^z \frac{\partial v_x}{\partial x} + \frac{\partial v_y}{\partial y} dz'
 \end{aligned}$$

4.7 Ice Sheet System Model

The *Ice Sheet System Model* is a massively parallelized numerical model of ice flow developed by Larour et al. (2012). It contains different models of ice dynamics: the Full Stokes model, the Blatter-Pattyn Higher-Order model, the shallow shelf approximation (SSA), and the shallow ice approximation (SIA). The model utilizes the Continuous Galerkin Finite Element Method for discretization of the ice flow equations, which allows for the use of unstructured meshes. It is thermomechanically coupled and uses FEM methods also to solve equations for evolving temperature and mass transport. ISSM relies on a static anisotropic adaptive mesh refinement and is therefore capable to run simulations on a continental scale with high resolution in interesting regions, like outlet glaciers, and coarse resolution in the interior of an ice sheet. The model has the capability for the inversion of basal friction. ISSM is written in C/C++, has a MATLAB user interface and is open source.

Inverse Problems

” *Nothing takes place in the world whose meaning is not that of some maximum or minimum.*

— **LEONHARD EULER**
Mathematician and Physicist

Constitutive equations come with many physical parameters, some of which are not known in real applications. If they can be measured in some way, there are often only some point measurements available. This lack of spatial (and temporal) resolution as well as large uncertainties makes them unusable for application as model input. Also measurements in laboratories are difficult and its reliability can be called into question because the scales are very different from those in reality.

At the same time, such parameters, which describe the initial state of the model, have a strong influence on ice sheet and glacier projections, especially on timescales of decades to centuries (Arthern and Gudmundsson, 2010). This section introduces the basic principles of inverse theory used in models like ISSM to estimate these parameters. Afterwards the special case of unknown basal parameters in ice dynamics is described and a summary of different solution strategies is given. Because Sect. 8 will discuss mainly the results of the inversion, more details of the underlying theory are given in this section.

5.1 General Case

5.1.1 From Direct Problem to Minimization

In a *direct problem*, an initial state and maybe other boundary conditions are given and model equations are solved to calculate a final state. This problem is also called *forward model* and can be described in the following way:

$$\mathbf{y} = F(\mathbf{p}) \tag{5.1}$$

where $\mathbf{y} \in \mathcal{Y}$ is the solution of the model equations $F : \mathcal{P} \rightarrow \mathcal{Y}$, which depend on the known parameter $\mathbf{p} \in \mathcal{P}$.

Unfortunately, in many applications the solution \mathbf{y} is observed instead of the parameter \mathbf{p} . The challenge is then to find parameters \mathbf{p} holding Eq. 5.1. This is called an *inverse problem* or *backward problem* and can be formulated as follows:

$$\mathbf{p} = F^{-1}(\mathbf{y}_{obs}) \quad (5.2)$$

with the observation of the solution \mathbf{y}_{obs} . Often, there is no possibility to simply run a model backwards meaning inverting the model equations because there is no explicit formulation of F^{-1} or the problem is *ill-posed*. Following Hadamard (1902), this means that

- a solution does not exist or
- a solution exists but is not unique or
- an unique solution exists but does not depend continuously on the data.

In many applications one of these criteria is fulfilled because the dimensions of \mathcal{Y} and \mathcal{P} are not the same, whereby the problem is either over-determined or under-determined.

An alternative is to formulate an *optimization problem* by minimizing the misfit between the observations \mathbf{y}_{obs} and modelled solution \mathbf{y} :

$$\min_{\mathbf{p} \in \mathcal{P}} \|F(\mathbf{p}) - \mathbf{y}_{obs}\| \quad (5.3)$$

The optimal parameter \mathbf{p} can then be determined by using an optimization algorithm, e.g. a steepest descent algorithm.

5.1.2 Setting up a Minimization Problem

We can write the model equations as follows:

$$F(\mathbf{y}, \mathbf{p}) = 0 \quad (5.4)$$

It is assumed that the direct problem 5.4 has a unique solution for any $\mathbf{p} \in \mathcal{P}$, which means that it is not an ill-posed problem. It is further assumed that there exists an operator $G : \mathcal{Y} \rightarrow \mathcal{Y}_{obs}$ with $G(\mathbf{y}) = \mathbf{y}_{obs}$ translating the model solution into the space of observations. This assumption takes care that \mathbf{y} and \mathbf{y}_{obs} are comparable. The basis of an optimization problem is the function which should be minimized,

called *cost function* or *objective*. Therefore, it is useful to define the cost function $j : \mathcal{Y} \rightarrow \mathbb{R}$:

$$j(\mathbf{y}) = \|G(\mathbf{y}) - \mathbf{y}_{obs}\| \quad (5.5)$$

$j(\mathbf{y}(\mathbf{p}))$ is then equivalent to another cost function $J : \mathcal{P} \rightarrow \mathbb{R}$ with

$$J(\mathbf{p}) = \|G(\mathbf{y}(\mathbf{p})) - \mathbf{y}_{obs}\| \quad (5.6)$$

Minimizing J means to search for the parameters \mathbf{p} such that the misfit between \mathbf{y} and \mathbf{y}_{obs} is minimal and \mathbf{y} fulfills the model equations. Thus, it is valid that

$$\min_{\mathbf{p} \in \mathcal{P}} J(\mathbf{p}) \Leftrightarrow \min_{\mathbf{p} \in \mathcal{P}, F(\mathbf{y}, \mathbf{p})=0} j(\mathbf{y}) \quad (5.7)$$

A *minimum* is defined in the following way:

Definition 5.1 (Local minimum). \mathbf{p}^* is a local minimum of J if and only if $\mathbf{p}^* \in \mathcal{P}$ and $\exists \epsilon > 0 : J(\mathbf{p}) \geq J(\mathbf{p}^*) \forall \mathbf{p} \in \mathcal{P} \cap B_\epsilon(\mathbf{p}^*)$ with $B_\epsilon(\mathbf{a}) = \{\mathbf{x} \in \mathbb{R}^n \mid \|\mathbf{x} - \mathbf{a}\| < \epsilon\}$.

Definition 5.2 (Global minimum). \mathbf{p}^* is a global minimum of J if and only if $\mathbf{p}^* \in \mathcal{P}$ and $J(\mathbf{p}) \geq J(\mathbf{p}^*) \forall \mathbf{p} \in \mathcal{P}$.

The minimum of the cost function can be found by an *optimization algorithm*, but this often needs the *gradient* of the cost function to solve the problem. E.g. steepest descent algorithms utilize this information to follow the steepest descending gradient to reach a minimum.

5.1.3 Calculation of the Cost Function Gradient

The following minimization problem is considered:

$$\min_{\mathbf{p} \in \mathcal{P}} j(\mathbf{y}) \text{ under the constraint } F(\mathbf{y}, \mathbf{p}) = \mathbf{0} \quad (5.8)$$

To calculate the gradient of the cost function it is useful to introduce the *Lagrangian*:

Definition 5.3 (Lagrangian). The Lagrangian of the minimization problem 5.8 is the functional $L : \mathcal{Y} \times \mathcal{V} \times \mathcal{P} \rightarrow \mathbb{R}$ with

$$L(\mathbf{y}, \boldsymbol{\lambda}, \mathbf{p}) = j(\mathbf{y}) + \boldsymbol{\lambda}F(\mathbf{y}, \mathbf{p}) \quad (5.9)$$

$\lambda \in \mathcal{V}$ is called *Lagrange multiplier* or *adjoint state* of the constraint $F(\mathbf{y}, \mathbf{p}) = \mathbf{0}$.

Because $F(\mathbf{y}(\mathbf{p}), \mathbf{p}) = \mathbf{0}$, it is valid that

$$J(\mathbf{p}) = j(\mathbf{y}(\mathbf{p})) = L(\mathbf{y}(\mathbf{p}), \lambda, \mathbf{p}) \quad (5.10)$$

Instead of calculating the derivative of the cost function, it is easier to calculate the derivative of the Lagrangian. The derivative of the Lagrangian with respect to the parameter \mathbf{p} and a direction \mathbf{q} is

$$\begin{aligned} \mathbf{q}J'(\mathbf{p}) &= \frac{\partial L}{\partial \mathbf{y}}(\mathbf{y}(\mathbf{p}), \lambda, \mathbf{p}) \frac{\partial \mathbf{y}}{\partial \mathbf{p}}(\mathbf{p}) \mathbf{q} \\ &+ \frac{\partial L}{\partial \lambda}(\mathbf{y}(\mathbf{p}), \lambda, \mathbf{p}) \frac{\partial \lambda}{\partial \mathbf{p}}(\mathbf{p}) \mathbf{q} \\ &+ \frac{\partial L}{\partial \mathbf{p}}(\mathbf{y}(\mathbf{p}), \lambda, \mathbf{p}) \mathbf{q} \end{aligned} \quad (5.11)$$

Choosing λ such that the first two summands vanish, means that the Lagrangian is stationary with respect to λ

$$\frac{\partial L}{\partial \lambda} \mu = \mu F(\mathbf{y}, \mathbf{p}) = \mathbf{0} \quad \forall \mu \in \mathcal{V} \quad (5.12)$$

and also with respect to \mathbf{y} :

$$\frac{\partial L}{\partial \mathbf{y}} \mathbf{f} = j'(\mathbf{y}) \mathbf{f} + \lambda \frac{\partial F}{\partial \mathbf{y}} \mathbf{f} = \mathbf{0} \quad \forall \mathbf{f} \in \mathcal{V} \quad (5.13)$$

Eq. 5.13 is called *Adjoint equations*. These both conditions are called *Karush-Kuhn-Tucker* (KKT) conditions (Karush, 1939; Kuhn and Tucker, 1951). If they are fulfilled, the gradient of the objective is equal to the derivative of the Lagrangian with respect to the parameter \mathbf{p} . This means:

$$\mathbf{q}J'(\mathbf{p}) = \frac{\partial L}{\partial \mathbf{p}}(\mathbf{y}(\mathbf{p}), \lambda, \mathbf{p}) \mathbf{q} \quad (5.14)$$

The gradient of the cost function is in this case relatively easy to calculate in practice.

5.1.4 Solving the Minimization Problem

There exist many different types of optimization algorithms, e.g. the Nelder-Mead method or evolutionary algorithms. However, this thesis will focus on *gradient based* methods to solve the following problem:

$$\min_{\mathbf{p} \in \mathcal{P}} J(\mathbf{p}) \quad (5.15)$$

A gradient descent algorithm is an iterative approach starting at some state $\mathbf{p}^{(0)} \in \mathcal{P}$. Then, a sequence of states $\{\mathbf{p}^{(k)}\} \subseteq \mathcal{P}$ is generated in the following way:

Algorithm 5.1 (General gradient descent).

- (1) Choose $\mathbf{p}^{(0)} \in \mathcal{P}$. Set $k := 0$.
- (2) IF $\mathbf{p}^{(k)}$ satisfies some termination criterion: STOP
- (3) Determine direction of descent $\mathbf{d}^{(k)}$ of J in $\mathbf{p}^{(k)}$
- (4) Determine a step size $t_k > 0$ with $J(\mathbf{p}^{(k)} + t_k \mathbf{d}^{(k)}) < J(\mathbf{p}^{(k)})$
- (5) Set $\mathbf{p}^{(k+1)} = \mathbf{p}^{(k)} + t_k \mathbf{d}^{(k)}$, $k=k+1$, go to (2)

Definition 5.4 (Direction of descent). $\mathbf{d} \in \mathbb{R}^n$ is called direction of descent of J in \mathbf{p} if $\exists \hat{t} > 0$ with $J(\mathbf{p} + t\mathbf{d}) < J(\mathbf{p}) \forall t \in (0, \hat{t}]$.

There are different possibilities to choose a direction of descent, but the simplest way is to use the *steepest descent*:

$$\mathbf{d}^{(k)} = \frac{J'(\mathbf{p}^{(k)})}{\|J'(\mathbf{p}^{(k)})\|} \quad (5.16)$$

For many applications it is easier to calculate the gradient of the Lagrangian with respect to the desired parameter instead of calculating the derivative of the cost function directly as explained in Sec. 5.1.3.

Finding a suitable *step size* can also be problematic, which is demonstrated in the following example:

Example (Importance of the step size). Be $J : \mathbb{R} \rightarrow \mathbb{R}$ with $J(p) = p^2$. Choose the initial state $p^{(0)} = 1$, the direction of descent $d^{(k)} = -1$ and the step size $t_k = (\frac{1}{2})^{k+2}$. The solution calculates then as follows

$$p^{(k+1)} = p^{(k)} - t_k = p^{(k-1)} - t_{k-1} - t_k = \dots = p^{(0)} - \sum_{i=0}^k \left(\frac{1}{2}\right)^{i+2}$$

Because the last term is the partial sum of a geometric series, it follows:

$$p^{(k+1)} = 1 - \frac{1 - \left(\frac{1}{2}\right)^{k+3}}{1 - \frac{1}{2}} = \frac{1}{2} + \left(\frac{1}{2}\right)^{k+2} \xrightarrow{k \rightarrow \infty} \frac{1}{2}$$

and thus do not converge to the true minimum $p^* = 0$.

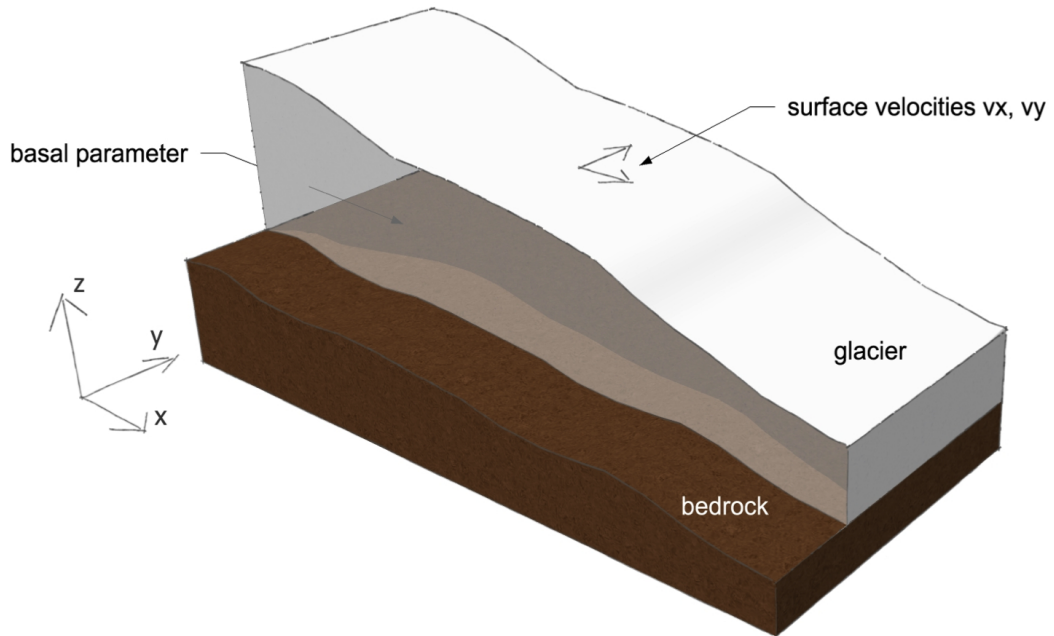


Fig. 5.1: Schematic glacier: velocities on the surface can be measured, while basal conditions are unknown.

Thus, a good choice of the step size is essential, wherefore Morlighem (2011) described the *optimized step size algorithm*. This method computes t_k such that

$$J(\mathbf{p}^{(k+1)}) = \inf_{t_k \in \mathbb{R}_+} J(\mathbf{p}^{(k)} + t_k J'(\mathbf{p}^{(k)})) \quad (5.17)$$

The step size t_k is found by a *Brent search algorithm*, which is terminated, if the cost function falls below a threshold. The Brent method is a combination of bisection, secant method and inverse quadratic interpolation to find the root of a function (Brent, 1971).

5.2 Special Case: Ice Dynamics

In the special case of ice dynamics the forward problem takes the equations of ice dynamics and some parameters, also basal parameters, and computes a three-dimensional ice velocity field containing horizontal surface velocities and the vertical velocity as described in Sect. 4. The bedrock conditions underneath the glacier are not observable, but they strongly influence glacier speed (Figure 5.1). Therefore, an inverse problem has to be solved to estimate the *basal friction* α .

Problem formulation

The conditions underneath the ice at the interface between ice and bedrock are formulated in the sliding law (see Sect. 4.5.1):

$$\tau_b = -k^2 N v_b = -\alpha^2 v_b \quad (5.18)$$

where the basal drag coefficient k or rather the basal friction coefficient α , which also includes the effective pressure, are the parameters of interest. The basal friction coefficient is optimized such that the model output, i.e. the modelled surface velocity, fits the surface velocity observed by satellite remote sensing. We measure this misfit integrated over the upper ice surface Γ_s with the help of a cost function:

$$J(\alpha) = j(\mathbf{v}(\alpha)) = \frac{1}{2} \int_{\Gamma_s} (v_x - v_x^{obs})^2 + (v_y - v_y^{obs})^2 d\Gamma_s \quad (5.19)$$

with $\mathbf{v} = (v_x, v_y)$ the modelled velocity and $\mathbf{v}^{obs} = (v_x^{obs}, v_y^{obs})$ the observed velocity. Following calculations will focus on the Higher-Order approximation (Eq. 4.26). The minimization problem is of the following form:

Theorem 5.1 (Basal friction inverse problem). *Let Ω be the model domain, Γ_u Dirichlet boundary conditions, Γ_σ Neumann boundary conditions, \mathbf{f} a force, and the cost function j as in Eq. 5.19. The PDE-constraint minimization problem is then of the form:*

Minimize the objective function $j(\mathbf{v}(\alpha))$ with the constraint

$$\begin{cases} \frac{\partial}{\partial x} \left(4\mu \frac{\partial v_x}{\partial x} + 2\mu \frac{\partial v_y}{\partial y} \right) + \frac{\partial}{\partial y} \left(\mu \frac{\partial v_x}{\partial y} + \mu \frac{\partial v_y}{\partial x} \right) + \frac{\partial}{\partial z} \left(\mu \frac{\partial v_x}{\partial z} \right) = \rho g \frac{\partial s}{\partial x} & \text{in } \Omega \\ \frac{\partial}{\partial x} \left(\mu \frac{\partial v_x}{\partial y} + \mu \frac{\partial v_y}{\partial y} \right) + \frac{\partial}{\partial y} \left(4\mu \frac{\partial v_y}{\partial y} + 2\mu \frac{\partial v_x}{\partial x} \right) + \frac{\partial}{\partial z} \left(\mu \frac{\partial v_y}{\partial z} \right) = \rho g \frac{\partial s}{\partial y} & \text{in } \Omega \\ v_z(x, y, z) = v_z(x, y, b) - \int_{b(x,y)}^z \frac{\partial v_x}{\partial x} + \frac{\partial v_y}{\partial y} dz' & \text{in } \Omega \\ \mathbf{v}(\alpha) = 0 & \text{on } \Gamma_u \\ \boldsymbol{\sigma} \cdot \mathbf{n} = \mathbf{f} & \text{on } \Gamma_\sigma \end{cases} \quad (5.20)$$

by controlling the parameter α .

Adjoint problem

The Lagrangian of the minimization problem (Theorem 5.1) reads

$$\begin{aligned}
L(\mathbf{v}, p, \lambda_{v_x}, \lambda_{v_y}, \lambda_p, \alpha) = & j(\mathbf{v}) \\
& + \int_{\Omega} \lambda_{v_x} \cdot \left(\frac{\partial}{\partial x} \left(4\mu \frac{\partial v_x}{\partial x} + 2\mu \frac{\partial v_y}{\partial y} \right) + \frac{\partial}{\partial y} \left(\mu \frac{\partial v_x}{\partial y} + \mu \frac{\partial v_y}{\partial x} \right) \right. \\
& + \frac{\partial}{\partial z} \left(\mu \frac{\partial v_x}{\partial z} \right) - \rho g \frac{\partial s}{\partial x} \Big) d\Omega \\
& + \int_{\Omega} \lambda_{v_y} \cdot \left(\frac{\partial}{\partial x} \left(\mu \frac{\partial v_x}{\partial y} + \mu \frac{\partial v_y}{\partial x} \right) + \frac{\partial}{\partial y} \left(4\mu \frac{\partial v_y}{\partial y} + 2\mu \frac{\partial v_x}{\partial x} \right) \right. \\
& + \frac{\partial}{\partial z} \left(\mu \frac{\partial v_y}{\partial z} \right) - \rho g \frac{\partial s}{\partial y} \Big) d\Omega \\
& + \int_{\Omega} \lambda_p \left(v_z(x, y, z) - \left(v_z(x, y, b) - \int_{b(x,y)}^z \frac{\partial v_x}{\partial x} + \frac{\partial v_y}{\partial y} dz' \right) \right) d\Omega
\end{aligned} \tag{5.21}$$

where (v_x, v_y, p) are the state variables (the velocity components as well as the pressure p) and $(\lambda_{v_x}, \lambda_{v_y}, \lambda_p)$ the adjoint states. To derive the adjoint equations, the viscosity is assumed to be linear (only in the adjoint problem), which is widely employed (e.g. MacAyeal, 1993) in order to simplify the calculation. This procedure is called incomplete adjoint method. The adjoint of the HOM is then (more details and a similar proof can be found in Morlighem (2011)):

Theorem 5.2 (Higher-Order adjoint). *For a linear viscosity, the adjoint state $\lambda_v = (\lambda_{v_x}, \lambda_{v_y})$ of the Higher-Order equations is solution of the following problem:*

$$\begin{aligned}
\frac{\partial}{\partial x} \left(4\mu \frac{\partial v_x}{\partial x} + 2\mu \frac{\partial v_y}{\partial y} \right) + \frac{\partial}{\partial y} \left(\mu \frac{\partial v_x}{\partial y} + \mu \frac{\partial v_y}{\partial x} \right) + \frac{\partial}{\partial z} \left(\mu \frac{\partial v_x}{\partial z} \right) &= 0 \text{ in } \Omega \\
\frac{\partial}{\partial x} \left(\mu \frac{\partial v_x}{\partial y} + \mu \frac{\partial v_y}{\partial x} \right) + \frac{\partial}{\partial y} \left(4\mu \frac{\partial v_y}{\partial y} + 2\mu \frac{\partial v_x}{\partial x} \right) + \frac{\partial}{\partial z} \left(\mu \frac{\partial v_y}{\partial z} \right) &= 0 \text{ in } \Omega \\
\lambda_v &= \mathbf{0} \text{ on } \Gamma_u \\
\sigma_{\lambda_v} \cdot \mathbf{n} &= \mathbf{0} \text{ on } \Gamma_{\sigma} \setminus \Gamma_s \\
\sigma_{\lambda_v} \cdot \mathbf{n} &= j'(\mathbf{v}) \text{ on } \Gamma_s
\end{aligned} \tag{5.22}$$

with the cost function derivative

$$j'(\mathbf{v}) = \begin{pmatrix} v_x - v_x^{obs} \\ v_y - v_y^{obs} \\ 0 \end{pmatrix}$$

Cost function gradient

The gradient of the cost function with respect to basal friction can be derived from the partial derivative of the Lagrangian. For simplification it is presented only the Higher-Order cost function gradient limited on cost functions, which do not depend on the basal friction. More details as well as an analogous proof for the Full-Stokes model can be found in Morlighem (2011).

Theorem 5.3 (Higher-Order cost function gradient). *The derivative of the cost function 5.19 with respect to basal friction is:*

$$J'(\alpha) = \begin{cases} 0 & \text{in } \Omega \\ -2\alpha(v_x\lambda_x + v_y\lambda_y) & \text{on } \Gamma_b \end{cases} \quad (5.23)$$

Advanced cost functions

This paragraph describes a more sophisticated cost function including more than only a linear misfit as used in Eq. 5.19. The cost function consists of three terms which are added and weighted by γ_1 , γ_2 and γ_3 :

$$J = \gamma_1 J_1(\mathbf{v}) + \gamma_2 J_2(\mathbf{v}) + \gamma_3 J_3(\alpha) \quad (5.24)$$

The first term is an absolute *linear misfit* between the measured and the modelled velocities on the surface of the glacier:

$$J_1(\mathbf{v}) = \int_{\Gamma_s} \frac{1}{2}(v_x - v_x^{\text{obs}})^2 + \frac{1}{2}(v_y - v_y^{\text{obs}})^2 d\Gamma_s \quad (5.25)$$

While J_1 has the strongest influence on fast flowing parts of the glacier, a *logarithmic misfit* (Eq. 5.26) ensures a good match of observed and modelled velocities in slow flowing areas.

$$J_2(\mathbf{v}) = \int_{\Gamma_s} \left(\log \left(\frac{\sqrt{v_x^2 + v_y^2 + v_{\min}}}{\sqrt{v_x^{\text{obs}2} + v_y^{\text{obs}2} + v_{\min}}} \right) \right)^2 d\Gamma_s \quad (5.26)$$

with a small constant v_{\min} ensuring mathematical consistency. In order to avoid oscillations in the controlled parameter, a *regularization* (Eq. 5.27) is taken into account. It forces the solution to be smooth by penalizing bumps.

$$J_3(k) = \int_{\Gamma_b} \frac{1}{2} \|k\|^2 d\Gamma_b \quad (5.27)$$

The three terms have to be well-balanced because otherwise the solution may be e.g. too smooth (γ_3 too large) or only high velocities are fit by the model (γ_1 too large). In order to find suitable weights, an *L-curve* analysis has to be performed (Hansen, 2001). For this purpose, values of the three objectives are plotted for various γ_i . The resulting curve has an L-shape and its edge gives the optimal weightings. The adjoint problem and the cost function gradient can be calculated in a similar way as before. With this information, a minimization algorithm can find the basal friction matching the observed velocities. An implementation based on this advanced cost function can be found in the ISSM framework.

Optimization algorithms

ISSM includes an implementation of a steepest descent algorithm as described in Sect. 5.1.4. In order to achieve a faster convergence, in general the second derivative of the cost function, the Hessian is necessary. Most optimization algorithms bypass this by approximating the Hessian using so called update formulas. Several algorithms are implemented in toolboxes and ISSM provides interfaces to two of them: Toolkit for Advanced Optimization (TAO) included in PETSc (Balay et al., 2018) and M1QN3 (Gilbert and Lemaréchal, 1989). From the TAO package three algorithms can be chosen, all of them need function and gradient evaluations as input. The Conjugate Gradient method (CG) limits the direction of descent to conjugated directions. This procedure prevents e.g. that the direction of descent is alternating, what can cause slow convergence of the steepest descent method. The Limited-Memory Variable-Metric method (LMVM) approximates the Hessian matrix from previous iterates and gradient evaluations. It uses the Broyden-Fletcher-Golfart-Shanno (BFGS) update formula. A similar method for constrained problems (bounded variables) is the Bounded-constrained Limited-Memory Variable-Metric Method (BLMVM). The M1QN3 package is designed to solve for functions which depend on hundreds of millions of variables. It is also a Quasi-Newton approach approximating the Hessian using the BFGS update formula. Furthermore, it uses a preconditioner, which is dynamically updated, and enforces global convergence by determining the step size using the Fletcher-Lemaréchal algorithm (Gilbert and Lemaréchal, 1989) and realizing the Wolfe conditions.

Reliability of the solution

By applying an inverse method it is important to be aware of the problems that can come with it. The solution is found by fitting the modelled velocity to observations. Errors in observations can thus lead to errors in the solution. Also uncertainties of

the model (e.g. choice of parameters, resolution, approximation or ignoring physical processes) are compensated by the optimized parameter. Therefore, the resulting solution is not necessarily the true basal friction, but it is the parameter that must be applied to the model to fit the observed velocities best. The distribution of basal friction gained by an inversion is only an indication of the real distribution, not an evidence. A sensitivity analysis should be conducted to evaluate the reliability of the estimated parameters and of the model output. A comparison with other studies on the basal conditions in the same region can help to verify the result in the meaning of a physical quantity.

The optimized parameter is assumed to be constant over time. This is only valid for smaller timescales (centuries), wherefore inversions should only be applied for simulations, which do not exceed this time.

5.3 Inverse Methods in Glaciology

Inverse methods were introduced in glaciological applications by MacAyeal (1992) in order to determine the controls on ice stream flow. He applied his method on Ice Stream E, Antarctica, by using a 2D SSA. He states a direct approach using an algebraic solution and a least squares approach. Using variational theory similar to the method described above, the gradient of the cost function is computed and the cost function is minimized using a minimization algorithm. The method was further applied, e.g. by MacAyeal (1993). Vieli and Payne (2003) applied a similar method to Pine Island Glacier. Joughin, MacAyeal, et al. (2004) adapted the algorithm to the Ross ice streams. Goldberg and Sergienko (2011) expanded the method to a hybrid model. A generalization to a 3D model was described by Morlighem, Rignot, Seroussi, et al. (2010) and implemented in ISSM (Larour et al., 2012). Comparisons and improvements of minimization techniques in this field were done e.g. by Habermann et al. (2012) and Petrat et al. (2012). Solving an inverse problem as described above can be called *classical adjoint method*, but there are several other approaches that can be employed.

Another method solving a generalized version of the problem described by MacAyeal (1992) is introduced by Arthern and Gudmundsson (2010) and manages the inversion of the basal drag coefficient and ice viscosity by solving an *inverse Robin problem*. For this purpose, they treat the basal parameter as an unknown parameter in a Robin boundary condition. The problem is then solved using only a solver for the forward problem, which needs to be able to handle Robin boundary conditions. Therefore, they do not need to solve an adjoint problem. A drawback of this method is that it does not integrate observation errors in the cost function. Jay-Allemand et al. (2011) extended the Robin method with a regularization term and implemented it in Elmer/Ice. Gillet-Chaulet et al. (2012) compared results of the classical adjoint

method and the Robin method and found that neither of them is favourable. *Probabilistic approaches* were explored by Chandler et al. (2006), who iteratively computed basal shear stress and basal sliding velocity by minimizing errors in modelled surface velocity and used a Monte Carlo approach to estimate uncertainties. Gudmundsson and Raymond (2008) as well as Raymond and Gudmundsson (2009) utilized a Bayesian inference approach to invert for basal slipperiness and bedrock topography at the same time. For this purpose they used surface topography as input data additionally to the surface velocities. The solution of their approach is the posteriori distribution of the searched parameters as well as an error estimate in the form of a covariance matrix. A Kalman Filter was utilized by Bonan et al. (2014) in order to estimate the bedrock topography, the ice thickness and the basal sliding parameter of a synthetic ice sheet based on SIA. Pollard and DeConto (2012) fitted modelled to observed ice thicknesses by adapting the basal sliding coefficient. For this purpose they run the model forward with a constant climate forcing. The method, which does not use velocity data, was then applied to the AIS. A totally different approach to generate initial conditions including basal properties is a *spin-up procedure*. For this purpose, the model is run forward for a long time (millennia) with climate forcing (Goelzer et al., 2018). A combination of classical adjoint inversion and spin up was done by Rückamp et al. (2018).

A Combined Approach for Filtering Ice Surface Velocity Fields Derived from Remote Sensing Methods

” *It is quality rather than quantity that matters.*

— LUCIUS ANNAEUS SENECA
Philosopher

Context

Methods inverting basal friction (Ch. 5) are all based on one type of data: horizontal surface velocities. These data feed directly into the cost function of the minimization problem, which is mainly the difference between simulated and observed velocities. The friction coefficient is forced to explain the observed surface velocities best. Therefore, a high quality of the observed velocity is assumed to be absolutely essential for inverse modelling. False values in the observed velocities would mean that the basal friction is fit to these errors resulting in false values of the friction coefficient. In the end, this would lead to poor projections, as the friction coefficient is a fundamental parameter controlling ice dynamics and thus an input for modelling the future development of glaciers and ice sheets.

Unfortunately, observation errors occur in all remote sensing based velocity fields due to several reasons like low correlation, poor coherence or atmospheric and ionospheric effects. Removing these errors is necessary to improve the quality of the observed velocities and the inverted basal friction. A main demand on the filtering procedure is the preservation of correct measurements. Removing too many data points would otherwise decrease the quality of the velocity field. A suitable filter algorithm is described in the following paper. It is implemented in python and applied to an artificial velocity field and different real test sites to demonstrate its performance.

The velocity field described in 3.3 will later serve as input for the inversion of the friction coefficient underneath Recovery Glacier, but also this field contains

erroneous values. Thus, the filtering procedure is also applied to the velocity field of Recovery Glacier. The algorithm is able to remove the majority of outliers contained in the velocity field by keeping a reasonable number of data points. The velocity scenes are mosaicked afterwards, so that it can be further processed using a suitable interpolation method. The influence of the quality of surface velocities on the inverted basal friction will be analyzed in a sensitivity study (Sect. 8). Therefore, both filtered and unfiltered velocities will serve as input for the inversion.

Contributions

C.Eis (former Lüttig) has implemented the filter in python programming language, created the artificial flow field and tested the filter on it. N.Neckel has derived velocity fields of Greenland, Petermann Glacier and NEGIS. C.Eis applied the filter on those velocity fields as well as on the velocity field of Recovery Glacier provided by DLR. C.Eis did the statistical analysis and the sensitivity analysis of parameters. All authors discussed the results. C.Eis wrote Sect. 6.2 ("Materials and Methods") and Sect. 6.3.1 ("Artificial Flow Field"), N.Neckel wrote Section 6.6.1 ("Intensity Offset Tracking"), A.Humbert wrote the sections containing the sensitivity analysis (6.3.2, 6.6.2). To all other sections all authors contributed to the writing. Figures related to the sensitivity analysis were created by A.Humbert, all other figures were created by C.Eis. A.Humbert designed the study and supervised it.

Authors and Affiliations

Christine Lüttig ¹ , Niklas Neckel ¹  and Angelika Humbert ^{1,2} 

¹ Alfred-Wegener-Institute, Helmholtz Centre for Polar and Marine Research

² University of Bremen

Abstract

Various glaciological topics require observations of horizontal velocities over vast areas, e.g. detecting acceleration of glaciers as well as for estimating basal parameters of ice sheets using inverse modelling approaches. The quality of the velocity is of high importance, hence methods to remove noisy points in remote sensing derived data are required. We present a three-step filtering process and assess its performance for velocity fields in Greenland and Antarctica. The filtering uses the detection of smooth segments, removal of outliers using the median and constraints

on the variability of the flow direction over short distances. The applied filter preserves the structures in the velocity fields well (e.g. shear margins) and removes noisy data points successfully, while keeping 72-96% of the data. In slow flowing regions, which are particularly challenging, the standard deviation is reduced by up to 96%, an improvement that affects vast areas of the ice sheets.

6.1 Introduction

The dynamics and mass balance of glaciers governs the contribution of ice sheets to sea level change. Consequently, monitoring changes in the dynamics in high spatial resolution and with a large spatial coverage, like entire ice sheets, is crucial. Also, the temporal evolution of the flow dynamics is very important. This can only be achieved using satellite remote sensing data. The key physical quantity here is the three dimensional velocity field of the glacier $\vec{v}(x, y, z, t)$, of which, however, only the horizontal velocity at the surface of the ice sheet is accessible. Numerous studies (e.g. Joughin, B. Smith, Howat, Scambos, and Moon, 2010) use different sensors and algorithms to retrieve velocity fields, but common to all are measurement errors that lead to noisy velocity fields. False velocity data needs to be filtered out in order to avoid complications in all the following fields of applications.

Timing and spatial onset of changes in velocities, caused by seasonal or long-term climate forcing, is of particular interest to glaciologists. With more accurate velocity fields our ability to detect acceleration is improved. The most prominent example is the acceleration and increased seasonality of Jakobshavn Isbræ in western Greenland. This might be connected to changes in the shear margins of the ice stream, highlighting the need of accurate velocity retrievals in these areas. Here, the gradients of the velocity field components are required with high accuracy, so that shear deformation rates can be retrieved in order to assess if changes in the shear margins are indeed the cause of acceleration.

Numerical models of ice sheets and glaciers use horizontal surface velocities to assess the model quality and partly to adjust model parameters. Simulations projecting the future contribution of ice sheets to sea level change are suffering from a poorly constraint initial state, which is today's velocity field. In order to overcome this, glaciologists use inverse modelling of ice sheets and ice streams, in which basal parameters are adjusted so that modelled horizontal surface velocities match the observed field. As the momentum balance equation, which is solved in inverse modelling, contains gradients of the velocity components (strain rates), the influence of non-smooth velocity data is enhanced. In this case, errors in the input field lead to errors in computed basal parameters and this in turn leads to incorrect projections. With missions such as Radarsat-1, Radarsat-2, TerraSAR-X, TanDEM-X, Sentinel-1A/B, Sentinel-2 and Landsat-8 a new era of mapping large-scale surface velocities

has begun (Joughin, B. Smith, Howat, Scambos, and Moon, 2010; Fahnestock et al., 2015; Nagler et al., 2015; Kääb et al., 2016; Mouginot, Rignot, et al., 2017). Today surface velocities of ice sheets, glaciers and ice caps are produced in near real-time and several data portals exist where the user can download velocity products. However, as most of these velocity estimates are based on offset tracking procedures, outliers and data gaps are most common and appropriate filtering is absolutely essential before further analysis.

Many of the applications of velocity fields will use an interpolation to obtain continuous velocity data sets which might be used for inverse modelling of glaciers subsequently. Depending on the type of interpolation applied, outliers might have strong effects, as interpolation techniques that rely on higher order polynomials are generally very oscillatory and may produce high amplitude outliers between the interpolation points.

The nature of erroneous data points is two fold. On the one hand, a pixel may have a false value in one or both velocity components. On the other hand, such a false velocity estimate can lead to a false flow direction. Outliers can occur in many different ways, such as covering only one pixel or a cluster of connected pixels. These clusters can be either smooth within themselves, or also very noisy. Other features are appearing over larger areas, like single lines or regular patterns. False velocity retrieval is caused by different factors: (i) low correlation, caused by changes in the surface properties between data acquisitions (e.g. surface melt or precipitation), (ii) very fast flow is causing poor coherence or (iii) atmospheric and ionospheric effects. Errors induced by atmospheric variations between the dates of data acquisitions can mostly be neglected for velocity retrievals from intensity offset tracking, but can be an issue for velocity estimates from synthetic aperture radar interferometry (Yan et al., 2015). Ionospheric effects can result in azimuth streaks in the derived velocity fields (Gray, Mattar, and Sofko, 2000; Wegmüller et al., 2006).

Critical zones can be especially slow or fast flowing regions, shear margins or pinning points of ice shelves. Future and current satellite missions in L-band, like ALOS PALSAR-2, NISAR and Tandem-L are preferable for ice velocity retrieval as deeper penetration is beneficial in areas with loss of coherence due to changes in surface properties or very fast flow. However, L-band signals suffer from ionospheric effects leading to errors in velocity retrieval (Gray, Mattar, and Sofko, 2000; Wegmüller et al., 2006). Again, a filter procedure might be able to reduce ionospheric effects in the velocity fields.

This reveals the importance of an appropriate filtering procedure. To avoid manual filtering of outliers, because this would be very time consuming and leads to different solutions for different users, it is possible to use a wide range of algorithms developed for this purpose. A filter needs to fulfill the following criteria: (i) remove erroneous data reliably, (ii) the structure of the velocity field remains unchanged, e.g. shear margins or sticky spots are not smoothed out, (iii) concurrently, as many data points as possible are saved and (iv) reasonable computational costs. Here, we

present a filter approach consisting of three different filter steps. This filter will be in future implemented into the Tandem-L product generation.

6.2 Materials and Methods

6.2.1 Description of the Filter

Starting with the projected x- and y-components of the velocity field we applied a filter combining three approaches. The first one divides the field into parts recursively, which are smooth within themselves, and was introduced by Rosenau et al. (2015). In the second step, the remaining outliers are removed by a filter using the median of the field. The third filter is based on variations of directions of the vector field. In the first component of the filter, all data points in the field are allocated to different segments. Afterwards, segments with less than n_{min} data points are deleted. The division in segments of the data points is done recursively, starting with a random seed point p . For each direct neighbour n , the difference between the velocity of p and n in both components (x and y) has to be compared with the threshold t . Only if it is less than t in both velocity components, the neighbor n is allocated to the same segment as p and the procedure starts again with this new point. There are two terms influencing the threshold t : These are a constant error e_{const} and the difference between the same points in an a-priori velocity field Δv multiplied with a factor w (in our case 1.5).

$$t = e_{const} + |w \cdot \Delta v| \quad (6.1)$$

$$e_{const} = a \cdot \sqrt{\sigma_M^2 + \sigma_R^2} \quad (6.2)$$

The constant error includes the errors of offset tracking σ_M and coregistration σ_R and is multiplied by a factor $a \in [0, 1]$ in order to reduce the accepted error, often leading to better results with more points sorted out. In the applications below, we set $a = 0.2$. We computed these errors like in Seehaus et al. (2015), where σ_R is calculated from stable points on rock surfaces. For this purpose we figured out coordinates of rocks in the area of the velocity field and computed the magnitudes of the velocities in these locations. If there are no stable points in the considered region, this error has to be estimated with the help of a velocity field with similar characteristics. The error of coregistration is calculated as the median of the magnitudes. The offset tracking error is computed as in (6.3) and strongly depends on the sensor resolution.

$$\sigma_M = \frac{C \Delta x}{z \Delta t} \quad (6.3)$$

with C , uncertainty in image registration and tracking in pixels [px], Δx image resolution [m/px], z oversampling factor and Δt time interval between the images [d]. We assumed $C = 0.4 px$ and $z = 2$, as it is suggested in Seehaus et al. (2015).

The second filter step is performed in a window moving one pixel per step. For every data point p , the medians \tilde{v}_x, \tilde{v}_y and the standard deviations s_x, s_y of the window in both components are computed. The point is only kept, if the difference between the velocity and the median is smaller than ϵ_m times the standard deviation in both components as described in (6.4) and (6.5).

$$|v_x(p) - \tilde{v}_x| < s_x \cdot \epsilon_m \quad (6.4)$$

$$|v_y(p) - \tilde{v}_y| < s_y \cdot \epsilon_m \quad (6.5)$$

with $v_x(p)$ velocity of data point p in x-direction and $v_y(p)$ velocity of p in y-direction as well as \tilde{v}_x median of all velocities of the window in x-direction and \tilde{v}_y median of all velocities of the window in y-direction. The parameter ϵ_m can be freely chosen, however, $\epsilon_m = 3$ was optimal in our applications. The window size in this filter was set to 25 pixels.

The displacement in x- and y-direction defines the direction of flow, θ_p , of each data point. The third approach works with this information, again by using a moving window, which is in our application of the same size as before (25 pixels), but can be chosen independently from the second filter step. With each step, the window is shifted by one pixel. First we check if the direction of a data point p is close to the mean direction $\bar{\theta}$ of the window (6.6)

$$|\theta_p - \bar{\theta}| < s \cdot \epsilon_d \quad (6.6)$$

with s standard deviation of all directions in the window and ϵ_d unrestricted parameter proposed to be $\epsilon_d = 3$. Subsequently, the number of direct neighbors n of the point p with $\theta_p \in \mathbb{R}$ having a difference of more than α degrees to θ_p is counted.

$$|\theta_p - \theta_n| < \alpha \quad (6.7)$$

For the angle α a value of $\alpha = 10^\circ$ is proposed. If this number of neighbors is higher than 4, the point is discarded.

In the last step, all points having less than 2 neighbors n with $\theta_n \in \mathbb{R}$, are removed because in this case a comparison with neighboring points is not possible. In all three steps, a point which is detected as an outlier in only one component is removed in the other component of the velocity vector. More details to the filter processes can be found in the flowchart in Figure 6.13. The effect of the choice of the parameters on the performance of the filter is discussed below in more detail.

6.3 Results

6.3.1 Artificial Flow Field

In order to test the performance of the filter, we created an artificial velocity field across which we have distributed outliers randomly. The field has a size of 200×245 data points. The a-priori field has increasing velocity values between 1 and 200 m a^{-1} in x-direction, while the v_y component increases in y-direction from 1 to 245 m a^{-1} , which leads to different flow directions. We distributed outliers by adding normal distributed values ($\sim \mathcal{N}(0, 122.5)$) to 4900 random points of the field. Additionally, we added 5000 values distributed with $\sim \mathcal{N}(0, 50)$ in a smaller region to simulate strong outliers in a limited area. In the end, in a region with a size of 10×10 pixels the velocity values are generated randomly ($\sim \mathcal{N}(0, 100)$) (Figure 6.1a). The applied filtering procedure can remove nearly all of these outliers (Figure 6.1b). Only 0.33% of the generated outliers are left. These outliers have a relatively small difference (maximal 6.07 m a^{-1}) to the expected values given by the a-priori field. Valid points falsely removed by the filter had less than 2 neighboring points for comparison in the last filter step.

6.3.2 Filter Parameter Sensitivity Tests

The three filter steps obey a number of parameters. Here we test the influence of these parameters on the ability to filter outliers. As glacier and ice sheet velocity fields contain certain characteristics with distinct challenges for the filter, we selected a subset of a velocity field covering a stripe-shaped area over a fast flowing glacier, including its shear margins and extending into slow flowing areas (the location of

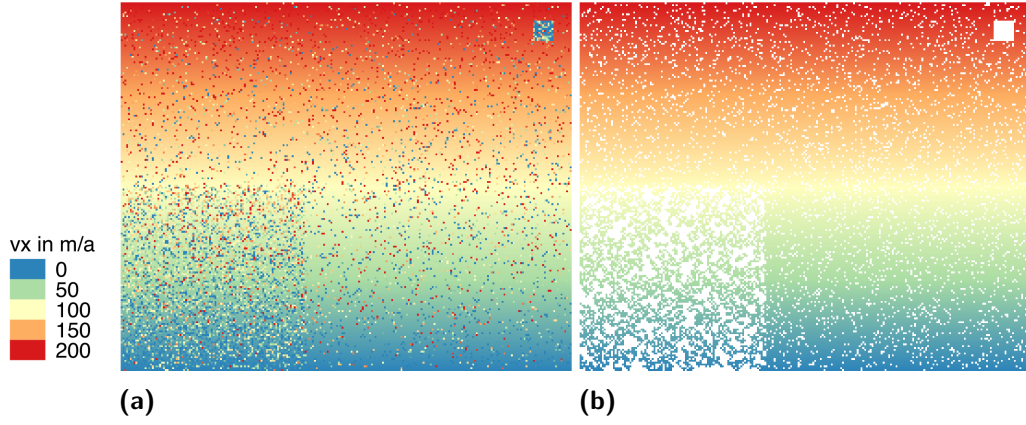


Fig. 6.1: Performance test of the filter using an artificial velocity field: (a) Before filtering and (b) after filtering.

the profile is shown in Figure 6.3d). This subset contains 80 676 pixels of the velocity field, which we consider to be sufficiently large for these tests. For filter step one (smooth segments), we have varied a from 0.1 to 1 in steps of 0.1, n_{min} from 2 to 12 with increments of 2 and the difference to the a-priori velocity field Δv from 1 to 2 in increments of 0.1. For filter step two (median) we tested the effect of the window size ($window_{median}$) and ϵ_m . $window_{median}$ was varied from 5 to 45 in steps of 5 and ϵ_m was increased from 1.0 to 5.0 in increments of 0.5. The third filter step (directions) is influenced by the choice of the window size too, ($window_{dir}$, varied from 5 to 45 in steps of 5), ϵ_d (from 1.0 to 5.0 in increments of 0.5) and the angle α (from 2.5° to 30° with step size 2.5°). Figure 6.2 shows an example of parameter α while the remaining parameters can be found in Figures 6.14 to 6.18 in the Appendix.

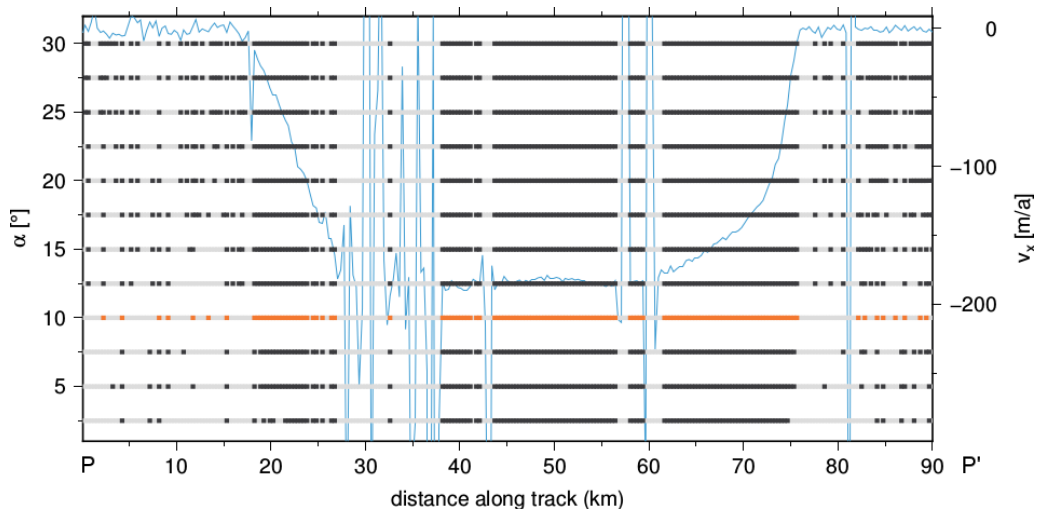


Fig. 6.2: Sensitivity of the third filter (directional) to α . Data points that passed the filter are plotted as black points, while those that were removed are shown in gray color. The selected value of α (left vertical axis) is highlighted in orange. The blue line displays v_x along the profile shown in Figure 6.3d.

Filter one is highly insensitive to n_{min} , the range from $n_{min} = 4 - 12$ give similar results, only $n_{min} = 2$ shows a difference. Thus the choice of $n_{min} = 8$ is reasonable and does not affect the performance of the filter negatively. The effect of a is, however, larger but declines for $a \geq 0.4$. With increasing w , the number of points remaining is increasing, which is to be expected, as a higher w is increasing the threshold t . Similar to that, $w = 0.1$ is reducing the remaining data points significantly in both, fast and slow flowing regions. The optimal parameter set is thus $n_{min} = 8$, $a = 0.2$ and $w = 1.5$.

The second filter is not particular sensitive to the window size. In the range of 20 to 35 pixel no variation occurs at all and below and above this range, only slight changes in faster flowing areas appear. $window_{median}$ was thus chosen to be 25 pixels. This filter is more sensitive to the choice of ϵ_m . Low values of $\epsilon_m \leq 2$ remove a large number of data points, while $\epsilon_m \geq 3.0$ does lead to similar results. An outlier at a distance along track of 57 km exemplifies that our choice of $\epsilon_m = 3.0$ is suited well to remove this outlier.

The directional filter shows a similar response to the window size, meaning that it is not particular sensitive on the size. The effect of ϵ_d is also similar to the second filter, as small values for ϵ_d remove an unreasonable high number of data points and the range $\epsilon_d \geq 3.0$ does lead to similar results. The effect of α is strongest in slow flowing areas, in which we also expect the largest number of false directions. From $\alpha \geq 20$ the number of remaining data points increases in a way that the filter becomes meaningless. At the other end of the spectrum of values for α , the number of remaining data points becomes critical for $\alpha < 10$. Hence our choice is $\alpha = 10.0$, the window size is set to 25 pixels and $\epsilon_d = 3.0$. These values may serve for other applications of the filter as a first guess, however, we recommend users perform similar tests for their particular areas and sensors for optimising the performance.

6.3.3 Recovery Glacier

We applied the filter to a velocity field of the Recovery Glacier (Antarctica, Figure 6.3a). The data are derived by intensity offset tracking of stripmap pairs of TerraSAR-X in 2012/13 and were provided by DLR in Floricioiu et al. (2014) and Abdel Jaber (2016). The revisit time was eleven to 33 days and the resolution of the velocity field is 156 meters. Every individual velocity field retrieved from one pair of satellite scenes was filtered separately to preserve as much data points as possible. Thus, overlapping scenes can compensate for removed outliers. As an a-priori velocity field for the smooth segments filter we used the Making Earth System Data Records for Use in Research Environments (MEaSUREs) ice velocity map of Antarctica (Rignot et al., 2011b; Rignot et al., 2011c). Afterwards the field was mosaicked by gmt grdblend (Wessel et al., 2013) using the mean of overlapping pixels. We have done this also for the fields after the first two filter steps to illustrate the results. Figure

6.3 shows the original v_x field and the results after each filter step. This figure demonstrates that the first filter (upper right panel) removes most outliers that are visually detectable on this scale. The next two steps (panels below) remove still a markable number of outliers, however keeping a reasonable amount of data. As the scale of the figure does not allow any detailed discussion of the effects, we selected four different sites for an in-depth discussion, with very distinct characteristics: one fast and one slow moving region, a shear margin and a region with a very high number of outliers (named line of outliers in the continuation). These regions are annotated in Figure 6.3a.

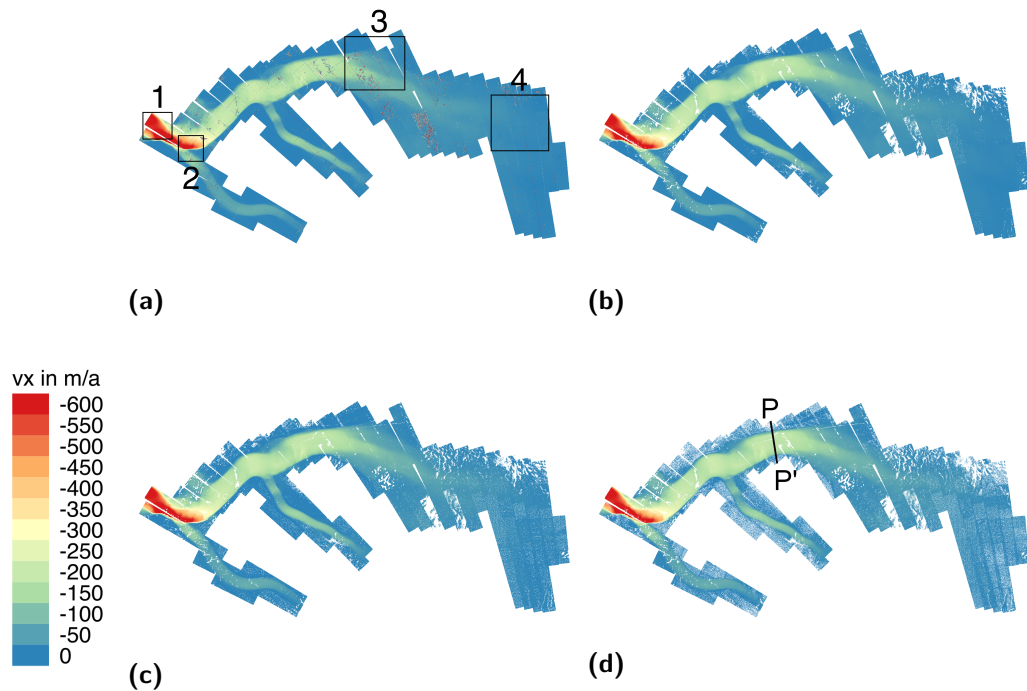


Fig. 6.3: Velocities in x-direction of the Recovery Glacier, Antarctica: (a) Original data. (b) After the first filter step (smooth segments). (c) After the second filter step (median). (d) After the third filter step (directions). The upper left panel shows the locations of the tested regions: 1 - fast flowing region, 2 - shear margin, 3 - region with line of outliers and 4 - slow flowing region.

In order to give some quantitative information on the statistics of the effect of the combined filter, we present boxplots for all four regions in Figure 6.4 for both components, v_x and v_y . The left panels show the original data, whereas the right panels present the statistics after the application of all three filter steps. Please note that the vertical axis changes between the left and right panels. In all cases the number of outliers is significantly reduced and the range of values is diminished. The range of the quartiles in v_x and v_y becomes smaller. The efficiency of the filter to remove outliers is also evident from Table 6.1. For three of the four subregions, as well as for the whole mosaic, the standard deviation decreased significantly during

the filtering while the mean stays rather constant. For example: while the mean v_x from the line of outliers changed by 3.4%, the standard deviation was reduced by 76.6% during the filtering (Table 6.1). This difference is less striking in regions with more heterogeneous flow velocities, for example in the shear margin. In this example the mean v_x changed by 9.1% while the standard deviation was reduced by 27.3%. In order to investigate the effect of the three filter steps in-depth, we discuss below the v_x field for the four regions after each filter step.

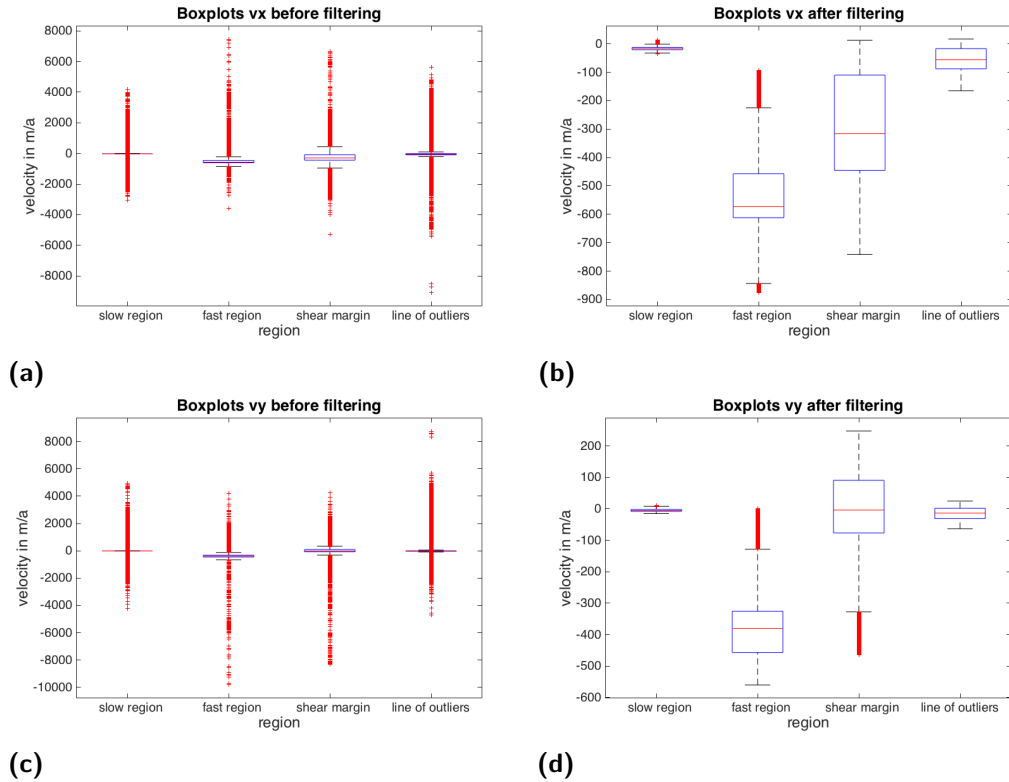


Fig. 6.4: Boxplots of the four test regions at Recovery Glacier. v_x before (a) and after (b) filtering. v_y before (c) and after filtering (d).

Shear margin

This subset (Figure 6.5) is a shear margin with a transition from the main trunk of the glacier to nearly stagnant motion and the inflow from a side branch into the main trunk. The first filter step (smooth segments) removes clusters of outliers (marked 1 and 3 in Figure 6.5a) successfully and also eliminates the outliers along the margins of the satellite scenes (denoted with 2). The second filter (median) removes more data points with low v_x , which is also the range (marked with 4 in Figure 6.5d) with the strongest effect of the third filter (directions). In comparison of Figure 6.5a to 6.5d, the most obvious outliers are captured, however, a stripe-like pattern (denoted with 4 in Figure 6.5d) is still present after all filter steps. The comparison between the initial and final field of v_x also reveals that the number of data points in the

shear margin itself is strongly reduced and patches without data appear, however, there are enough remaining data points to assure that a subsequent interpolation would be able to represent the shear margin well.

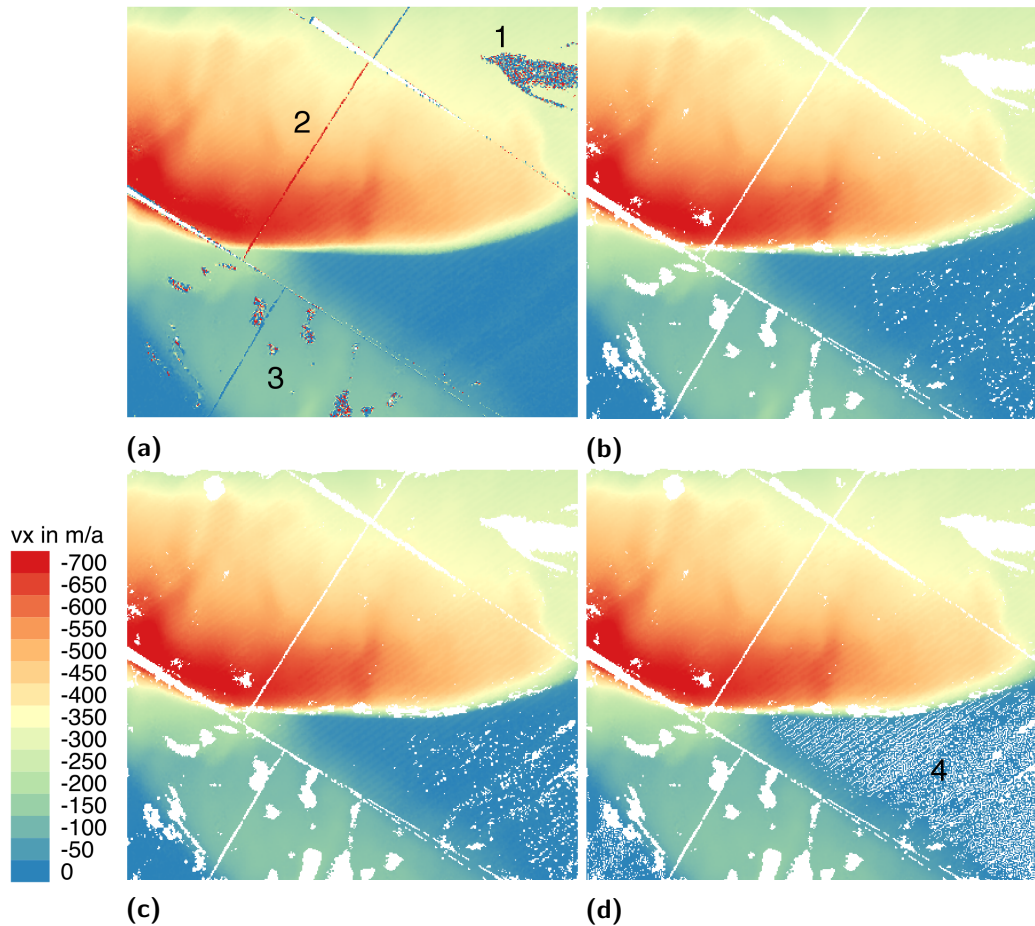


Fig. 6.5: Velocities in x-direction in a shear margin of the Recovery Glacier, Antarctica: (a) Original data. (b) After the first filter step (smooth segments). (c) After the second filter step (median). (d) After the third filter step (directions)

Fast flowing region

We also chose a very fast flowing region, typical for the central part of ice streams (Figure 6.6) with displacements up to 800 m a^{-1} to test the filter. After the first step, the outliers at margins of the satellite scenes are removed. The cluster of outliers around 2 in Figure 6.6a are also well detected. In the zone labeled with 1 large variations in v_x are removed successfully. Here, the glacier surface is heavily crevassed, which might be the cause for false velocity detection. The median and directional filters do not remove a significant number of data points in this case. This was to be expected, as wrong flow directions are typically a problem in slow moving areas.

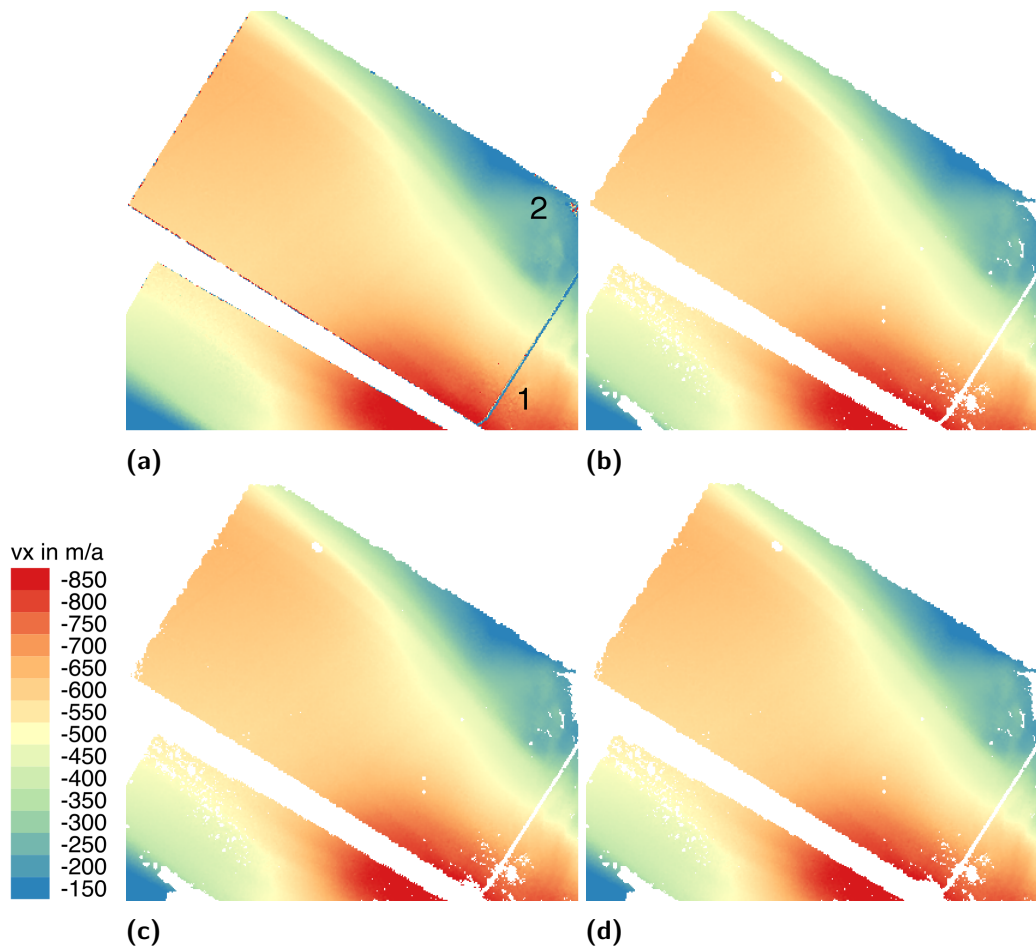


Fig. 6.6: Velocities in x-direction in a fast flowing region of the Recovery Glacier, Antarctica: (a) Original data. (b) After the first filter step (smooth segments). (c) After the second filter step (median). (d) After the third filter step (directions)

Slow flowing region

The subset in Figure 6.7 is characterised by low velocities, which are typically prone to problems in both, magnitude as well as direction of flow. Consequently, a lot of erroneous data points are exhibited in Figure 6.7a. The first filter removes the clusters, like those marked with 1, successfully, but leaves much more outliers than in the case of the fast flowing region and the shear margin. The second filter is most effective with outliers like the ones marked with 2 and 3. In this example the effect of the directional filter becomes more apparent: the area around 4 has been stripped off a large number of data points. However, there are still invalid data points remaining in this region. As the difference between the data points in this area is small, a subsequent interpolation is not expected to be affected substantially.

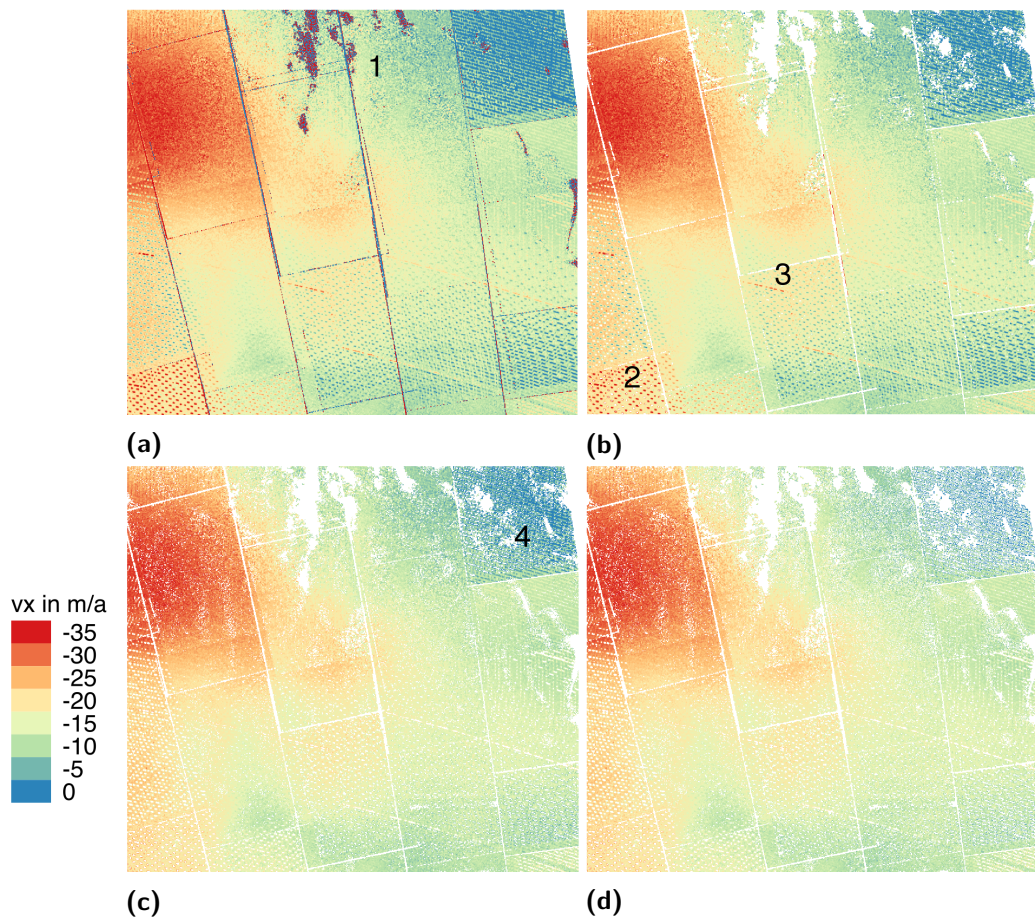


Fig. 6.7: Velocities in x-direction in a slow flowing region of the Recovery Glacier, Antarctica: (a) Original data. (b) After the first filter step (smooth segments). (c) After the second filter step (median). (d) After the third filter step (directions)

Line of outliers

A large number of outliers is evident in the region shown in Figure 6.8. Beside the clusters of outliers (marked with 1) that also appeared in the other examples, there is a notable feature: a line running through the velocity field of the entire glacier. The first filter step detects these clusters well, as in the examples above. However, the feature 2 is not detected. After the second filter, the line is almost completely erased, whereas the outliers in the region marked with 3 remain. The last filter step has the strongest effect in the area around 3 and the adjacent region of low velocities. This is in agreement with the above examples where the directional filter is most effective in slow moving areas.

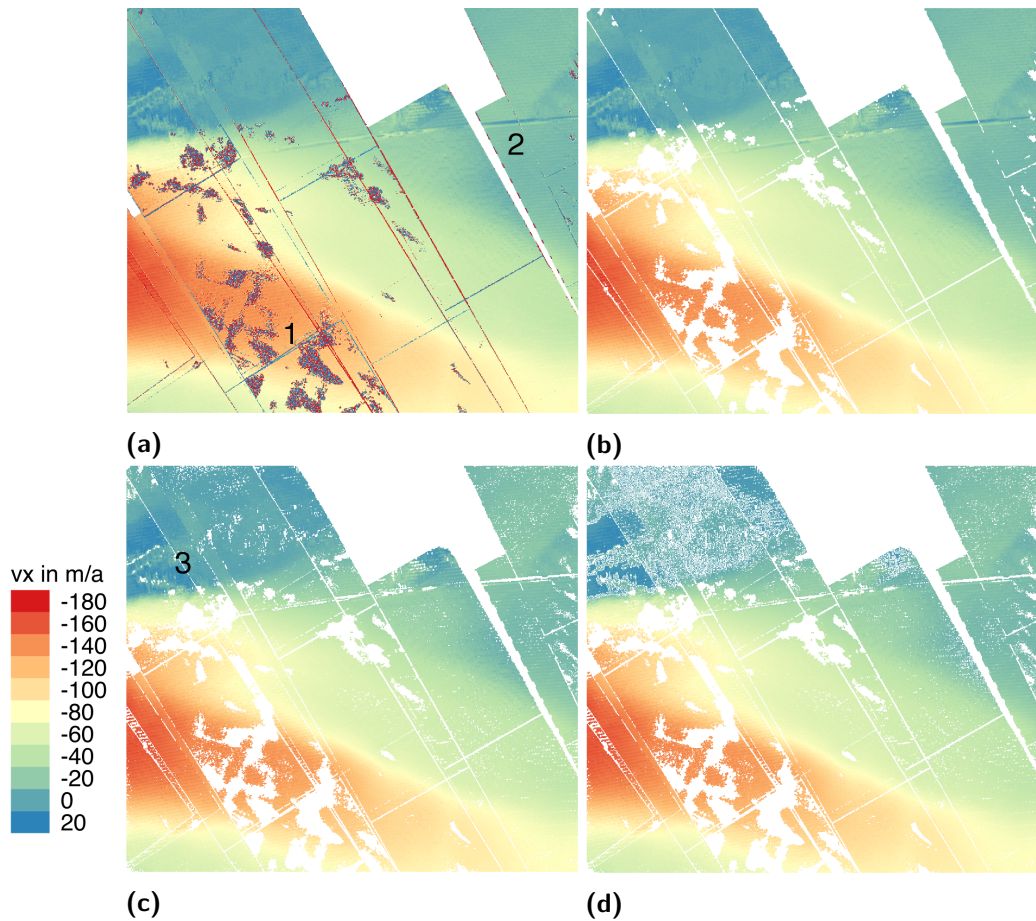


Fig. 6.8: Velocities in x-direction in a region with a line of outliers of the Recovery Glacier, Antarctica: (a) Original data. (b) After the first filter step (smooth segments). (c) After the second filter step (median). (d) After the third filter step (directions)

6.3.4 Other Locations

Next to the Recovery Glacier in Antarctica, we tested the filter in some more regions in Greenland. Here we chose a Sentinel-1 velocity mosaic of the Greenland Ice Sheet, a TerraSAR-X derived velocity field of Petermann Glacier and a part of a Sentinel-1A velocity field of a subset of the North East Greenland Ice Stream (NEGIS). These regions are annotated in Figure 6.9a.

Figure 6.10 shows boxplots for the three regions, indicating v_x in the upper panels and v_y in the lower ones. The left panels show the original data, while the right panels represent the data after the three step filtering approach. From the boxplots it becomes evident that the number of outliers could be significantly reduced for the NEGIS subset. This applies for both components v_x and v_y . However, a minor reduction of the standard deviation as evident from Table 6.1 implies that only few large outliers were present and fast and low velocities coexist in this example. The Sentinel-1 velocity mosaic of Greenland covers a wide range of velocities in both directions wherefore the effect of successfully removed outliers becomes hidden in

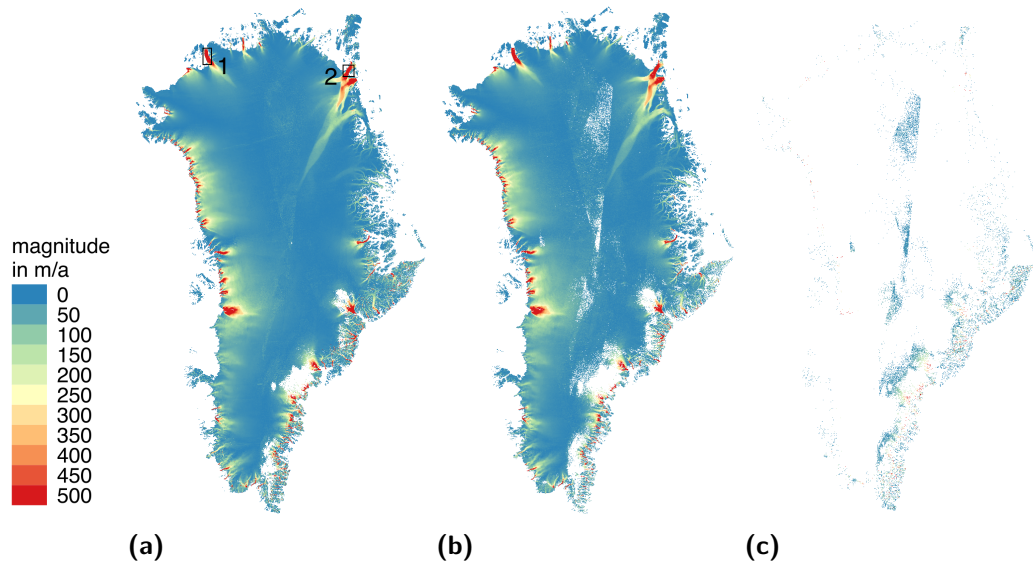


Fig. 6.9: Surface velocities of the Greenland Ice Sheet (magnitude): (a) Original data (b) Filtered data. (c) Removed data. The left panel indicates the locations of the tested regions: 1 - Petermann Glacier, 2 - subset of the North East Greenland Ice Stream (NEGIS).

the boxplots shown in Figure 6.10. The latter also applies for the minor reduction of the standard deviation in this example as shown in Table 6.1. The small reduction of 0.4% of the standard deviation of v_y for Petermann Glacier can be attributed to the fact that only few outliers were present in this example (Table 6.1). In the following, the effects of the presented filtering strategy on the three test regions in Greenland are shown in more detail.

Sentinel-1 Greenland velocity mosaic

The velocity mosaic of the Greenland Ice Sheet was obtained by intensity offset tracking on 6-day repeat-pass Sentinel-1A/B acquisitions. For this we employed all available Level-1 Single Look Complex (SLC) products acquired in IW TOPS mode between 01 December 2016 and 01 March 2017 resulting in a total amount of 1779 image pairs. Prior to the coregistration of image pairs, successive bursts of each acquisition were mosaicked. Then intensity offset tracking was performed as described in Section 6.6.1. After testing several window sizes we choose a final search window size of 1000 m in both range and azimuth directions. Offsets with a normalized cross correlation below 0.1 were considered erroneous and excluded from the analysis. The single velocity fields were gridded to 250 m and masked by a manually adjusted version of the Bedmachine ice mask (Morlighem et al., 2014; Morlighem et al., 2015). This excluded large areas of open water and hence reduces the computation time of the filtering steps significantly. After filtering of the single velocity fields mosaicking was performed as described in Section 6.3.3.

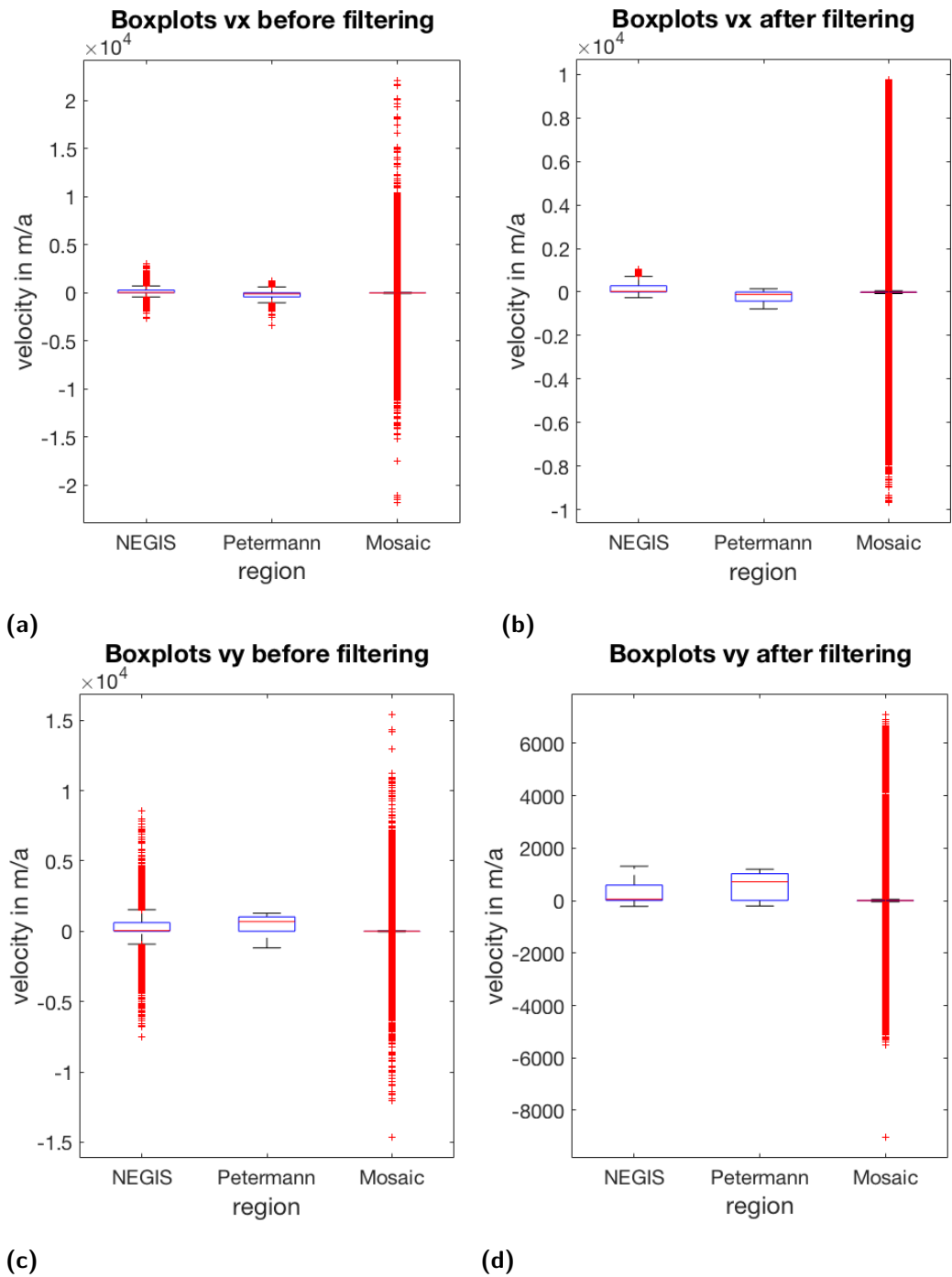


Fig. 6.10: Boxplots of the three regions in Greenland. (a) In x-direction before filtering. (b) In x-direction after filtering. (c) In y-direction before filtering. (d) In y-direction after filtering.

It is very important that the a-priori velocity field used in the first filtering step (smooth segments) has a good spatial coverage. We therefore make use of the MEaSUREs Multi-year Greenland Ice Sheet Velocity Mosaic which shows no data gaps but includes data acquired between 01 December 1995 and 31 October 2015 (Joughin, B. Smith, Howat, and Scambos, 2016).

While Figure 6.9a shows the Sentinel-1 velocity mosaic of Greenland prior to the

region	component	mean before [$m a^{-1}$]	mean after [$m a^{-1}$]	standard deviation before [$m a^{-1}$]	standard deviation after [$m a^{-1}$]
Recovery Glacier (RG)	v_x	-49.83	-60.65	222.00	99.49
	v_y	-5.82	-7.40	203.77	69.09
RG slow flowing region	v_x	-13.44	-16.84	111.34	6.62
	v_y	-3.47	-4.63	104.99	4.42
RG fast flowing region	v_x	-518.72	-530.76	243.28	144.13
	v_y	-373.49	-374.38	242.39	110.98
RG line of outliers	v_x	-59.60	-57.59	183.84	43.04
	v_y	-8.01	-15.02	169.18	20.10
RG shear margin	v_x	-269.21	-296.07	278.77	202.53
	v_y	-3.93	0.89	243.12	112.50
Greenland mosaic	v_x	-10.32	-11.92	134.11	124.85
	v_y	2.53	3.41	100.06	90.86
Petermann Glacier	v_x	-200.95	-206.43	224.59	225.19
	v_y	568.97	586.79	474.42	472.45
NEGIS subset	v_x	176.43	179.93	246.22	243.5
	v_y	294.83	296.06	413.03	400.63

Tab. 6.1: Statistical properties of the velocity in x- and y-direction before and after application of all three filter steps in the tested regions.

filtering, Figure 6.9b shows the data after applying the three step filtering approach. The excluded velocity measurements are shown in Figure 6.9c. It becomes evident that most removed data points are located in the central part of the ice sheet and in its south-eastern part. On the one hand the acquisition of Sentinel-1A/B data is concentrated on the margins of the Greenland Ice Sheet as these are the dynamical key regions. Therefore, less velocity fields could be derived in the interior of the ice sheet, leading to a decreased ability to fill gaps from multiple data takes. On the other hand low velocities of $< 20 m a^{-1}$ are prevailing in this region. Similar to the slow flowing region of Recovery Glacier, this region is strongly affected by the median and the directional filter. It is also evident from Figure 6.9 that many data points were removed in the south-eastern part of the ice sheet. This region is known to have poor coherence due to frequent snowfall wherefore velocity retrieval is difficult in this area (Joughin, B. Smith, Howat, Scambos, and Moon, 2010; Nagler et al., 2015). This large-scale example shows that the applied filtering strategy is capable to discover regions in which the offset intensity tracking poses challenges. Thus it is also conceivable to think of the filter as a tool to investigate systematically the locations in which velocity retrieval is difficult. Individual fast flowing outlet glaciers, where the offset tracking often relies on surface features remain well preserved during the filtering procedure.

Petermann Glacier

For Petermann Glacier we show a 2014 winter velocity field generated by intensity offset tracking on a 11-day repeat-pass TerraSAR-X/TanDEM-X acquisition following the approach described in Section 6.6.1. After testing several window sizes we choose a search window size of 250 m in both range and azimuth directions, which is close to window sizes employed in earlier studies (e.g. Rankl et al., 2014; Seehaus et al., 2015). Offsets with a normalized cross correlation below 0.1 were considered erroneous and excluded from the analysis. The final velocity field was gridded to 50 m.

Figure 6.11 shows the v_y field of Petermann Glacier, which represents the main flow component. Obvious outliers are marked as 1 in Figure 6.11a and are removed during the first filtering step (smooth segments, Figure 6.11b). Also several data points of the side margins of two tributary glaciers are removed by the smooth segment filter (marked as 2 in Figure 6.11b). The median filter leads to more data gaps in both of the mentioned tributary glaciers. The directional filter removes several data points on stable ground (marked as 3 in Figure 6.11d). As the v_y field of Petermann Glacier is almost in the azimuth direction of the satellite scene, some minor ionospheric effects remain visible.

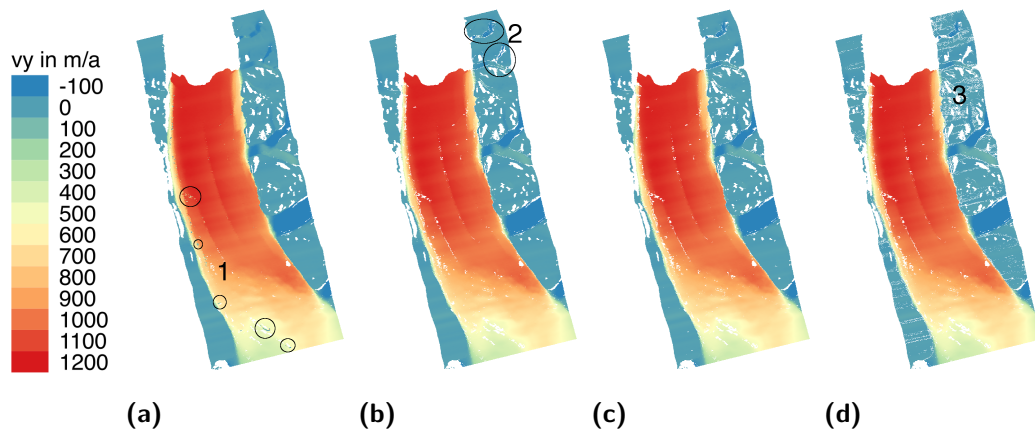


Fig. 6.11: v_y of Petermann Glacier, Greenland: (a) Original data. (b) After the first filter step (smooth segments). (c) After the second filter step (median). (d) After the third filter step (directions). Circles and numbers indicate locations which are discussed in the main text.

NEGIS subset

Compared to the smooth TerraSAR-X velocity field of Petermann Glacier we selected a rather noisy velocity field of a subset of NEGIS to further test the presented three step filtering strategy. The velocity field is based on two Sentinel-1A scenes acquired on 02 March 2016 and 14 March 2016. The data were processed as described in Section 6.3.4.

The velocities in y-direction are presented in Figure 6.12. The original velocity field is shown in Figure 6.12a, the results of the first filtering step (smooth segments) are presented in Figure 6.12b, while Figure 6.12c and 6.12d show the data after applying the second (median) and third (directions) filtering step respectively. Contrary to the fast flowing region of Recovery Glacier, outliers are also evident in fast flowing regions of $>600 \text{ m a}^{-1}$ (marked as 1 in Figure 6.12a). Most of these outliers are successfully removed after the first filtering step (smooth segments, Figure 6.12b). However, some outliers, e.g. in the shear margin (marked as 2 in Figure 6.12b) are still present. These specific outliers are removed by the second filtering step (median, Figure 6.12c). Also several data points on stable ground are deleted by the median filter (marked as 3 in Figure 6.12c), an effect which is further amplified by the third (directions) filtering step. In this example the filter is able to remove many erroneous data points (i.e. only 71.58% of the original data points are remaining, Table 6.2). However, depending on the further analysis an additional smoothing and interpolation step might be necessary for this example.

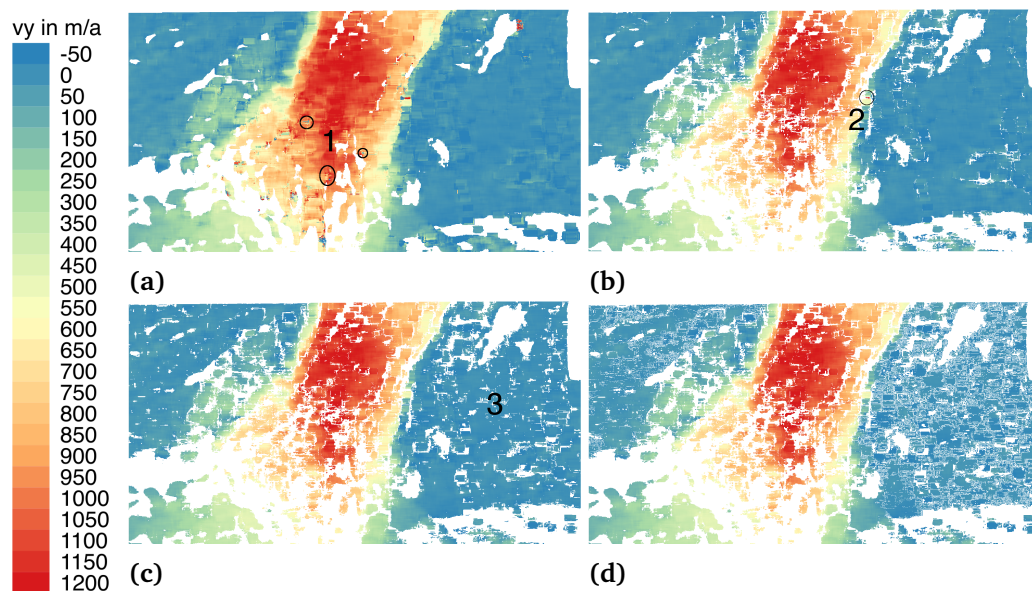


Fig. 6.12: v_y of the NEGIS subset, Greenland: (a) Original data. (b) After the first filter step (smooth segments). (c) After the second filter step (median). (d) After the third filter step (directions)

region	points before	points after	percentage of remaining data points
Artificial flow field	49 000	39 906	81.44%
Recovery Glacier (RG)	7 748 376	6 422 695	82.89%
RG slow flowing region	563 242	442 413	78.55%
RG fast flowing region	95 280	91 092	95.60%
RG line of outliers	514 596	414 873	80.62%
RG shear margin	140 551	121 734	86.61%
Greenland	28 087 899	26 632 467	94.82%
Petermann Glacier	1 036 193	989 318	95.48%
NEGIS subset	805 170	576 362	71.58%

Tab. 6.2: Number of data points before and after application of all three filter steps in the tested regions.

6.4 Discussion

Our results demonstrate that the presented three step filtering strategy is capable to remove the majority of outliers from remote sensing derived surface velocity fields. Despite a positive qualitative impression when comparing the filtered velocity fields with the unfiltered input fields (e.g. Figures 6.3, 6.5, 6.7) a quantitative test on a synthetic velocity field with randomly included outliers revealed that the presented filtering strategy removes up to 99.67% of erroneous data points (Figure 6.1). On the other hand a maximum of valid velocity measurements is preserved throughout the filtering. While from the rather noisy velocity field of the NEGIS subset 28.42% of data points were removed by the filter, up to 95.60% of valid velocity measurements were preserved for the relatively smooth velocity field in the fast flowing region of Recovery Glacier (Table 6.2).

The three step filtering strategy applied in this study relies on several parameters which can be adjusted by the operator. In the first filter (smooth segments) these include a , w , n_{min} and σ_M . Lower values of $a \in [0, 1]$ in (6.2) would lead to a lower threshold during the classification of segments. As a result, segments would have less elements and consequently more points would be removed. A higher value can be chosen if the filtering procedure should be more defensive. Our sensitivity analysis showed that a value between 0.2 and 0.4 removes most erroneous data points (Figure 6.15). The factor w is designated to account for possible temporal changes between the a-priori velocity field and the satellite derived velocity field (Rosenau et al., 2015). It is therefore highly dependent on the expected changes in the study region. Here we propose a value of 1.5 for regions where we expect little changes between the a-priori velocity field and the raw input velocities. The number of elements in a segment to be accepted, $n_{min} = 8$, is already proposed in (Rosenau et al., 2015). We can confirm this in section 6.3.2, however, the result for

n_{min} between four and twelve seem to be very similar. A higher value of n_{min} can improve the result, if there are larger outlier areas, which are very smooth within themselves. The offset tracking error σ_M in (6.3) is dependent on the resolution and the revisiting time of the employed satellite and need to be adjusted correspondingly by the operator (e.g. McNabb et al., 2012; Seehaus et al., 2015).

In the second filter (median) the parameter ϵ_m and the size of the moving window can be changed. ϵ_m in (6.4) and (6.5) influences the threshold below which data points are deleted and therefore the amount of removed points directly. The window size should be larger than the size of the erroneous features, as otherwise the filter is not able to remove them. At the same time, the window size should depend on the resolution of the velocity field. A larger window leads to the removal of more points, causing problems especially in shear margin regions. Therefore, this parameter should be reconsidered in case of losing too much data points during the second filtering step. However, the size of the moving window plays also an important role for the computation time. If a reduction of the computation time is necessary, e.g. in the case of high resolution input data or large spatial coverage, a reduction of the window size should be considered.

In the third filter (directions), the angular threshold α in (6.7) and the size of the moving window can be adjusted by the operator. A changing value of α has the strongest effect in slow flowing areas as there are only little differences between two satellite images with a small time interval in between. Therefore, the direction of the flow cannot be detected in many cases. This problem does not appear in fast flowing areas, wherefore the strongest effect of the directional filter is evident in slow moving regions.

Previous remote sensing studies rely only on one of the presented filtering steps to exclude outliers from satellite derived velocity fields. While most large-scale studies of ice streams and ice sheets rely on filters based on local variance within a moving search window (e.g. Mouginot, Scheuchl, et al., 2012; Nagler et al., 2015), studies examining mountain glaciers also make use of directional filters employing certain angular thresholds to which neighboring data points are allowed to deviate (e.g. Scherler et al., 2008; Burgess et al., 2012). In order to find segments of continuous glacier flow Rosenau et al. (2015) implemented a gradient based filtering approach. The latter has been successfully applied on Landsat derived velocity fields for numerous outlet glaciers in Greenland (Rosenau et al., 2015).

In this study all of these approaches were connected in series. This way erroneous data points are successfully removed even if an outlier is not detected in the previous filtering step. This is evident for example in the shear margin of Recovery Glacier (Figure 6.5). In this example, 54.23% of the removed data points were detected by the first filter (smooth segments), 12.04% by the second filter (median) and 33.73% by the third filter (directions).

Our results show that the different methods used in the three filtering steps have different effects on the velocity field. While the first two steps remove clusters which

are noisy in magnitude, the last one removes data points with false flow directions. The segment filter can remove clusters, which are smooth within themselves but having an offset to surrounding points. The median filter on the other hand is capable to remove features with a smoother transition from correct to incorrect data points. We found that the order of the three filtering steps has a significant impact on the results. We therefore tested all possible arrangements and the presented procedure turned out as being most effective. The major cause for this is that the first filter relies on segments, meaning that once the second and third filter steps were removing individual points, there were less clusters and with that the first filter becomes less successful.

In this study it has been shown that the combination of three separate filtering algorithms is very effective for removing outliers from surface velocity fields. However, it should be noted that it is not possible to employ the complete filtering strategy for all settings of glaciers. This is mainly because an input to the segmentation filter is an a-priori velocity field with a good spatial coverage. In this filtering step, the difference of neighboring points in the a-priori field is taken to compute the accepted error between two points in a segment. This means that a missing value in the a-priori field would also lead to a missing value in the result, even if the corresponding value is a valid velocity measurement. For the examples shown in this study, this is not a problem as we rely on large scale high resolution ice motion fields available through the MEaSURES program. These mosaics were compiled from data of various remote sensing sources including ALOS PALSAR, Envisat ASAR, ERS-1/2, Landsat-8, RADARSAT-1/2 and TerraSAR-X and show no gaps in our study regions. For many mountain ranges no such compilations are available yet, specifically for smaller mountain glaciers. This limits the use of the smooth segment filter in these regions. However, it has been shown previously that filters based on local variance within a moving search window or a directional threshold are capable to remove many outliers in such areas (Scherler et al., 2008; Burgess et al., 2012; Heid and Käab, 2012a; Neckel et al., 2017). We therefore argue that even if the smooth segment filter fails in these areas, robust results might be obtained by employing the median filter and the directional filter.

6.5 Conclusions

We presented a new approach to filter outliers of remote sensing based glacier velocity fields. The approach consists of three individual steps, with each filter detecting different types of incorrect data points. The combination of the three filter steps leads to a robust filtering of data, so that the standard deviation of the velocity field is reduced significantly, while a reasonable number of data points (72-95%) is preserved. Velocity retrieval is particularly challenging in slow moving areas,

which leads to standard deviation values up to a factor of ten of the mean velocity. With our filter, this can be reduced to a factor of 0.5 to 1, leading to data sets with acceptable measurement errors. Also in areas of high velocities, the standard deviation is significantly reduced, leading to higher accuracy in estimates of ice discharge at grounding lines of fast ice streams and hence improved measurement of mass loss of ice sheets. As the procedure does not manipulate the values of the velocity field, no smoothing of velocity gradients occurs, which is important for glaciological applications. Due to its efficiency, this filtering processor is also suitable for future missions dealing with big data volumes.

6.6 Appendix

6.6.1 Intensity Offset Tracking

In this study surface velocities are obtained by intensity offset tracking on spatially lower resolved Sentinel-1 Terrain Observation with Progressive Scans (TOPS) Interferometric Wide swath (IW) SAR data ($\sim 2.3 \text{ m} \times 13.8 \text{ m}$ in range and azimuth) and spatially higher resolved TerraSAR-X stripmap data ($\sim 1.4 \text{ m} \times 1.9 \text{ m}$ in range and azimuth). While a full Sentinel-1 scene covers an area of approximately $250 \text{ km} \times 200 \text{ km}$ on the ground a TerraSAR-X stripmap scene is restricted to approximately $30 \text{ km} \times 50 \text{ km}$ resulting in a trade-off between spatial resolution and ground coverage between both sensors. Independent of the sensor, repeat-pass acquisitions of the respective satellite need to be available for applying intensity offset tracking. While the repeat-pass of Sentinel-1A/B takes 6 days the revisiting time of TerraSAR-X is 11 days. In a first step data from successive repeat-passes of the respective satellite are coregistered based on precise orbit information and a digital elevation model (DEM). A great advantage of this new generation of SAR satellites is that precise orbit information is aided by an on-board Global Navigation Satellite System (GNSS) receiver. Therefore, no stable ground control points or global fits are required for the initial coregistration of repeat-passes and a precise coregistration over moving ice surfaces is possible (Pritchard, 2005; Nagler et al., 2015). For each coregistered image pair offsets in range and azimuth direction are then calculated by cross correlating the backscatter intensity in predefined moving search windows (e.g. Strozzi et al., 2002). In order to improve the accuracy of the estimated shift an oversampling factor is applied to the correlation function (Jezek, Floricioiu, et al., 2009). Depending on the spatial resolution of the sensor and the anticipated ice movement between satellite passes the size of the search window is adjusted by the operator. Range and azimuth offsets are finally translated into metric surface displacements and projected into a polar stereographic coordinate system.

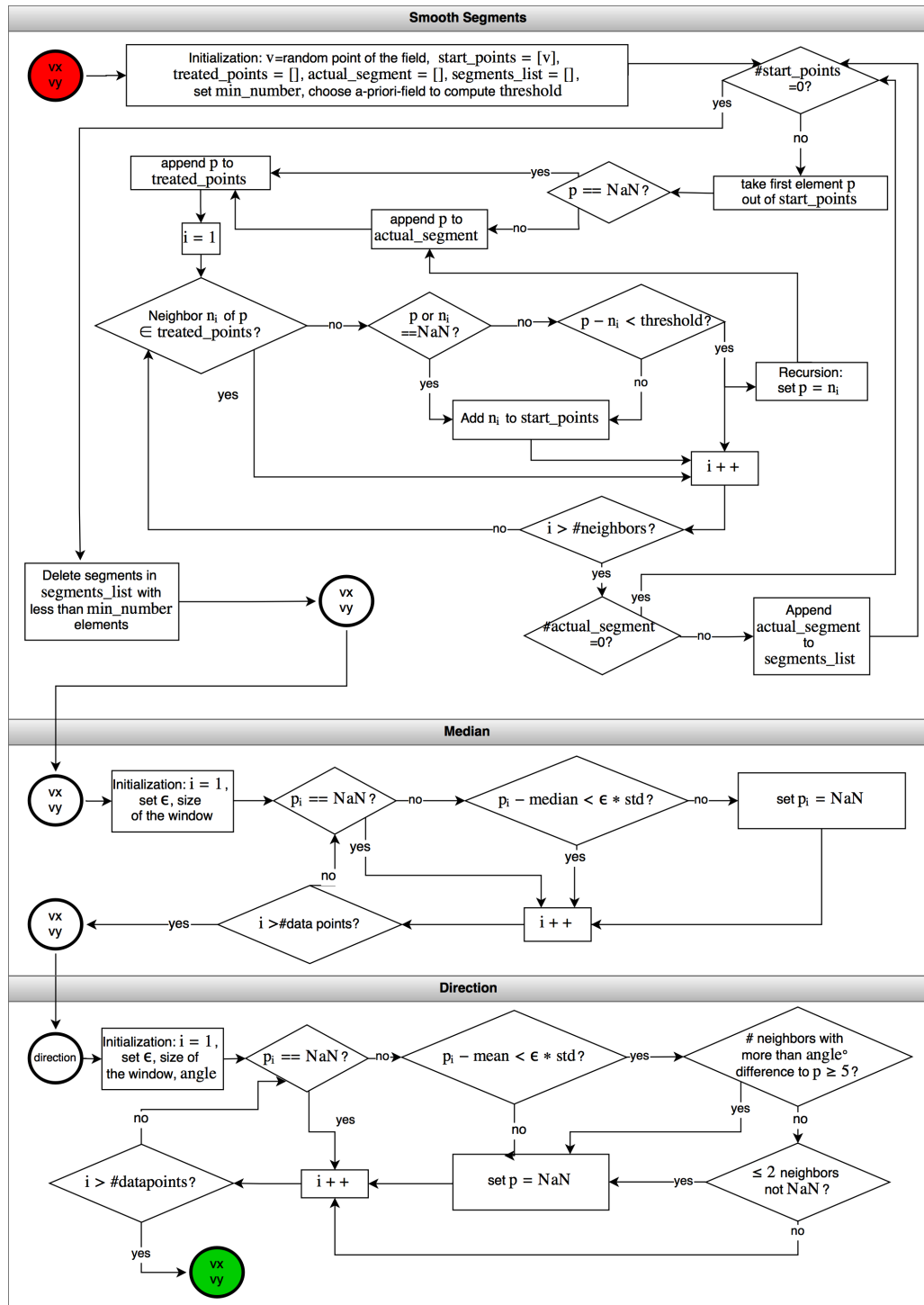


Fig. 6.13: Flowchart of the filter algorithm

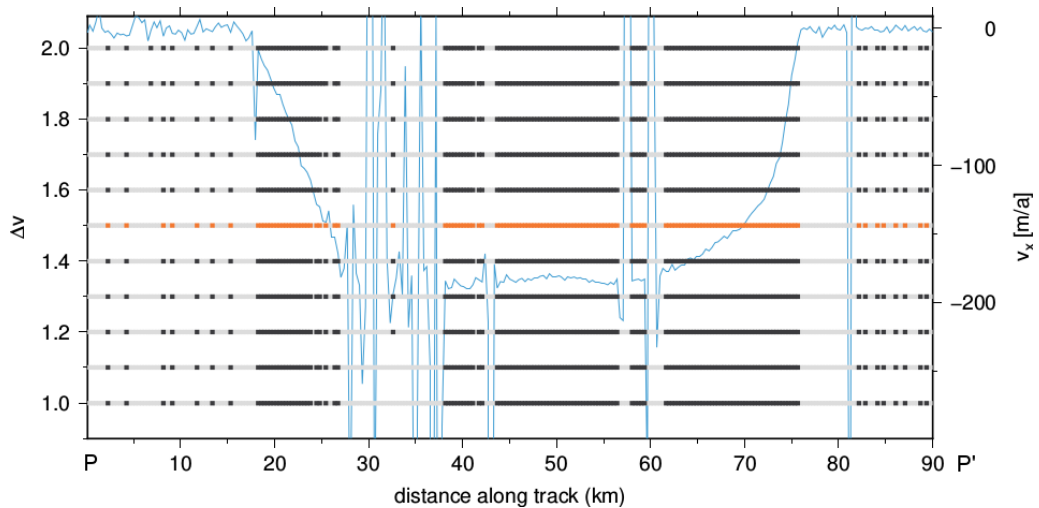


Fig. 6.14: Sensitivity of the first filter (smooth segments) to w . Data points that passed the filter are plotted as black points, while those that were removed are shown in gray color. The left y-axis represents the value of Δv , while the right axis denotes the velocity. The selected value of Δv is highlighted in orange. The blue line displays the original velocity in x-direction along the profile shown in Figure 6.3d.

6.6.2 Filter Parameter Sensitivity Tests

Here we present additional information on the sensitivity of the individual filter steps to their parameters. The graphs displayed in Figures 6.14 to 6.18 are undermining the discussion in Sections 6.3.2 and 6.4 and visualise the parameters used in our applications to glaciers in Greenland and Antarctica. Each figure displays v_x (blue color, right y-axis) along a transect crossing a glacier and hence incorporate slow and fast moving glaciers and the shear zone in their transition. The different parameter values are shown as values along the left y-axis. In all cases, data points that have been removed appear in grey color, whereas data points that passed the filter are drawn as black points, or in orange color for those filter parameter setting that has been our setting in the applications to ice sheets within this study.

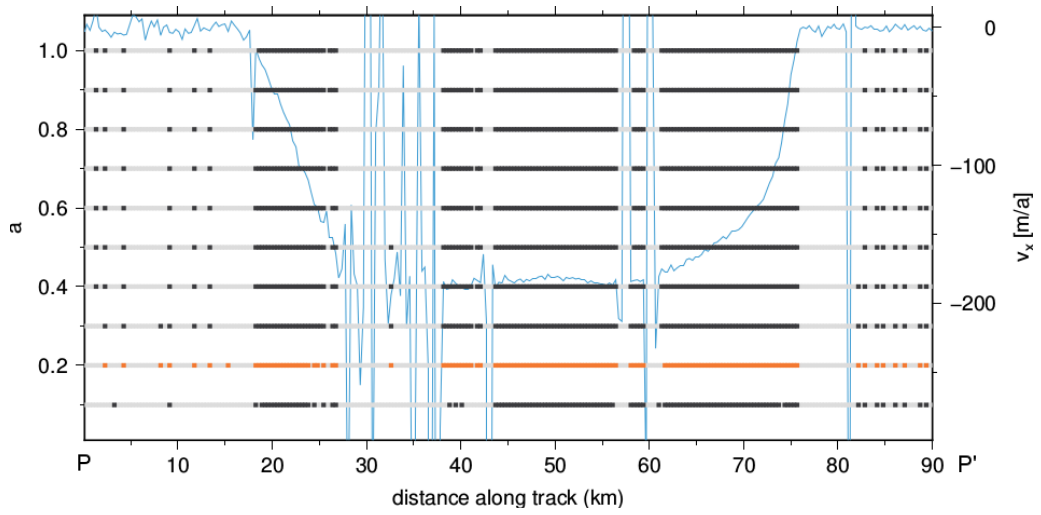


Fig. 6.15: Sensitivity of the first filter (smooth segments) to a .

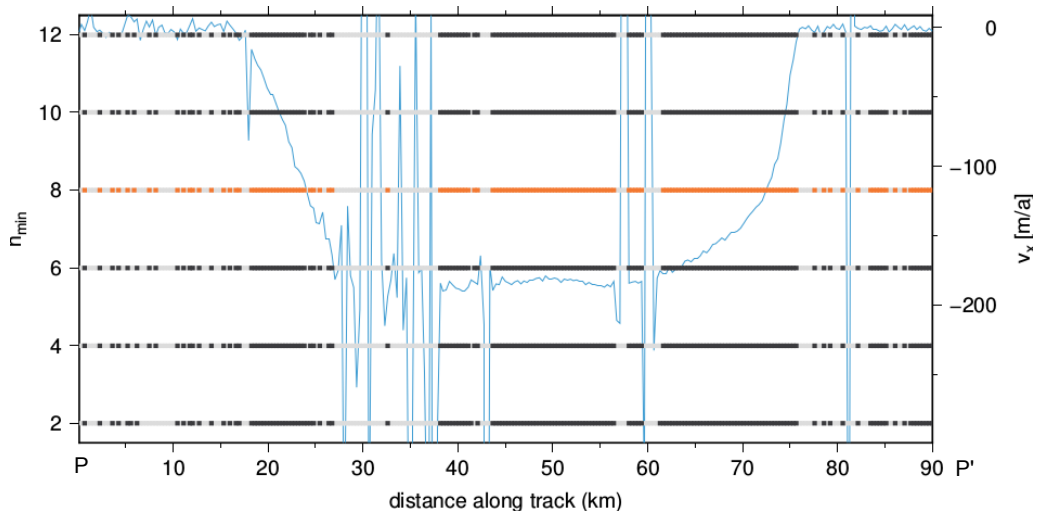


Fig. 6.16: Sensitivity of the first filter (smooth segments) to n_{min} .

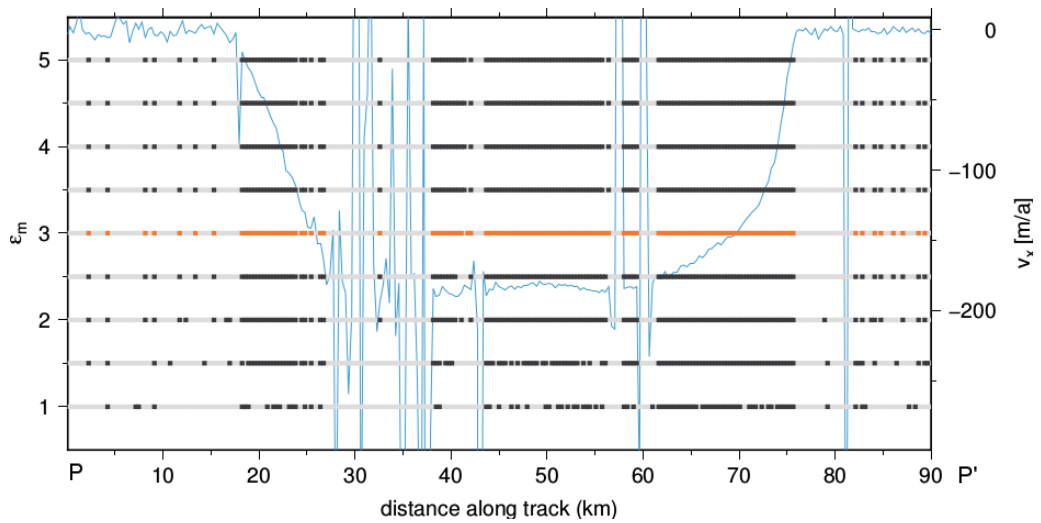


Fig. 6.17: Sensitivity of the second filter (median) to ϵ_m .

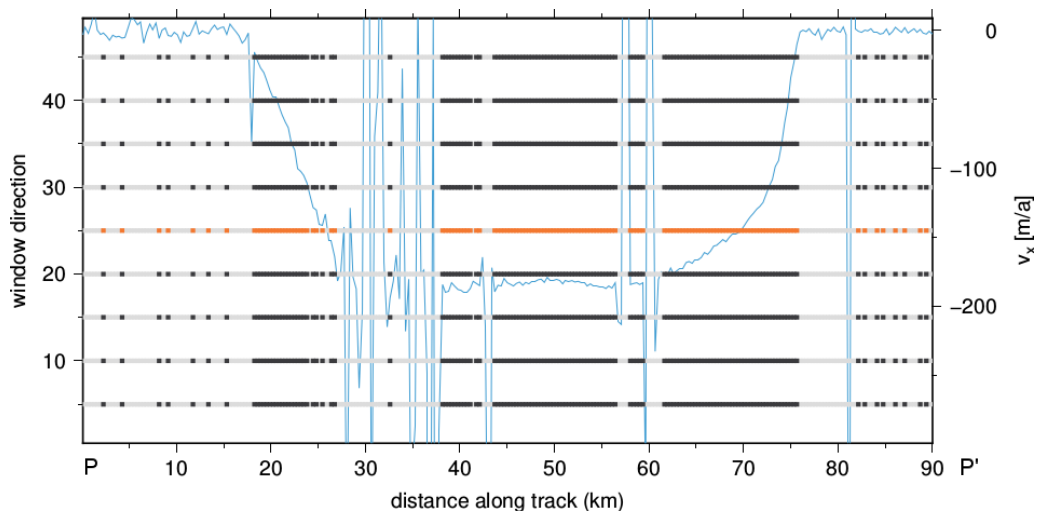


Fig. 6.18: Sensitivity of the third filter (directions) to $window_{dir}$.

An Evaluation of Gap Filling Methods for Glacier Surface Velocity Fields Derived from Remote Sensing

“ *A hole is a space where everything has been moved out so that opportunity has space to move in.*

— **CRAIG D. LOUNSBROUGH**
Author and Life Coach

Context

In Ch. 6, the TerraSAR-X velocity field covering Recovery Glacier was filtered in order to remove outliers. Unfortunately, false values in the data set are not the only problem while preparing the velocities to serve as inversion input. Data gaps are a typical problem in remote sensing derived velocity fields resulting from lack of coherence, filtering, non-overlapping satellite orbits or failures of the instruments. For many applications, inter alia basal friction inversion in ice sheet models, a grid without gaps is necessary, thus a gap filling technique is required to solve the problem. The method of choice should avoid decreasing the quality of the velocity field with the same reason why filtering was carried out: false values in the input velocity field lead to errors in the inverted basal friction.

The following paper investigates different interpolation methods testing their usefulness for application to glacier velocities: linear interpolation, minimum curvature with tension, natural neighbor interpolation and Kriging. All methods are already implemented in some software packages, but the Kriging method needs an additional speed up procedure to enable its application to big data sets. The speed up procedure was implemented in python during this work. Advantages and drawbacks of the method are balanced out against each other in order to find the best method. The methods are applied to an artificial velocity field including different gap characteristics for the purpose of quantifying estimation errors. All methods are then applied to

the complex system of Recovery Glacier. None of the investigated techniques meets all the requirements and preferences, but natural neighbor interpolation turned out to be the best choice. The resulting velocity field serves as input for the inversion. The basal friction resulting from the best interpolation will be compared to the basal friction inverted from the non-smooth linear interpolated velocities in the course of a sensitivity analysis. Thus, the influence of low quality velocity fields as a result of inappropriate interpolation will be examined.

Contributions

Conceptual design of the study was done by C.Eis consulted by A.Humbert. C.Eis designed and implemented the speed-up procedure of the Kriging method. The artificial flow field was created by C.Eis. The application of the interpolation techniques NatInt, LinInt and MinCurv using the software packages Matlab and gmt as well as the Kriging procedure on the artificial flow field and Recovery Glacier was done by C.Eis. C.Eis analyzed the results. C.Eis wrote Sect. 7.2 and 7.3 ("Materials and Methods", "Results"), which were proofread by A.Humbert. Both authors contributed to the other sections. All figures were created by C.Eis.

Authors and Affiliations

Christine Eis ¹  and Angelika Humbert ^{1,2} 

¹ Alfred-Wegener-Institute, Helmholtz Centre for Polar and Marine Research

² University of Bremen

Abstract

Velocity fields of glaciers and ice sheets are required in many applications, like assessment of changes in glacier dynamics, ice sheet mass loss or as model input data. Based on satellite remote sensing, high resolution horizontal surface velocity fields are derived. However, data gaps arising from e.g. coherence loss, are a common problem. Those gaps need to be filled, while still keeping a high accuracy of the product. Here we compare four different interpolation approaches: linear interpolation, natural neighbor interpolation, minimum curvature with tension, and Kriging. We apply the methods to an artificial velocity field for quantifying their capability. Furthermore, we study a typical application, a large ice stream in Antarctica, the Recovery Glacier. Up to 86% of the gaps can be filled with errors

less than 5%. Computational costs for a field of 6137x3074 data points range from 1 min to 14.5h. We find that the natural neighbor interpolation method is the best choice to obtain reasonably filled gaps. Data gaps along ice stream shear margins are challenging for all methods, which exemplifies that further methods need to be developed in future that are tailored specifically to those types of gaps.

7.1 Introduction

For a few decades satellite remote sensing has been used to derive horizontal surface velocity fields of glaciers and ice sheets (e.g. Rignot, 2006; Joughin, B. Smith, Howat, Scambos, and Moon, 2010). This has changed the understanding of ice sheet dynamics considerably, as individual point measurements gained from ground-based methods on ice sheets are sparse. While a simple estimation of the characteristic time scale of ice dynamics leads to 100 years, glaciers in Greenland, Antarctica and all other glaciated areas have, however, change on sub-decadal time scale as the system responds with acceleration to climate change. In addition to that, glaciers e.g. in Greenland also undergo a seasonal variation in glacier speed. Observations of surface velocities are becoming ever more important to assess the change of the natural system. The era of high resolution (3-20 m) satellites began with ERS-1/2, Landsat, Radarsat, ALOS Palsar, TerraSAR-X and is continued with the Sentinels that are sustaining Earth observation from space in the next decades. All those sensors can be used to derive surface velocities of glaciers based on interferometry or on offset tracking, either using features or speckle (Joughin, B. Smith, Howat, Scambos, and Moon, 2010; Fahnestock et al., 2015; Nagler et al., 2015; Käab et al., 2016; Mouginot, Rignot, et al., 2017).

Although, the resulting fields have a large areal coverage in general, data gaps arise. These gaps result typically from lack of coherence, removing outliers, non-overlapping satellite orbits or instrumental failures, although these issues are significantly reduced due to reduced repeat pass periods available today. Often it is necessary to fill the gaps, e.g. to use the velocity field as a model input.

There are three different approaches to do this. One approach of gap filling is data fitting, e.g. proposed in Wang et al. (2012). In general, such methods use a regression to approximate values in data gaps. Therefore, they do not fit the input data points exactly. The advantage is that these methods can also work for very erroneous data sets and work simultaneously as a smoothing. However, using such an approach features can be lost because they are smoothed out. A combination of the processing steps, filtering and interpolation, allows little control by the user. It is preferable to filter the data set in a separate step before the gap filling. Afterwards, it is more important to fit the data points instead of approximate them.

Beside the mathematical method, there are other concepts that may be engaged. New sensors such as Sentinel 1 and 2, Landsat 8 with repeated coverage may allow to fill in gaps. Mouginot, Scheuchl, et al. (2012) did apply this concept. This can, however, only be conducted if it is justified to assume that the system does not change between the acquisitions or the velocities are contemporaneously derived from different sensors. While this may be reasonable in the interior of ice sheets, it may not be appropriate for outlet glaciers in Greenland or glaciers in warmer climates with strong seasonal variability. In that case, mismatches between different fields from different times can occur. If specific surface conditions are the reason for the lack of data, none of the radar sensors may lead to retrieval of velocity and in consequence, there may be areas where such a procedure would fail. Another disadvantage of filling gaps with additional data is that this can cause a loss of quality, if the additional data are of lower quality. However, if filling gaps is appropriate, it will certainly improve the overall situation prior to e.g. an interpolation procedure and hence the goal to derive velocity fields in high accuracy from satellite remote sensing can be more likely achieved.

Another way to fill gaps is to use interpolation methods, which fill the gaps by fitting the input data exactly. If an interpolation of a field of a physical quantity is needed, there are some important requirements and preferences on the method:

1. It should fill all data gaps.
2. The input data need to be preserved.
3. The solution should be smooth, while preserving patterns (e.g. shear zones).
4. The computational costs have to be low, what enables application to huge data sets (in terms of data structure and memory).
5. An error estimation is preferable.
6. Easy handling is desirable.

To our knowledge, no interpolation procedure can fulfill all of these criteria in every case (yet), however every method has its own advantages and disadvantages. It is thus the decision of the user which method is the best for a particular application. In this paper, we aim to discuss different methods to interpolate velocity fields of glaciers derived by remote sensing data analysis. We describe the principles of linear interpolation, natural neighbor interpolation, minimum curvature with tension, and Kriging and apply the methods on an artificial flow field and a real world case with sufficient complexity, the Recovery Glacier in Antarctica. We analyse the results with

respect to different quality measures as well as the computational effort.

7.2 Materials and Methods

The problem of interpolating a velocity field derived by remote sensing can be formulated in a mathematical language as follows:

Problem. Let $\mathbf{x}_1, \dots, \mathbf{x}_n$ with $\mathbf{x}_i = (x_i, y_i)$ be a set of locations of n scattered input data points. The corresponding values are $z_i = g(\mathbf{x}_i)$, $i = 1, \dots, n$ whereby g is an underlying function $g : \mathbb{R}^2 \rightarrow \mathbb{R}$. The task is to find an interpolant $f \in H$ with $H = \{h : \mathbb{R}^2 \rightarrow \mathbb{R} \mid h(\mathbf{x}_i) = z_i \forall i = 1, \dots, n\}$. With this information it is possible to compute the value $z = f(\mathbf{x})$ at any given position \mathbf{x} including all gap locations on the grid G of the velocity field.

A number of techniques have been developed to interpolate the case of a spatial distributed quantity, e.g. linear interpolation, bi-cubic splines, radial basis functions, interpolation filters, inverse distance weighting, nearest and natural neighbors, minimum curvature and Kriging (Amidror, 2002; Spedding and Rignot, 1993; W. H. F. Smith and Wessel, 1990; Shepard, 1968; Cressie, 1990; Nogueira et al., 1997). This study presents the advantages and disadvantages of four very different approaches. We selected Kriging as a very complex technique also used in other geospatial applications. In contrast to other tools, the Kriging method provides an error estimation, which is a huge benefit. A major problem with the Kriging method is that it needs a huge amount of computational time and memory. Therefore, different advanced features were proposed, e.g. covariance tapering (Furrer et al., 2006) and optimally weighted cluster Kriging (Stein et al., 2015). This study also uses some advantages of these methods to reduce the computational costs, however this may limit the quality of the result. We will test the usefulness of the Kriging procedure in the case of glacier flow velocities and compare the results to three simpler methods: linear interpolation, natural neighbor interpolation and minimum curvature with tension.

The interpolation methods are based on weighting special points in the vector field around the point of interest. The easiest way utilized by many methods, e.g. linear interpolation, is to use only the distance between the points to compute the weights. A similarity between all distance based methods is that they assume that points close to each other are more similar than points far away from each other, under the assumption that the physical field to be interpolated is continuous. The Kriging procedure is also based on distances, but takes statistical information into account. There are also other strategies, e.g. the area based natural neighbor interpolation.

The latter two methods have the advantage that they do not put too much weight on groups of data points in a small distance. Characteristics of the methods are summarized in Tab. 7.1.

7.2.1 A Velocity Field with Artificial Gaps

In order to test the performance of the different approaches, we set up a synthetic velocity field (Figure 7.1a) with artificially distributed gaps (Figure 7.1b). This allows us to assess the capability of each interpolation method. The velocity field has a size of 1000x1000 data points with a pixel size of 1m. We simulated single missing values, stripes, a missing satellite scene (region A), and unavailable data in a shear margin (region B). The latter may be the consequence of poor data quality in these zones and is a quite typical case. In total, about 14% of the data points of the true signal are removed to create the interpolation input data (4.9% single missing values, 1.7% region A, 2% region B, 5.5% stripes).

7.2.2 Recovery Glacier

This study focuses on one real case the Recovery Glacier, situated in East Antarctica and draining into the Filchner Ice Shelf. Recovery Glacier is covering a large area between 80° S and 82° S, 10° W and 38° W, and has two side branches, the Ramp Glacier and Blackwall Glacier. With the Shackleton Range framing the area on one side and a very widespread upstream area of low flow velocities, this glacier is obeying several different types of flow regime and is thus a test case with quite some complexity. The gap characteristics include various types, ranging from small to large gaps and from round to elongated. They occur in both fast flowing and slow flowing areas and there is a lack of information in shear margins. Summarizing these points, it is a representative example for many other cases, whether in another region or on data from another sensor.

The velocity field is derived from TerraSAR-X data in 2012 and 2013 (Floricioiu et al., 2014) by applying the speckle tracking technique to 150 stripmap pairs recorded in intervals of eleven to 22 days. They have a size of 30x45 km^2 each with a resolution of 3 m. In Lüttig et al. (2017) a combination of three different filters is applied on the resulting velocity fields to remove outliers and therefore improve the quality significantly. Outliers are removed by detection of smooth segments, using the median and constraining the variability of the flow direction of nearby data points leading to data gaps at the detected locations. Afterwards the function `grdblend` of the open source software tool GMT (Wessel et al., 2013) was used to generate a mosaic covering the entire Recovery Glacier. Overlapping data points are averaged in this process. The result is a velocity field with 6137x3074 data points with a grid

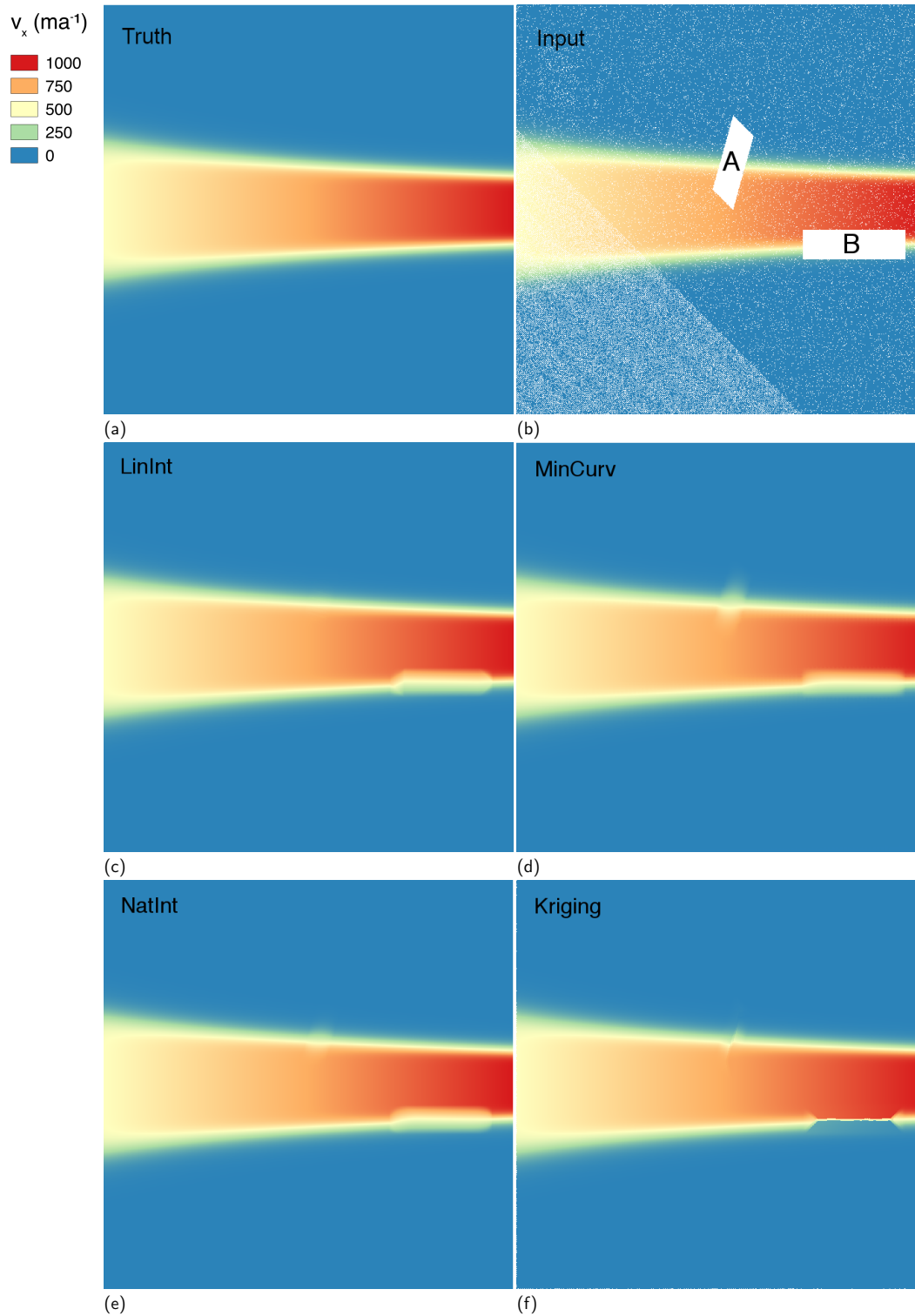


Fig. 7.1: Test case artificial velocity field. (a) Artificial velocity field serving as the true signal (Truth). (b) Test velocity field with artificially distributed gaps taken as input to test the different interpolation methods. The labeled regions should simulate a missing satellite scene (A) and missing values in the shear margins (B). Interpolated fields using (c) LinInt. (d) MinCurv. (e) NatInt. (f) Kriging.

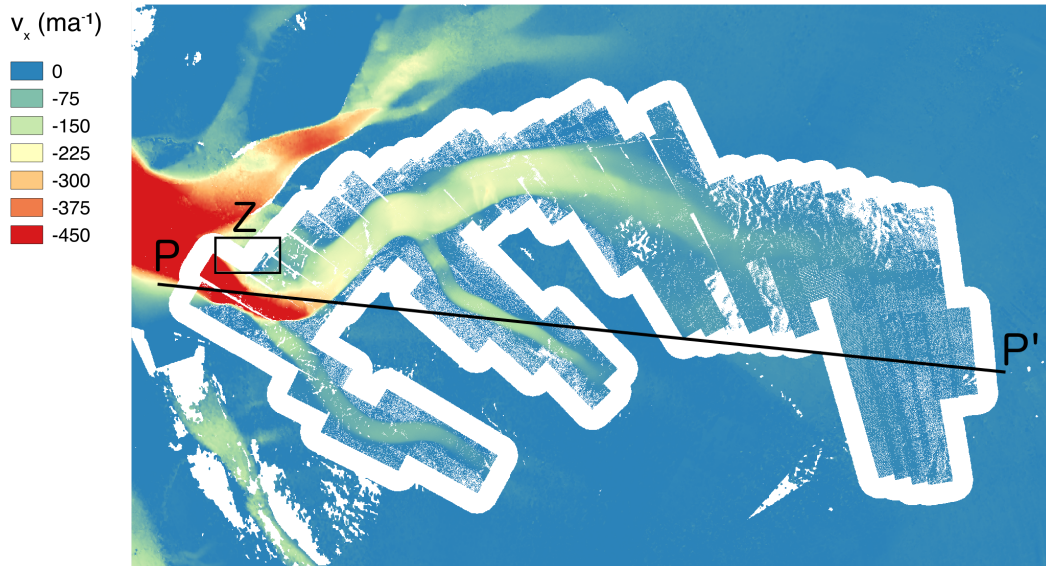


Fig. 7.2: First component of the remote sensing derived velocity data field that serves as input data for the interpolation. Location is the Recovery Glacier System, Antarctica. The Black line describes a profile from P to P'. The region marked with a rectangle will be discussed in the results section. The white color presents no data locations.

spacing of 156 m in the Antarctic Polar Stereographic coordinate system (WGS 84 / EPSG:3031).

Already before the filtering process the data set contains many gaps, which is of course enhanced while removing outliers. There is also no information available in the velocity field about the regions between the side branches of the Recovery Glacier, Blackwall and Ramp glacier. Because extrapolation outside of the convex hull of the data set leads to very erroneous results for all methods, we used as an additional information the velocity field of Rignot et al. (2011b) and Rignot et al. (2011c) at the margins of the covered area. This edge is resampled to the grid spacing of the velocity field of the Recovery Glacier and cut around it with a distance of about 25 km. The resulting input data for the different interpolation procedures can be seen in Figure 7.2. We show in all examples the first component of the velocity vector because this is the main flow direction of the Recovery Glacier. The other component is treated in the same way, but not displayed here, because the interpolation procedures do not show a different behavior applied on it.

7.2.3 Linear Interpolation

The linear interpolation method is one of the easiest ways to solve Problem 7.2. For the sake of completeness we want to give a short outline of the method. For a more detailed description, see e.g. Amidror (2002).

A linear interpolation on scattered input data points as in our case, needs a pre-processing step in which the data set x_1, \dots, x_n is triangulated. The Delauney Triangulation is the preferred method and widely used because it maximizes the minimal angle of the triangles. Therefore, the triangles are as equilateral as possible. After triangulating the data set, the interpolation procedure is applied on any interpolation point x inside the corresponding triangle. Assuming this triangle has the vertexes x_1 , x_2 and x_3 , the linear interpolator is a weighted average of the values z_1 , z_2 and z_3 :

$$z = az_1 + bz_2 + cz_3 \quad (7.1)$$

with $a + b + c = 1$. The coefficients a , b , and c are the barycentric coordinates of the interpolation point x calculated by solving the linear system of equations (7.2).

$$\begin{aligned} ax_1 + bx_2 + cx_3 &= x \\ ay_1 + by_2 + cy_3 &= y \\ a + b + c &= 1 \end{aligned} \quad (7.2)$$

In this paper, we used one of several existing implementations, the MATLAB function *scatteredInterpolant*. This function provides beside others an option to use the method *linear*. We denote this method in the following with *LinInt*.

7.2.4 Minimum Curvature with Tension

This method was introduced by W. H. F. Smith and Wessel (1990) and is a generalization of the minimum curvature interpolation. The idea is to lay a thin elastic plate with minimal strain energy through the given data points at the positions x_1, \dots, x_n . This surface is called *minimum curvature surface* and equivalent to the natural bi-cubic spline. To create any other surface interpolating the given data points, more work has to be done on it. To avoid oscillations in this surface W. H. F. Smith and Wessel (1990) established a modification which relaxed the condition on the surface that it must minimize the total curvature. For this purpose they use a tension parameter, which makes it possible to stretch the plate additionally to bending it. The method is implemented in GMT (Wessel et al., 2013), where equation (7.3) is solved to compute the values at all positions $x \in G$.

$$(1 - T)\nabla^2(\nabla^2 z) + T\nabla^2 z = 0 \quad (7.3)$$

with the tension parameter $T \in [0, 1]$. For $T = 0$ this gives the minimum curvature interpolation and a harmonic surface is calculated for $T = 1$. To avoid aliasing short wavelengths a pre-processing step has to be carried out using the GMT function *blockmean*. The procedure computes the mean position and value for every block

derived from a given block size. In the following, this method is denoted with MinCurv.

7.2.5 Natural Neighbor Interpolation

This method is another local method, also described in detail in Amidror (2002). It needs an additional pre-processing step in which the Voronoi tessellation of the data set $\mathbf{x}_1, \dots, \mathbf{x}_n$ must be found. This means that the entire plane is divided into disjoint areas. Each Voronoi polygon V_i contains only one given data point \mathbf{x}_i and only the area which is not closer to any other data point \mathbf{x}_j , which is defined in equation (7.4).

$$V_i = \{\mathbf{x} \in \mathbb{R}^2 | d(\mathbf{x}, \mathbf{x}_i) \leq d(\mathbf{x}, \mathbf{x}_j) \forall j = 1, \dots, n\} \quad (7.4)$$

with $d(\mathbf{a}, \mathbf{b})$ describing the Eukclidean distance between the points $\mathbf{a} = (a_1, a_2)$ and $\mathbf{b} = (b_1, b_2)$.

Afterwards, the interpolation position \mathbf{x} is added to the tessellation. The overlapping areas of the new Voronoi polygon V corresponding to \mathbf{x} with the areas of the old tessellation polygons V_i are taken as weights for the interpolation. This means that the natural neighbor interpolant is

$$z = f(x, y) = \sum_{i=1}^n \frac{A(V_i \cap V)}{A(V)} z_i \quad (7.5)$$

where $A(P)$ is the area of the polygon P . This procedure is implemented in the MATLAB function *scatteredInterpolant* by using the *natural* method. In the following, we denote this method with NatInt.

7.2.6 Kriging

The Kriging procedure is the best linear unbiased estimator (BLUE). It is linear because it is a weighted average of the input data z_1, \dots, z_n , the expected value of the estimator does not differ from the true value, and it minimizes the variance of the estimation error. In contrast to other methods the weights are here determined by the statistics of the input data. In this study we focus on ordinary Kriging because in this case no knowledge about the mean of the input data is needed. Therefore, the estimator is defined by equation (7.6).

$$\begin{aligned} z^* &= \mathbf{w}z \\ \sum_{i=1}^n w_i &= 1 \end{aligned} \quad (7.6)$$

with $\mathbf{w} = (w_1, \dots, w_n)^T$ and $\mathbf{z} = (z_1, \dots, z_n)^T$. The weights \mathbf{w} are chosen such that they hold equation (7.7) assuming that z is the true value at the location \mathbf{x} .

$$\begin{aligned} &\min_{\mathbf{w} \in \mathbb{R}^n} (E(z - z^*))^2 \\ &= \min_{\mathbf{w} \in \mathbb{R}^n} \left(2 \sum_{i=1}^n w_i \gamma(\mathbf{x}_i, \mathbf{x}) - \sum_{i=1}^n \sum_{j=1}^n w_i w_j \gamma(\mathbf{x}_i, \mathbf{x}_j) \right) \end{aligned} \quad (7.7)$$

where γ is called semivariogram and is defined by equation (7.8). The variogram (2γ) can be estimated by fitting a variogram model to the point cloud of variogram values over the distance of the given data points. The variogram model is often chosen as spheric, exponential or Gaussian model function. For big data sets it makes sense to use only a subset of the input data set to determine the estimated variogram to speed up the procedure. This subset can be found by choosing uniformly distributed points of the input data, however, it has to be ensured that the subset is representative for the entire data set.

$$2\gamma(\mathbf{x}_i, \mathbf{x}_j) = \text{Var}(z_i - z_j) \quad (7.8)$$

It can be shown that the solution of the minimization problem equation (7.7) leads to the interpolator equation (7.9).

$$z = \boldsymbol{\gamma}^T \Gamma^{-1} \mathbf{z}_i + (1 - \boldsymbol{\gamma}^T \Gamma^{-1} \mathbf{1})(\mathbf{1}^T \Gamma^{-1} \mathbf{1})^{-1} (\mathbf{1}^T \Gamma^{-1} \mathbf{z}_i) \quad (7.9)$$

with

$$\begin{aligned} \boldsymbol{\gamma} &= (\gamma(\mathbf{x}, \mathbf{x}_1), \dots, \gamma(\mathbf{x}, \mathbf{x}_n))^T \in \mathbb{R}^n \\ \Gamma &= (\gamma(\mathbf{x}_i, \mathbf{x}_j))_{i,j=1,\dots,n} \in \mathbb{R}^{n \times n} \\ \mathbf{1} &= (1, \dots, 1)^T \in \mathbb{R}^n \end{aligned}$$

In applications the number of data points \mathbf{x}_i can be large, which leads to a large vector $\boldsymbol{\gamma}$ and a large matrix Γ . In this case, solving equation 7.9 can be very memory consuming. Thus, it is necessary to reduce the problem to a smaller system. This means, the matrix Γ becomes a sparse matrix by setting most of its values to zero.

Thus, most of the equations of the system are cancelled. This can be achieved e.g. by defining a maximal distance $d \in \mathbb{R}$ from the location \mathbf{x} to the surrounding data points as described in equation (7.10). Only data points fulfilling the condition get a non zero value in Γ .

$$D = \{\mathbf{x}_i | i \in \{1, \dots, n\}, \|\mathbf{x} - \mathbf{x}_i\| \leq d\} \quad (7.10)$$

It is not useful to take the same value d for all searched points, as the data set may contain gaps of very different sizes. To fill also huge gaps, it would be necessary to choose a high value for d because otherwise Γ would be a zero matrix. This also means that points in very small gaps had a high value d . For points, which are closer to existing data points, many values in Γ would be non zero. Thus, Γ is not as sparse as it could be and in consequence the solution of the system of equations is more complex.

It is also not useful to take different values d for every new data point, because this would mean that the Kriging function has to be called with different parameters for every data point. This possibility would thus increase computing time strongly.

To speed up the procedure, we choose the same conditions for a set C_i of new data points. We categorize the gaps in a certain number of clusters by using three criteria for the cluster algorithm: the area, the perimeter, and the maximal width of the gaps. The maximal distance d_i for the all data points in the cluster C_i is then defined as the maximal width of all gaps in the cluster C_i .

$$d_i = \max_{j \in \{1, \dots, m\}} \{w(g_j)\} \quad (7.11)$$

with g_1, \dots, g_m gaps in cluster C_i and $w(g)$ width of the gap defined by.

$$w(g) = d((x_{min}, y_{min}), (x_{max}, y_{max})) \quad (7.12)$$

where $x_{min}, y_{min}, x_{max}$, and y_{max} describe the outer coordinates of the gap and $d(\mathbf{a}, \mathbf{b})$ the Euklidean distance between the points $\mathbf{a} = (a_1, a_2)$ and $\mathbf{b} = (b_1, b_2)$. In this way, it is guaranteed that also for the middle point in the widest gap, some data points are selected for the Kriging procedure and Γ is not empty. For some clusters, e.g. line shaped gaps, this radius can be huge and is therefore not the best choice for d_i . In this case, d_i has to be further reduced, e.g. by defining d_i as the range r of the variogram.

Another option is to select only a certain number m of nearby data points as non zero values in Γ . The disadvantage of either way of reduction of selected data points is that it can lead to sharp edges in the result, but without a reduction of the size of the problem it cannot be solved. Finding a balance between too many and too few points can be very difficult and strongly depends on the distribution of the data

Tab. 7.1: Characteristics of the four different methods.

Characteristic	LinInt	MinCurv	NatInt	Kriging
local/global	local	global	local	global
based on	distance	curvature	area	covariance
software package	MATLAB	GMT	MATLAB	R
preprocessing	triangulation	blockmean	Voronoi tes- sellation	-

points as well as the resolution of the velocity field.

After defining the subset of data points used for the cluster C_i , we applied the function *krige* of the *gstat* package implemented in R to the cluster (Pebesma, 2004; R Core Team, 2017). Thus, it is possible to interpolate the different clusters in parallel and combine them afterwards to one new velocity field with filled gaps.

7.2.7 Quality Measures

We can compute the errors of the methods applied on the artificial velocity field by calculating the difference between the interpolated values and the true signal in all gap positions, $\Delta \mathbf{v}_x = ((\Delta v_x)_1, \dots, (\Delta v_x)_n)$. We will call the mean of the absolute error $\mu(|\Delta \mathbf{v}_x|)$ and the corresponding standard deviation $\sigma(|\Delta \mathbf{v}_x|)$. Additionally, we will compute a goodness of fit $gf(\Delta v_x) = \sqrt{\sum_{i=1}^n (\Delta v_x)_i^2}$. For the Kriging procedure, an error estimation is also provided by the algorithm. A good interpolation method will achieve small values for all three statistical values. Furthermore, the solution has to be smooth, in other words, lines or other artifacts visible in the resulting velocity field are highly undesirable. For every method we will calculate how many gaps are filled with an error $(\Delta v_x)_i$ of less than 5%.

7.3 Results

7.3.1 Application to a Velocity Field with Artificial Gaps

Figure 7.1 shows the results of the four different interpolation methods. While smaller gaps are not challenging for any of the interpolation approaches, all of them show errors in the two large gaps (Figure 7.3). Region A was best interpolated by the linear approach, followed by NatInt and the Kriging procedure. MinCurv shows in this case the highest differences. This impression is additionally enhanced by erroneous values in the entire shear margins, which result from the necessary pre-processing step of the method. The other large gap labeled with B shows even worse interpolation results.

Statistic	LinInt	MinCurv	NatInt	Kriging
$\mu(\Delta v_x)$	11.68	15.68	12.3	13.15
$\sigma(\Delta v_x)$	36.22	37.62	35.39	51.05
$gf(\Delta v_x)$	1388	1487	1367	1923
$\mu(\Delta v_x)$ in A	3.02	37.16	13.07	11.49
$\sigma(\Delta v_x)$ in A	3.90	30.87	15.12	18.47
$gf(\Delta v_x)$ in A	530	5194	2149	2339
$\mu(\Delta v_x)$ in B	85.25	88.85	83.32	90.7
$\sigma(\Delta v_x)$ in B	59.43	54.47	57.27	110.52
$gf(\Delta v_x)$ in B	1387	1391	1350	1909

Tab. 7.2: Statistics of interpolation errors Δv_x with μ mean, σ standard deviation and gf goodness of fit in all gaps as well as limited to region A and B. All values in m/a .

In total, LinInt fills 85.9% of the gaps with values with an error of less than 5%, closely followed by NatInt with 83.9% and Kriging (80.2%), while MinCurv (71.2%) is substantially worse. Figure 7.4 presents histograms of the differences between interpolated velocities and original velocities in gap positions and hence, the error of the method. LinInt, MinCurv and Kriging all exhibit a peak with small differences. The MinCurv approach has more large errors in regions with a velocity smaller than $50m/a$, whereas linear and natural neighbor interpolation have better results there. Velocities between 100 and $500m/a$ are best interpolated by the MinCurv approach. Table 7.2 supports the first impression that the linear and natural neighbor interpolations give the best results, with statistical information. They have the smallest errors on average and also the smallest Euklidean norm serving as goodness of fit with regard to all gaps. In the shear margin (marked with B) NatInt can obtain the smallest values, while the Kriging procedure as already expected has the largest errors. Region A is by far best fitted by LinInt with a mean absolute error of about $3m/a$. NatInt and Kriging exhibit similar statistics in the intermediate range, while MinCurv is massively erroneous in this area.

7.3.2 Application to Recovery Glacier

Natural Neighbor Interpolation

All gaps are reasonably filled using NatInt (Figure 7.5). The interpolated field is sufficiently smooth meaning that there are no kinks in the result, although the derivative is theoretically not continuous in the data points, which leads to peaks and pits at these locations that will influence applications that require gradients of the velocity field. Features like shear zones are nevertheless preserved. NatInt has the advantage that it is based on areas and not on distances. Therefore, it

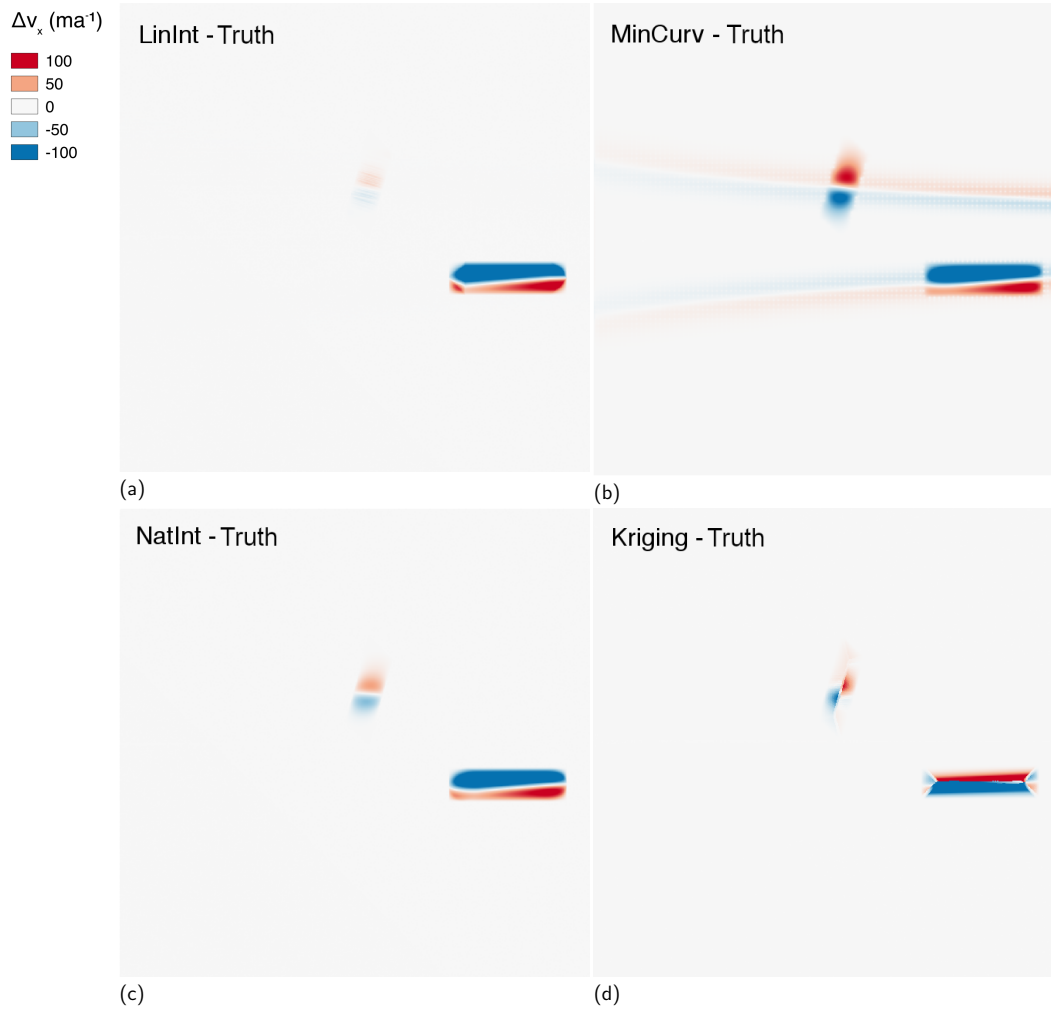


Fig. 7.3: Error of the four methods (difference between interpolated values and true signal): (a) LinInt. (b) MinCurv. (c) NatInt. (d) Kriging.

Tab. 7.3: Computational costs of the different methods (averaged over 10 runs).

Method	Computation Time [s]
LinInt	1min
NatInt	1min
MinCurv ^a	20min
Kriging ^b	14,5h

^aincluding the time needed for the pre-processing (gmt grd2xyz and gmt blockmean)

^busing three computing nodes on AWI's super computer (each has 2x Intel Xeon Broadwell 18-Core CPUs with 64GB RAM)

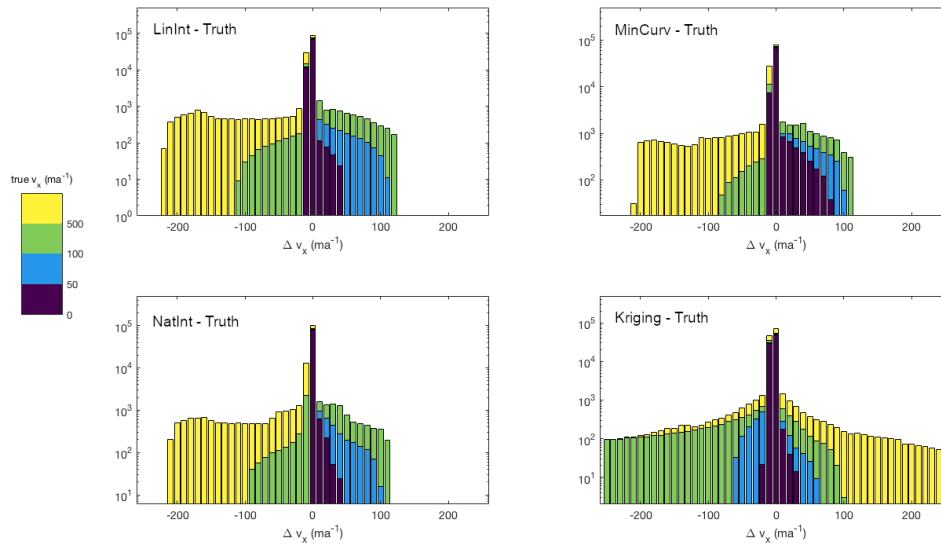


Fig. 7.4: Stacked histograms of the errors of the different interpolation procedures. The colors distinguish velocity classes of the expected result.

can compensate for data density variations and does not overweigh data clusters. The method performs well in both regions, data clusters and sparse areas, and is therefore a good choice for the investigated data set.

Linear Interpolation

The computation time of this approach is very fast, even the best we achieved in our experiments as can be seen in Table 7.3. The method is thus easy and quick to use to get a first overview. However, already a first look on the results in Figure 7.6 shows the disadvantages of the linear interpolation. In order to distinguish better between the results, we plotted the differences between the outcomes of NatInt and LinInt. Although the solution is continuous, it is not smooth, because the first derivative is not continuous between the triangles described in the methodology section. Therefore, edges of the triangles are visible in the form of lines. These discontinuities are not acceptable as a good solution and therefore the application of a linear interpolation is not useful in the case of the glacier velocity field described in the methodology section.

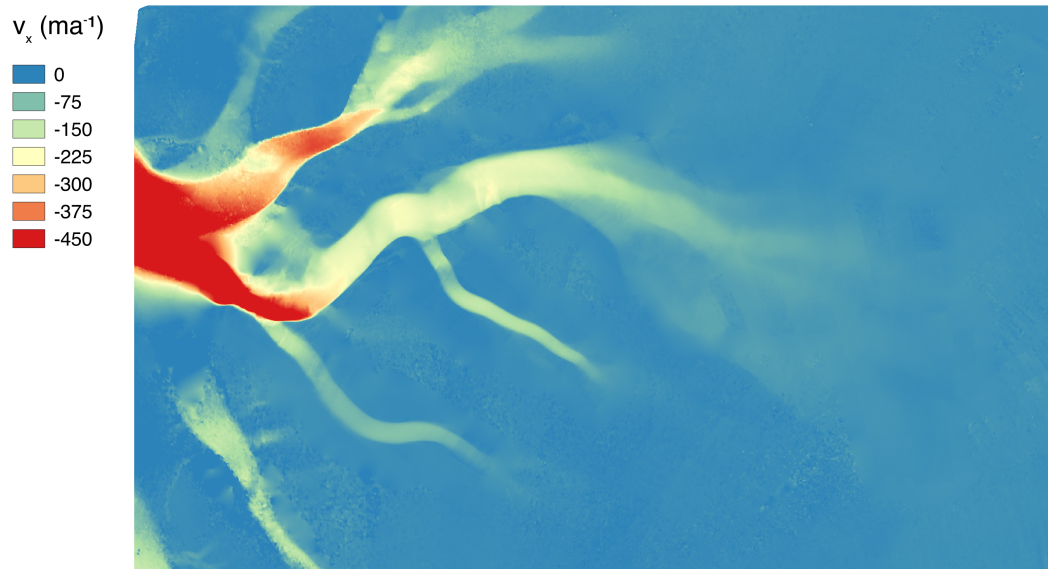


Fig. 7.5: Interpolated velocities of the Recovery Glacier using NatInt. The results of the other methods will be displayed in difference to this solution.



Fig. 7.6: Resulting velocity difference between NatInt and LinInt.

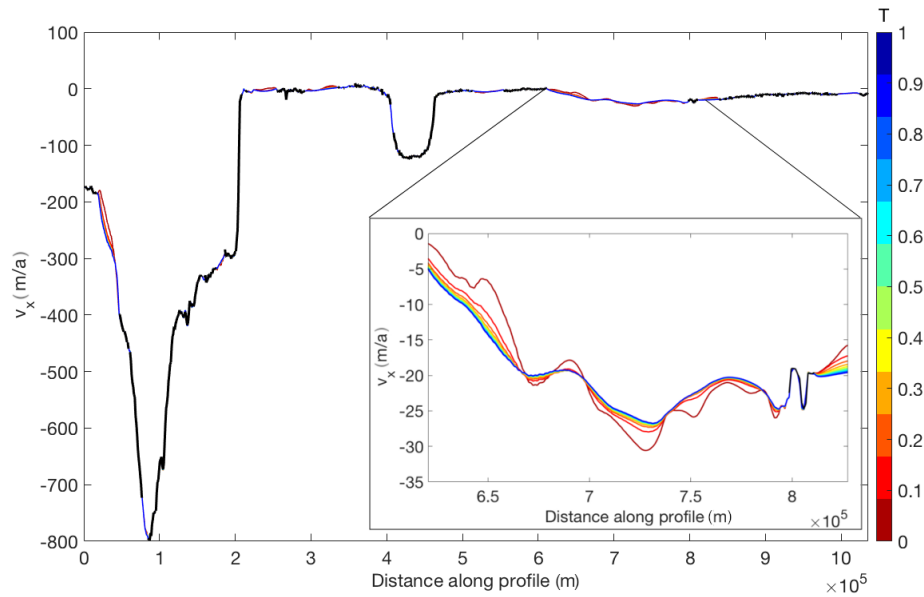


Fig. 7.7: Solutions of MinCurv with different T along the profile P - P' (Figure 7.2)

MinCurv

Because of its efficiency (Table 7.3), it is reasonable to test the method with different tension parameters T . All solutions have the similarity that they are continuous in both the interpolator and its first and second derivatives. For a small T , the plate is relatively inelastic, which leads to sharper edges in the result as can be seen in Figure 7.7. In contrast, higher values in T result in softer edges and a smoother overall appearance. We chose $T = 0.4$ in the following analysis resulting in a surface, which is very similar to a harmonic surface. Therefore, the overall appearance is smoother without losing the minimum curvature condition completely.

The procedure needs an additional pre-processing step. The *gmt* function *blockmean* computes the mean of defined blocks of the velocity field to avoid spatial aliasing. Therefore, the user has to define a block size, which has a strong influence on the results. In our analysis we chose a blocksize of 1 km. We found that in some cases, a poor choice can result in assigning the overall mean of the data set to all interpolation positions. Another effect of this pre-processing step is, although the algorithms theoretically fits all input data points, in practice, this is not the case. Changes in resolution lead to undesired deviations from the original data points, which is also indirectly visible in Figure 7.9. This figure shows the difference between NatInt and the other methods along the profile P-P' (Figure 7.2). Knowing that the other methods (especially NatInt) do not deviate from the original data points, it is clear that MinCurv does not fit the input data. In this representation it becomes also apparent how large the differences are in all parts of the glacier.

The results displayed in Figure 7.8 are very similar to those from NatInt in slow

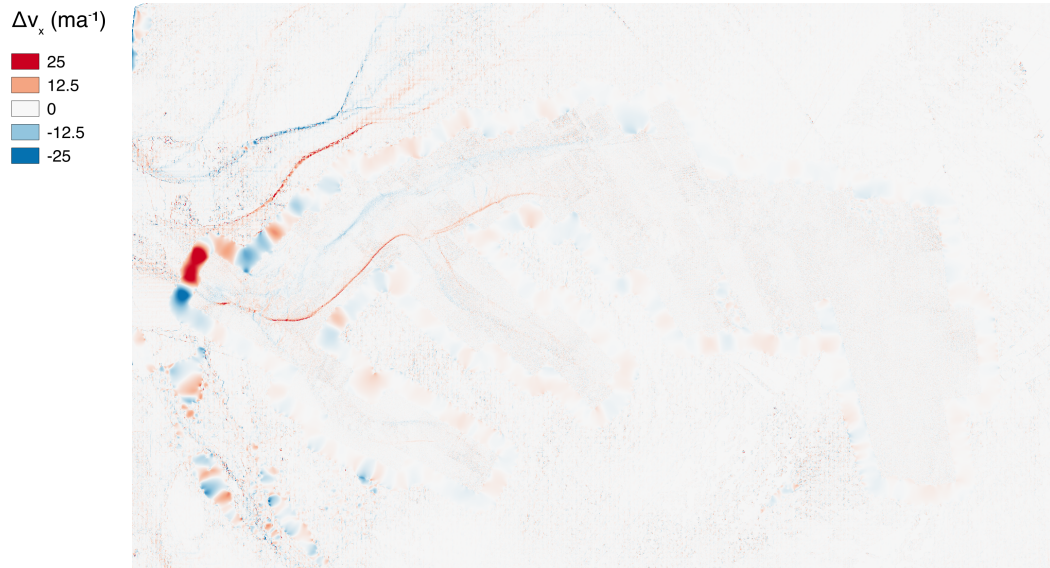


Fig. 7.8: Resulting velocity difference between NatInt and MinCurv.

flowing regions, but show a smoothing in the shear margins in consequence of the pre-processing and differences in the very fast flow.

Kriging

The results of this method are presented as differences to NatInt in Figure 7.10. It exhibits artifacts that are clearly generated by the speed-up procedure, which is required to receive a solution in an acceptable time. The borders between areas with different subsets of influencing points are visible. Therefore, the solution contains discontinuities, which should be prevented in general. Despite this, the resulting velocity field in the interior of glacier appears reasonable and there are no significant differences to other interpolated velocity fields. A great advantage is the error estimation obtained from the Kriging variance, presented in Figure 7.11. High variance values reflect high uncertainty of the solution. As expected, this is the case in wide gaps, where no input data is nearby. In contrast, smaller gaps are filled with less erroneous values.

7.4 Discussion

We begin our discussion with the assessment of the methods to the artificial velocity field, as only in this case we have a true measure to assess the quality of the interpolated fields. None of the methods can handle the sharp transition between fast and slow flow. We see slight advantages in NatInt and MinCurv. Both methods

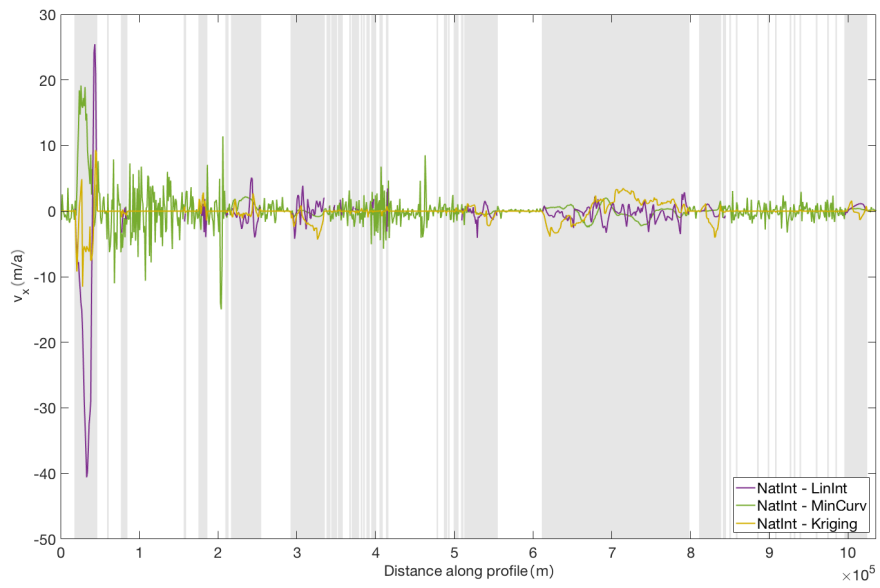


Fig. 7.9: Difference between NatInt and the other solutions along the profile P - P' (Figure 7.2)

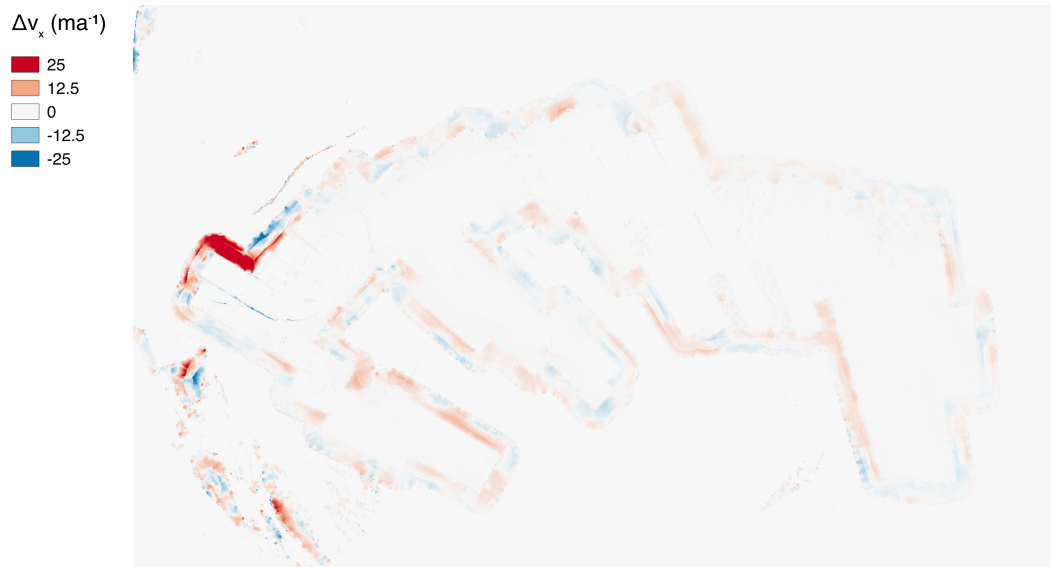


Fig. 7.10: Differences between the reference and the Kriging procedure.

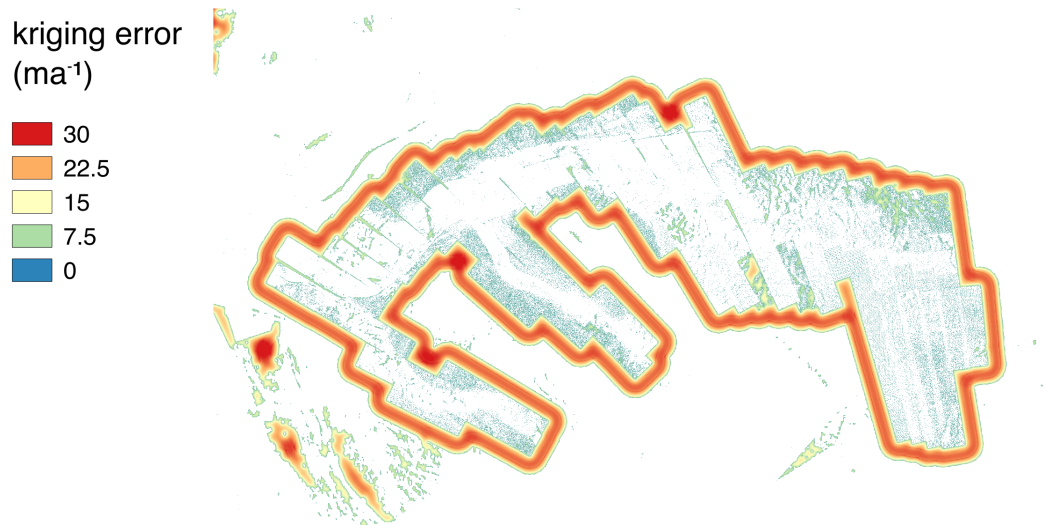


Fig. 7.11: Error estimation of the Kriging procedure: square root of the Kriging variance.

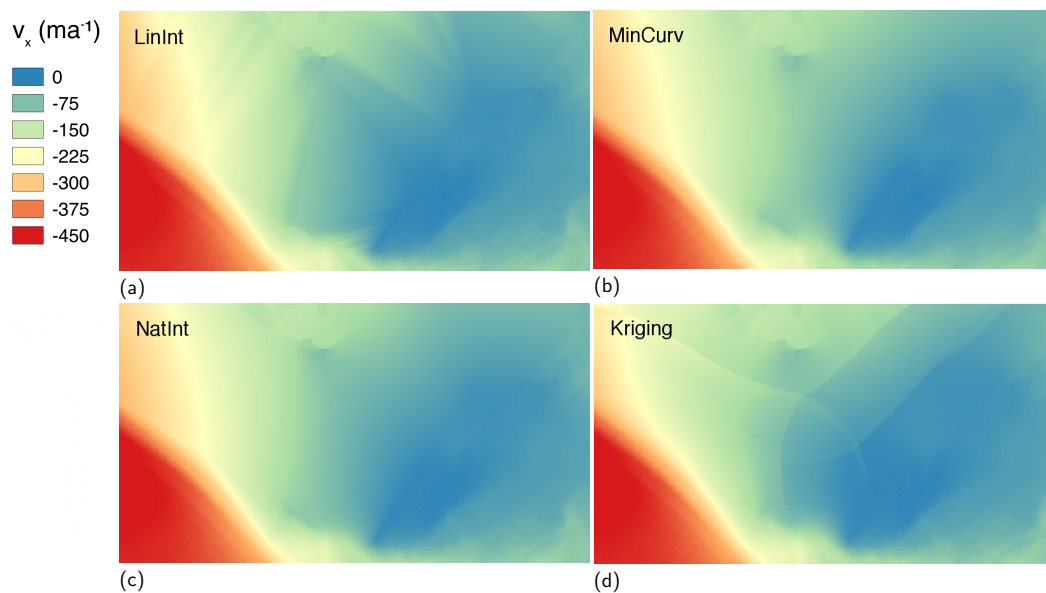


Fig. 7.12: Zoom into the area marked with Z in Figure 7.2, interpolated with the different methods: (a) LinInt. (b) MinCurv. (c) NatInt. (d) Kriging.

produce smoother edges in contrast to Kriging and LinInt. In addition, it is noticeable that the patterns of the errors are similar for all methods except for the Kriging procedure. This is also reflected in the error histograms presented in Figure 7.4, where only the Kriging result differs and has the highest errors. The other histograms indicate differences mainly in slow flowing areas.

For Recovery Glacier, all of the methods can fulfill some of the requirements described in the introduction, but none of them can comply with all the requirements. In sum, all methods work well for small gaps (few pixels), while larger gaps result in major differences. In general, the methods produce reasonable results, while existing structures are preserved. A result which can be seen as not sufficient is the one of LinInt. In this case we see many artifacts because it is not as smooth as the other solutions. Also the Kriging result is not smooth enough and clearly shows some lines, which result from speeding up the procedure as described in the methodology section. In the other cases, there are no visible discontinuities. Figure 7.12 shows clearly the differences of the methods with regard to this issue.

Another aspect are the computational costs, which vary extremely between the methods as shown in Table 7.3. While LinInt and NatInt as local methods need only one minute, Kriging takes 14.5 hours, even though we used a speed-up mechanism. MinCurv has an intermediate performance. However, the measured computation times depend on details of the implementation, e.g. the programming language, and give only a rough estimation.

The linear and natural neighbor interpolation can be utilized with minimal effort because they are already implemented e.g. in MATLAB. They lead to the same results independent from the user as they do not need the selection of an additional parameter. The MinCurv algorithm is also implemented in a toolbox, but needs the additional input parameter T and a parameter for the pre-processing step. These parameters have a great influence on the solution, thus the user has to know which solution he or she wants to receive. This is not the case for the Kriging procedure, which is however also not very easy to use in the case of big data sets. Although, the method is implemented in the R package *gstat*, it needs a speed-up to be feasible for the amount of data. To achieve this, the user needs to specify at least one parameter to define a radius of influencing points. Finding a good balance for this parameter is sometimes difficult making Kriging the worst method from this point of view.

The only method providing an error estimation of the solution is Kriging. To estimate errors of the other methods an analysis of synthetic flow fields like the first application of this paper is necessary. MinCurv does not fit the data points exactly, because an additional pre-processing step is mandatory. This samples the data to the selected block size, which leads in some areas to an undesired smoothing.

An additional disadvantage of LinInt and NatInt is that there is no possibility for extrapolation, as they are limited to the convex hull of the given data set. This is caused by the triangulation, which is necessary prior to the the proper interpolation.

Tab. 7.4: Assessment of the performance criteria of the four different methods.

Criterion	LinInt	MinCurv	NatInt	Kriging
all gaps filled	✓	✓	✓	✓
smooth	✗	✓	✓	✗
preserves input data	✓	✗	✓	✓
easy to handle	✓	✗	✓	✗
acceptable computational costs	✓	✓	✓	✗
error estimation available	✗	✗	✗	✓

In the presented case, this is a reason why additional information from another velocity field is taken into account. In regions where data coverage is sparse, this becomes an issue, but there are opportunities to overcome this: a linear extrapolation based on boundary gradients of the vector field and the nearest neighbor extrapolation. Nevertheless, both extrapolation methods would lead to very erroneous results outside the convex hull of the input data points.

Table 7.4 summarizes these findings and shows that LinInt and MinCurv are not suitable in the presented case. Also Kriging is not useful for the application, because the error estimation does not balance all its disadvantages out. However, for smaller data sets this might be the most interesting procedure. This would enable the possibility to use Kriging without a speed up procedure, what maybe improve its performance. NatInt fulfills nearly all criteria, except it does not provide an error estimation. The latter might be overcome by testing its performance with artificial fields as we presented here that mimic the characteristics of the application. Therefore, we recommend NatInt as best choice for situations similar to this study, hence the vast majority of applications of velocity fields over ice sheets, ice caps and valley glaciers.

All four methods revealed problems in particular in the shear margins. More work has to be done to overcome these challenges either by developing new techniques or by improving existing methods, e.g. the Kriging procedure. A problem for this method could be that the characteristics of the velocities in the shear margin are different from those of the interior of the ice stream. Those are in turn different from the characteristics in surrounding areas with comprehensive slow flow. However, Kriging assumes a homogeneous velocity field. A procedure which does not need this assumption has probably less problems in shear margins.

7.5 Conclusions

We compared four different interpolation methods to fill gaps in surface velocity fields derived by remote sensing: LinInt, NatInt, MinCurv and Kriging. The approaches result in partially very different solutions and not all of them are satisfying. We

found the natural neighbor interpolation to be the best compromise between low computational cost and reasonable interpolated velocity fields. Kriging, although complex and renowned is not favourable for this application.

Applying the methods to an artificial velocity field, allowed to quantify the impact on the ability to fill gaps of different characteristics. Data gaps across a shear margin, which often arise due to difficulties for the feature tracking algorithm to find a valid match, leads even with the best method to an underestimation of speed in the fast flowing area of the glacier. The glacier would thus appear more sticky in applications, like inverse modelling of basal friction parameters. The application to an artificial velocity field also demonstrated that interpretation of seasonal speed-up, e.g. in tidewater glaciers, is unlikely to be misinterpreted, as small-scale data gaps in the fast flowing parts are well represented after interpolation. This is important for upcoming satellite missions, like Tandem-L, that aim to deliver products as such as weekly velocity fields.

Our results also demonstrate that there is still a requirement for improvement of interpolation approaches in future. The impact of errors in interpolation of velocity fields on estimation of e.g. basal friction and subsequently projections of ice sheet mass loss is still to be assessed. The distribution of typical gaps in remote sensing data and the variability in remote sensing velocity fields in itself, remains challenging and deserves attention of applied mathematicians. With new missions acquiring big data in terms of spatial resolution, efficiency and hence high performance computing will in future also be a factor to be developed further.

Basal Properties of Recovery Glacier from Inverse Modelling and Observations

” *Look beneath the surface; let not the several
quality of a thing nor its worth escape thee.*

— **MARCUS AURELIUS**

Roman emperor and philosopher

Context

Basal conditions are the substance of many studies, in particular at Recovery Glacier because they are a main driver of ice dynamics. It is assumed that several subglacial lakes exist underneath Recovery Glacier fundamentally contributing to enhanced flow. Basal conditions can be derived from surface observations by inverse modelling. The following article presents inverted basal friction of Recovery Glacier and compares it with the outcome of other studies. Different lake identification criteria become involved to get a more comprehensive picture of Recovery Glacier's bed.

Furthermore, a sensitivity analysis of the inversion is carried out. For this purpose, the enhancement factor, initial and minimum values of basal friction as well as the quality of the observed surface velocity is taken into account.





All experiments are conducted with ISSM using the Higher-Order approximation of ice flow. The classical adjoint method with incomplete adjoints is used for solving the inverse problem minimizing an advanced cost function as described in Sect. 5.2. Linear and logarithmic misfit as well as a regularization are optimally weighted by parameters derived from an L-Curve analysis. Filtered and unfiltered velocity data are used as input for the inversion, interpolated on the model mesh using a bilinear interpolation as standard in ISSM and a natural neighbor interpolation, which turned out to be the best method in Sect. 7. Far upstream large effects of both the interpolation and the filter can be seen. Unfiltered data lead to much smaller values in basal friction in vast areas and patterns are clearly changed. This finding demonstrates the importance of a filtering procedure prior to the inversion. Interpolation has less influence, however near the grounding line, differences between

the methods are large. Minor effects can be seen by varying initial values and lower bounds of the controlled parameter, basal friction. The enhancement factor leading to smallest misfits in slow flowing areas is smaller as expected, $E = 0.5$, showing that the ice is too soft without considering this parameter.

Contributions

The model setup was done by C.Eis with counselling A.Humbert and M.Rückamp. All model runs were performed by C.Eis, including the sensitivity study of the enhancement factor, the initial values and lower bounds of the controlled parameter, and the quality of the input velocities, as well as the L-Curve analysis. Calculation of glaciological quantities (like basal drag, driving stress and slip ratio) and computations of the rms of the different experiments were done by C.Eis. C.Eis and A.Humbert analyzed the results and all authors discussed them. The publication text was written by A.Humbert and proofread by all co-authors. Figures 8.4, 8.16 and 8.17 were created by C.Eis, all other figures were created by A.Humbert.

Authors and Affiliations

Angelika Humbert ^{1,2} , Martin Rückamp ¹ , Thomas Kleiner ¹  and Christine Eis ¹ 

¹ Alfred-Wegener-Institute, Helmholtz Centre for Polar and Marine Research

² University of Bremen

Abstract

Recovery Glacier drains about 8 % of the Antarctic ice sheet and feeds the Filchner Ice Shelf, that is suggested to be prone to changes in the oceanic forcing in future. Recent studies have used radar data to infer basal properties in particular with respect to the existence of subglacial lakes and its role in the genesis of the ice stream. Here, we take a different approach and use inverse modelling to infer the basal friction coefficient and basal drag. We use the Ice Sheet System Model (ISSM) in higher order Blatter-Pattyn approximation. To overcome limitations in a representative temperature field, we adopted this from a spin-up using the Parallel Ice Sheet Model (PISM). Minimization of the cost function is using a high-resolution TerraSAR-X derived surface velocity field as target. We conduct an L-curve analysis and sensitivity study to ensure the robustness of the minimization. We find

alterations between high and low basal drag in the main trunk, associated with ice falls and large bedrock undulations in case of high drag and smooth basins for low basal drag. The basal friction coefficient in the onset area of the ice stream is not small, indicating non vanishing friction at the ice base, which is not conform with subglacial lakes. This backs previous studies that lack evidence for the existence of large subglacial lakes at the onset of Recovery Glacier. A shear margin, inferred from radar satellite imagery, is matching with a transition to a lower basal friction coefficient but not to patterns in basal topography. This rules out a topographically driven formation of the ice stream. Given that the Recovery Glacier is resting on a deep subglacial base, sediment basins and hence wet sediments may play an important role in the onset of this ice stream.

8.1 Introduction

Subglacial lakes are suggested as a key element for the formation of ice streams. One prominent example, where lakes were thought to play a major role, is the Recovery Glacier System (Fig. 8.1) of the East Antarctic Ice Sheet (EAIS). With this system being an important contributor of mass loss of the EAIS (Golledge et al., 2017), understanding its dynamics is crucial. The original idea (Bell et al., 2007) was that subglacial lakes at the onset of the ice stream deliver continuously water acting as a lubricant. Two approaches can be taken to understand if this is likely a driving mechanism at Recovery Glacier: (i) perform observations of subglacial water, including existence of lakes and (ii) conduct modelling studies - and use both to increase our understanding of ice stream genesis at this location.

Recovery Glacier is a particular interesting ice stream as it drains a large area (996,000 km^2 , 8 % of the area and 5 % of volume of Antarctica (Rignot, Bamber, et al., 2008)) and it reaches about 1000 km into the interior of the Antarctic ice sheet. As this glacier system is also very remote in terms of logistically accessibility, field studies are limited, highlighting the importance of remote sensing.

Radar satellites with left looking capabilities that cover areas south of $80^\circ S$ open thus a great opportunity. Among those sensors are high-resolution radar satellites RADARSAT and TerraSAR-X/TanDEM-X. Also the altimeters ICESat-1 and CryoSat-2 are able to survey this area. The RADARSAT mosaic of Antarctica (Jezek, 1999) exhibits the upstream area of the Recovery Glacier with areas that appear very smooth, similar to the appearance of Lake Vostok. This was the basis for the hypothesis of Bell et al. (2007) that these locations are large subglacial lakes. Studies of B. Smith et al. (2009) and Fricker et al. (2014) were indicating a dynamic connection between elevation changes and lake filling or drainage on time scales of

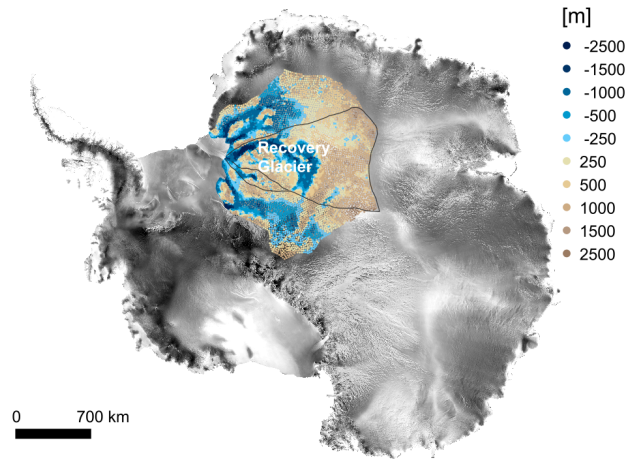


Fig. 8.1: Overview map showing the Recovery Glacier system with its drainage basin in black lines. The modelling area of this study is shown in colored dots representing the basal topography. Background image is the RADARSAT mosaic of Antarctica (Jezek, 1999).

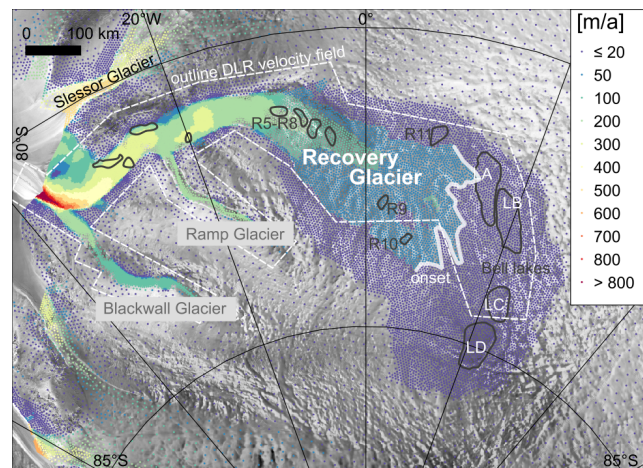


Fig. 8.2: Overview map of Recovery Glacier including proposed subglacial lake positions (black polygons). Observed velocities v_{obs} (Floricioiu et al., 2014; Rignot et al., 2011b) are presented on finite element nodes of the ISSM mesh (colored points). Dashed white line shows the outline of the TerraSAR-X derived velocity field (Floricioiu et al., 2014). The bold white line marks the approximate onset of the ice stream, defined as velocities $\geq 20 \text{ m a}^{-1}$. The dark grey polygons are previously suggested lake outlines.

a few years. Both have been challenged in a recent study by Humbert et al. (2018), of which we will use some data in this study to compare our modelling results.

The left looking capabilities of TerraSAR-X and TanDEM-X allowed coverage of the Recovery Glacier in stripmap mode (3 m resolution). Although the surface of steep ice falls within the main trunk is challenging the estimation of velocity fields, Floricioiu et al. (2014) derived a high-resolution velocity dataset. This dataset is the basis for inverse modelling in this study, after sophisticated filtering (Lüttig et al., 2017) and interpolation (Eis and Humbert, submitted, 2019). Furthermore, the

individual radar imagery allows to identify structures like crevasse fields, which can be used to infer locations of high tensile stress.

MacAyeal et al. (1995) and Joughin, MacAyeal, et al. (2004) were early studies using the classical adjoint method for inversions of surface velocity, elevation and thickness data to infer basal properties. In particular they addressed the question if large ice streams are in general resting on widespread till layers. The current generation of ice sheet models allows to conduct inverse modelling in high resolution, which has been done with a regional focus (Morlighem, Rignot, Seroussi, et al., 2010; Zhao et al., 2018; Brondex et al., 2019). In the recent past, inversions became more prominent for deriving an adequate initial state for projections of future mass loss (Goelzer et al., 2018). An introduction to inverse methods and their applications will be given below.

An early modelling study focussing on the basal shear stress of the Recovery and nearby glaciers was conducted by Joughin, Bamber, et al. (2006). However, this modelling attempt was limited by the lack of bedrock data, that only became available in the last two years. A general finding of Joughin, Bamber, et al. (2006) was that Recovery Glacier is resting on a bed that is a mixture of weak and strong bed. This is contrasting to the ice streams along the Siple Coast, which are suggested to rest on a weak subglacial till bed (Joughin, MacAyeal, et al., 2004; Kamb, 2001). This conclusion was drawn based on the difference between driving stress and simulated basal shear stress. The alternation between strong and weak spots was argued to be due to the vicinity of the Transantarctic Mountains (in contrast to the Siple Coast ice streams) and the ice stream potentially flowing alternating over mountain ranges and sedimentary basins. In the continuation, we will see, that despite the lack of bedrock constraint, this study captured quite some characteristics correctly.

A challenge for inverse modelling of basal friction is the knowledge of the viscosity and with that the temperature field of the glacier. Many applications used simplified parameterizations for temperature (e.g., Joughin, Bamber, et al., 2006; Zhao et al., 2018) or conduct a thermal spin-up with fixed ice sheet geometry in conjunction with the inversion for the basal friction coefficient (Rückamp et al., 2018). Here we use the 3D temperature and water content fields that have been derived from a coarse resolution ice sheet model with a long spin-up as in Humbert et al. (2018).

Given that gradients of the bedrock topography are influencing the dynamics of the system strongly, a decent knowledge of the bedrock topography is an important prerequisite. This became available for Recovery Glacier only in the recent past with airborne campaigns of Operation Ice Bridge (Leuschen et al., 2010, updated 2017), Forsberg et al. (2018) and Humbert et al. (2018). These surveys unveiled a

more than 1000 *km* long marine based main trunk, with a deep trough exceeding -2300 *m* about 270 *km* upstream the grounding line (Fig. 8.3). A subglacial ridge just 50 *km* away from the grounding line, will certainly influence its future retreat characteristics.

The intention of this study is to use the inverse modelling to infer the basal friction coefficient and to interpret this parameter, as well as basal shear stress, with respect to the existence of subglacial lakes at the onset of the ice stream. Also the simulated contribution of sliding in the horizontal velocity profile is used to infer areas with a wet base and/or underlying sediment.

The article is structured in the following way: we first present the mathematical model, introduce the inversion approach, and lay out the model setup, before we present the modelling results and compare them with data formerly presented in Humbert et al. (2018).

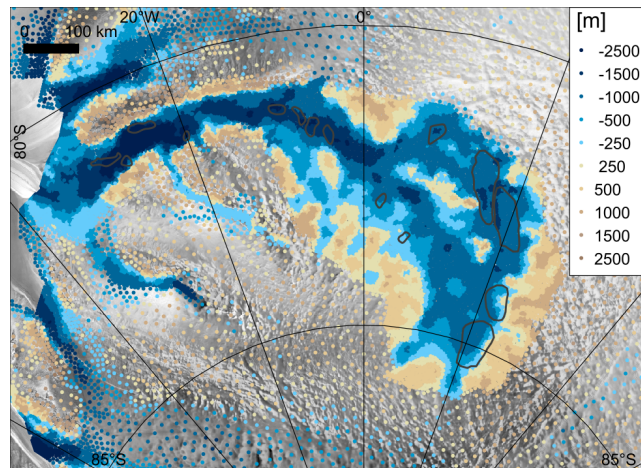


Fig. 8.3: Basal topography in the modelling domain shown at the nodes of the finite element mesh. The dark grey polygons are previously suggested lake outlines.

8.2 The Modelling Approach

8.2.1 Balance Equations

The mass balance for incompressible ice (omitting firn) is written as

$$\operatorname{div} \mathbf{v} = 0 \quad (8.1)$$

with the glacier velocity field $\mathbf{v} = (v_x, v_y, v_z)$.

The momentum balance assumes acceleration, horizontal gradients of the vertical velocities and bridging effects (variation of horizontal shear stress along the direction of shear) to be negligible (Blatter, 1995; Pattyn, 2003). The resulting elliptical system of equations for the horizontal velocities represents an elliptical system of PDEs with two unknowns and reads as

$$\begin{aligned} \frac{\partial}{\partial x} \left(4\eta \frac{\partial v_x}{\partial x} + 2\eta \frac{\partial v_y}{\partial y} \right) + \frac{\partial}{\partial y} \left(\eta \frac{\partial v_x}{\partial y} + \eta \frac{\partial v_y}{\partial x} \right) + \frac{\partial}{\partial z} \left(\eta \frac{\partial v_x}{\partial z} \right) &= \rho_i g \frac{\partial h_s}{\partial x} \\ \frac{\partial}{\partial x} \left(\eta \frac{\partial v_x}{\partial y} + \eta \frac{\partial v_y}{\partial x} \right) + \frac{\partial}{\partial y} \left(4\eta \frac{\partial v_y}{\partial y} + 2\eta \frac{\partial v_x}{\partial x} \right) + \frac{\partial}{\partial z} \left(\eta \frac{\partial v_y}{\partial z} \right) &= \rho_i g \frac{\partial h_s}{\partial y} \end{aligned} \quad (8.2)$$

with η the viscosity of ice, $\rho_i = 917 \text{ kgm}^{-3}$ the density of ice, g the norm of the acceleration due to gravity and with h_s the ice surface topography. This hydrostatic approximation is often referred to as Longitudinal Multi Layer stress approximation (LMLa) as introduced by Hindmarsh (2004). The vertical velocity v_z is computed from integration over the mass balance equation after the linear system of equation from Eq. 8.2 is solved.

$$v_z = v_z|_{z=h_b} - \int_{h_b}^z \left(\frac{\partial v_x}{\partial x} + \frac{\partial v_y}{\partial y} \right) dz' \quad (8.3)$$

with h_b the basal topography.

8.2.2 Boundary Conditions

The ice surface is assumed to be traction free. At the base the ice experiences friction and hence the stress boundary condition in tangential direction at the base is a sliding law, that leads to vanishing basal drag at the grounding line. Furthermore, the impenetrability condition holds at the base of the ice sheet. Together, the boundary condition of the momentum balance at the base reads as

$$(\boldsymbol{\sigma} \cdot \mathbf{n}) \cdot \mathbf{n} = -\rho g H \quad (8.4)$$

$$(\boldsymbol{\sigma} \cdot \mathbf{n}) \cdot \mathbf{t}_1 = \tau_{b,1} = -k^2 N v_{b,1} = -\alpha^2 v_{b,1} \quad (8.5)$$

$$(\boldsymbol{\sigma} \cdot \mathbf{n}) \cdot \mathbf{t}_2 = \tau_{b,2} = -k^2 N v_{b,2} = -\alpha^2 v_{b,2} \quad (8.6)$$

$$\mathbf{v} \cdot \mathbf{n} = 0 \quad (8.7)$$

with the basal drag coefficient k estimated by the inversion presented below, the basal friction coefficient α^2 , the effective normal pressure N , the basal drag $\boldsymbol{\tau}_b^\parallel = (\tau_{b,1}, \tau_{b,2})$ and the basal velocity $\mathbf{v}_b^\parallel = (v_{b,1}, v_{b,2})$. The basal drag and velocity are

two-dimensional vectors acting in the basal tangential plane. The sliding relation in Eq. 8.5 and Eq. 8.6 is implemented in ISSM for the LMLa scheme as (Morlighem, Seroussi, et al., 2013):

$$\boldsymbol{\tau}_b = -k^2 N \mathbf{v}_b, \quad (8.8)$$

where $\boldsymbol{\tau}_b = (\tau_{b,x}, \tau_{b,y})$ and $\mathbf{v}_b = (v_x, v_y)|_{h_b}$ are the basal drag and the basal velocity in the horizontal plane. Low values of k are associated with low basal shear stress and large contribution of sliding, which is why in the following a focus of the study is on the interpretation of k with respect to subglacial lakes and ice stream dynamics. N is a function of the ice overburden pressure P_i and water pressure P_w

$$N = P_i - P_w \quad (8.9)$$

with $P_i = \rho_i g H$. Assuming a hydrological connection between the subglacial drainage system and the ocean, the water pressure becomes

$$P_w = \min(\rho_w g h_b, 0) \quad (8.10)$$

and $\rho_w = 1028 \text{ kg m}^{-3}$ the density of sea water.

Along all lateral margins the momentum balance is completed by a Dirichlet boundary condition for the horizontal velocities which is set to the observed velocities treated as plug flow.

8.2.3 Constitutive Relation

The constitutive equation is given by a Norton-Hoff type power law, namely the Glen-Steinemanns flow law

$$\eta = \frac{1}{2} A(T, W)^{-1/n} E^{-1/n} d_e^{(1-n)/n}. \quad (8.11)$$

The rate factor A depends on temperature T and microscopic water content W following an Arrhenius relation (Cuffey and Paterson, 2010). The enhancement factor E accounts for any softening due to other than thermodynamic factors. If not

mentioned otherwise, the enhancement factor is set to 0.5. The exponent n of the flow law is assumed to be 3.

The second invariant of the strain-rate tensor, d_e becomes in LMLa

$$d_e = \left(\left(\frac{\partial v_x}{\partial x} \right)^2 + \left(\frac{\partial v_y}{\partial y} \right)^2 + \frac{\partial v_x}{\partial x} \frac{\partial v_y}{\partial y} + \frac{1}{4} \left(\frac{\partial v_x}{\partial y} + \frac{\partial v_y}{\partial x} \right)^2 + \frac{1}{4} \left(\frac{\partial v_x}{\partial z} \right)^2 + \frac{1}{4} \left(\frac{\partial v_y}{\partial z} \right)^2 \right)^{1/2} \quad (8.12)$$

and enables strain-thinning of the non-Newtonian fluid.

8.2.4 Inversion

The inversion infers the basal drag coefficient k by minimizing a cost function, which calculates the misfit between modelled v_{mod} and observed horizontal surface velocities v_{obs} . The cost function consists of three parts: one contribution J_1 of a linear misfit optimizing basically fast flowing areas, one term J_2 that optimizes slow flowing areas by controlling a logarithmic misfit and one regularization term J_3 that penalizes oscillations in k . The terms read as

$$J_1 = \int_{\Gamma_s} \left(\frac{1}{2} (v_x^{\text{mod}} - v_x^{\text{obs}})^2 + \frac{1}{2} (v_y^{\text{mod}} - v_y^{\text{obs}})^2 \right) d\Gamma_s \quad (8.13)$$

$$J_2 = \int_{\Gamma_s} \left(\log \left(\frac{\sqrt{v_x^{\text{mod}^2} + v_y^{\text{mod}^2} + v_{\text{min}}}}{\sqrt{v_x^{\text{obs}^2} + v_y^{\text{obs}^2} + v_{\text{min}}}} \right) \right)^2 d\Gamma_s \quad (8.14)$$

$$J_3 = \int_{\Gamma_b} \frac{1}{2} \|k\|^2 d\Gamma_b \quad (8.15)$$

$$J = \gamma_1 J_1 + \gamma_2 J_2 + \gamma_3 J_3 \quad (8.16)$$

The cost function gradient is calculated in ISSM using the classical adjoint method with incomplete adjoints (Morlighem, Seroussi, et al., 2013). This means the viscosity is assumed to be linear in the inversion. The minimization problem is solved using the M1QN3 algorithm (Gilbert and Lemar chal, 1989).

8.3 Model Setup

The simulations are carried out using the Ice Sheet System Model (Larour et al., 2012) in higher order Blatter-Pattyn approximation (Blatter, 1995; Pattyn, 2003). The domain is defined by ice divides based on Rignot et al. (2011a) (Fig. 8.1), but extends outside our main focus region of the Recovery Glacier system. This has been done in order to avoid influences of boundary conditions on our interpretation. We only simulate the grounded area. We use ice thickness data from several recent airborne radio-echo sounding campaigns conducted in the Recovery Glacier area, namely RECISL (Humbert et al., 2018), ICEGRAV (Forsberg et al., 2018; Ferraccioli et al., 2018) and Operation IceBridge (Leuschen et al., 2010, updated 2017) to derive a new regional ice thickness grid. This grid is then incorporated into the Bedmap2 (Fretwell et al., 2013b) dataset that is only based on IceBridge data in the Recovery Glacier area. To produce the bedrock elevation dataset the ice thickness grid is subtracted from the Bedmap2 surface elevation. The details of the applied methods are given in Humbert et al. (2018).

TerraSAR-X derived surface velocities (Floricioiu et al., 2014) are filtered in order to remove outliers using the method presented in Lüttig et al. (2017). Because the resulting mosaic does not cover the entire drainage basin, the field is completed by velocities from Rignot et al. (2011b) and afterwards linearly interpolated onto our mesh. Please note, that we test in the following the sensitivity of the filtering and interpolation method.

The system is not modelled in a thermo-mechanical coupling, but we engage a temperature and water content field that has been achieved in a spin-up with the 3D thermomechanical Parallel Ice Sheet Model (Bueler and Brown, 2009)[v0.6.2]. The model is forced with surface skin temperature and surface mass balance from RACMO 2.3/ANT (van Wessem et al., 2014, multi-annual mean 1979 – 2011) and the geothermal heat flux dataset from Shapiro and Ritzwoller (2004). After initialization, a short relaxation period and a purely thermal spin-up (fixed geometry), the model runs for 124 *ka* in its hybrid shallow-shelf/shallow-ice mode (SSA+SIA). During this stage the geometry is free to evolve including ice thickness, calving front and grounding line. Details of the setup are described in Humbert et al. (2018). The PISM fields of temperature and water content are mapped from the regularly spaced 10 *km* finite-difference grid with 101 *z*-layers to the unstructured finite-element mesh (refined towards the base; 14 *m* basal layer thickness) using a piecewise cubic Hermite interpolation in the vertical and a bilinear interpolation in the horizontal. As the geometries of the PISM spin-up deviates to the data assembled geometry used here, the vertical profiles are stretched or compressed, respectively.

8.3.1 Numerics

Model calculations are performed on an horizontally unstructured grid which is refined in areas of faster ice flow and in the Bell-lake area (shown in Fig. 8.2). The vertical discretization comprises 15 layers refined towards the base to capture vertical shearing at the base. The final mesh is formed by prism elements with a median edge length of 4824 m resulting in 761852 elements. This mesh is used for the 'best-fit' simulation and the interpretation of the basal drag and friction coefficient pattern and further glaciological quantities. For the numerous sensitivity tests and L-curve analysis presented below we generated a coarser mesh to keep the computational amount manageable. This mesh comprises in total 699538 elements.

We use Lagrange P1 elements. For solving the nonlinear system we employ a Picard iteration scheme. For the remaining linear systems of equations, we make use of the iterative GMRES solver with an Additive Schwarz preconditioner provided by the PETSc package. For the linear system, we apply convergence criteria (Larour et al., 2012) on (i) the linear system ϵ_{res} of 0.1 and (ii) solution vector ϵ_{rel} as relative residuum of 0.1. Compared to Larour et al. (2012) our stopping criteria is much larger in order to speed up the computation. However, at the last inversion steps the mechanical stress equilibrium is much lower than the recommended value of $\epsilon_{\text{res}} = 10^{-4}$. We tested a convergence criterion of $\epsilon_{\text{res}} = 10^{-4}$ for our 'best-guess' setup and found that the results are not influenced by this, while it doubles the computation time.

To solve the optimization problem we used the M1QN3 algorithm with a maximum number of iterations and function evaluations of 200. Two points with a difference of less than 10^{-5} in the uniform norm are considered to be identical during the line search. We apply a gradient relative convergence criterion $\|g(X)\| = \|g(X_0)\| < 10^{-5}$ for the inversion.

8.3.2 Experimental Setups

We conduct a series of inversion sequences (a total amount of 51), with different foci:

- (i) obtaining an L-curve by a series of simulations of a suite of γ_1 - γ_3 ,
- (ii) suites for enhancement factor E, for initial values k_{ini} and lower bounds k_{min} of the friction parameter k ,

- (iii) testing the influence of the interpolation method and filtering from observed velocities by conducting a series of simulations using the best guess inversion parameters.

This is conducted in a cascade, in which first the L-curve is obtained and an optimal parameter set for γ_1 - γ_3 is selected and is used in all subsequent runs.

8.4 Results

8.4.1 Optimal Parameter Choice and Sensitivity Tests

In order to ensure a smooth velocity field an L-curve analysis is performed (with $E = 0.5$) to find the optimal parameter for the Tikhonov regularization (J_3). Figure 8.4 displays J_3 over J_1 and the logarithmic misfit J_2 in color. The distribution demonstrates a smooth curve, from which $\gamma_1 = 10$, $\gamma_2 = 10^{-2}$ and $\gamma_3 = 5 \cdot 10^{-8}$ are selected as optimal parameter set. This set is chosen to prevent too large oscillations in k but still reveal a good match to the observations.

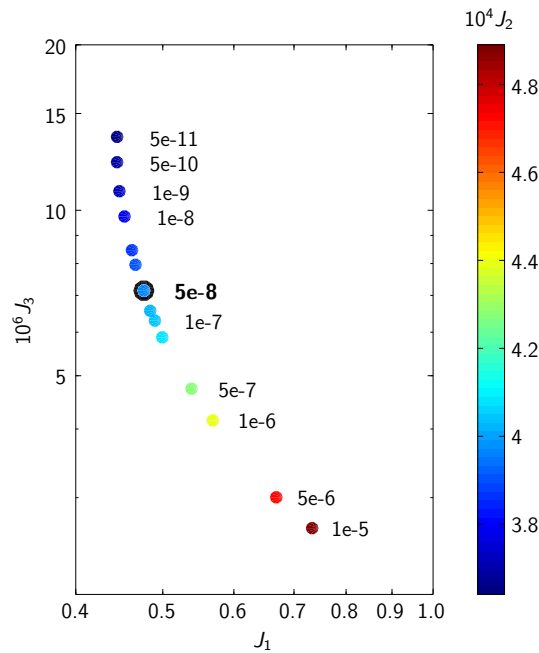


Fig. 8.4: L-Curve: log-log plot of the cost function J_3 with respect to J_1 . The logarithmic misfit J_2 is in color, while the different values of the Tikhonov parameter, γ_3 are annotated. The selected optimal parameter combination is highlighted with a black circle.

Based on the selected parameters γ_1, γ_2 and γ_3 we test the effect of using a filter to remove outliers in the observed velocities. Therefore, we conducted the inversion

with a differing input field. We directly merged the data sets of Floricioiu et al. (2014) and Rignot et al. (2011b) without previous filtering and mapped them to our mesh using bilinear interpolation. The resulting inverted parameter k shows large differences between with and without filtering in extensive parts of Recovery Glacier (Fig. 8.14). As filtering is removing outliers, the resulting field using a filter is less variable leading to a smoother k . This shows clearly the need of filtering observed velocities before using them as inversion input.

Testing the effect of the interpolation method is aiming to understand how gaps in the remote sensing velocity field affect the inverted basal drag coefficient in general. It is also conducted to clarify if any drawbacks in this field influence our interpretation of the basal drag coefficient with respect to the basal properties. In another study (Eis and Humbert, submitted, 2019) we were testing different interpolation techniques using artificial datasets, as well as the velocity field that we use in this study, and came to the conclusion that natural neighbour interpolation (natint) is best suited for the interpolation. Here we compare a bilinear interpolation (linint) with natint. The comparison is, however, done with the interpolated values at finite element nodes, thus indeed directly in the finite element framework, not as an interpolation onto a regular grid that is then subsequently interpolated onto nodes. The results are shown in Fig. 8.15. Close to the grounding line, the effect is large, as well as very far upstream (not shown here). This is expected in the vicinity of the grounding line, as it is highly crevassed and velocity data might even after filtering contain outliers. The low velocities in the very far upstream areas are naturally leading to high changes in k , as sliding is only a minor contribution and small changes in the horizontal velocities v_x and v_y will not be smoothed out by the interpolation.

The deformational part of the overall velocity field is basically fixed by the temperature and water content field retrieved from the PISM results. To test the influence of the viscosity we vary the enhancement factor (Eq. 8.11) by conducting simulations with $E = [0.5, 0.75, 0.9, 0.95, 0.99, 1.0, 1.01, 1.05, 1.1, 1.25, 1.5, 2, 2.5, 3.0, 3.5, 4.0]$. Note that smaller values of E describe stiffer ice. We find the best root mean square (rms) of differences between modelled and observed surface velocities in slow moving areas (observed velocities smaller than 50 m a^{-1}) with $E = 0.5$ (Fig. 8.16), however, there is only a minor difference to $E = 1.0$. In the region of interest, which is the outline of the TerraSAR-X velocity field, the effect is even smaller. This exemplifies that the ice is either too soft or about correctly stiff considering the temperature and water content effect only, but enhancement factors of $E = 3$ are unlikely.

Next we aim to test if the choice of the initial values k_{ini} is affecting the minimum that the inversion approaches and if that leads to significantly different distributions of the basal friction parameter. For this purpose, a list of initial values is chosen

$k_{ini} = [1, 5, 10, 25, 50, 75, 100, 125, 150] \text{ (s/m)}^{1/2}$ and the rms of the velocity differences is evaluated (Fig. 8.17). For higher initial values, the effect of the particular initial values is minor, which is to be expected, as all represent low sliding, however, starting with a very low k_{ini} leads to a low k everywhere, which is unreasonable (and is therefore not included in the figure). The best rms of velocity differences is obtained with $k_{ini} = 100 \text{ (s/m)}^{1/2}$. The last sensitivity study estimates the effect of the allowed minimum value k_{min} for k during the inversion. The tested range comprises $k_{min} = [0.1, 1, 5, 10] \text{ (s/m)}^{1/2}$. The influence of this parameter on the result is negligible, however, we find a minimum value $k_{min} = 0.1 \text{ (s/m)}^{1/2}$ to best fit the observed velocities (Fig. 8.17).

We were testing several setups that are not presented here. In particular, we were testing, if an a priori estimate of the friction coefficient for an initial field for k would lead to another minimum in the optimization with distinct different characteristics in the distribution of k . We followed Morlighem, Seroussi, et al. (2013, Eq. 31) and found, that the resulting k does not change considerably. This is increasing the confidence that both basal drag and friction coefficient are in the upstream area quite robust.

For the optimal parameter set, we present in Fig. 8.5 the simulated surface velocities and in Fig. 8.6 the difference to the observed velocity field. The general pattern of the flow field is represented reasonably, however, it becomes obvious, that in the faster parts of the Recovery main trunk, there are substantial differences to the observed velocities, as well as in the inflow from Ramp and Blackwall glaciers. Differences in the main trunk are associated with ice falls, where the ice surface is heavily crevassed and the basal topography is steep. Both tributaries, Ramp and Blackwall glaciers, are exhibiting too low simulated velocities. Along the shear margin of the main trunk between Ramp and Blackwall glaciers, we overestimate the speed. However, the overall distribution is that we tend to underestimate flow velocities in the areas of streamish flow. The Bell-lake area exhibits low magnitudes in differences, and the differences are a factor of 5-8 below the observed velocities in that region.

8.4.2 Basal Drag and Friction Coefficients

Based on the optimal parameter choices for $\gamma_1 - \gamma_3$, E , k_{ini} and k_{min} found in the sensitivity tests, we present in the following section our 'best-guess' for the basal drag and friction coefficient and aim to address the raised glaciological questions. In the following, we present α (Fig. 8.7) instead of α^2 (that would directly express the linear relationship between basal shear stress and velocity) in order to compare our results with Morlighem, Seroussi, et al. (2013). The range of α indicates areas

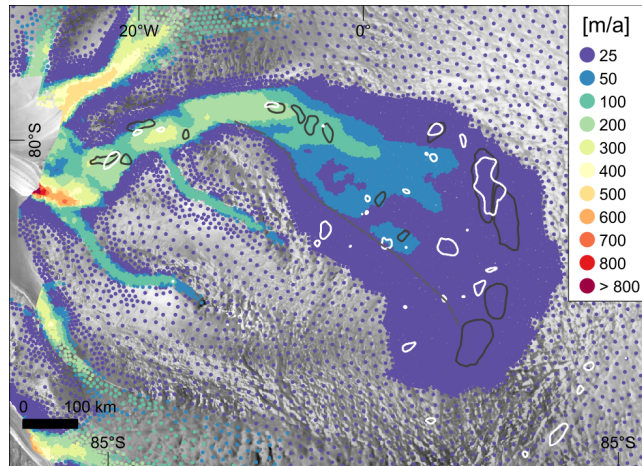


Fig. 8.5: Modelled surface velocity after inversion obtained with the optimal parameter set for γ_1 – γ_3 and $E = 0.5$. White polygons are locations of sinks updated from Humbert et al. (2018), the dark grey polygons are previously suggested lake outlines.

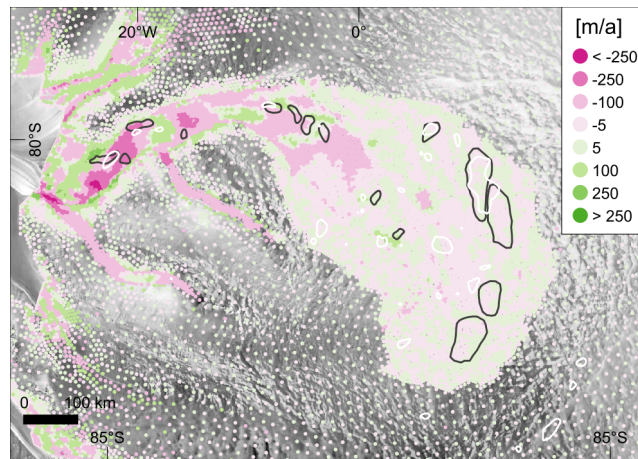


Fig. 8.6: Obtained difference in surface velocity magnitude $v_{\text{mod}} - v_{\text{obs}}$ with the optimal parameter set for γ_1 – γ_3 and $E = 0.5$. White polygons are locations of sinks updated from Humbert et al. (2018), the dark grey polygons are previously suggested lake outlines.

with particular smooth bed with very low values, whereas widespread areas in the onset area of the ice stream are marked by moderate values of $\alpha < 25 \text{ (Pa a/m)}^{1/2}$. The main trunk is intersected with several patches of very high values. Figure 8.8 is basically showing k , which is of the same type of distribution across the catchment, but is not subsuming the effective pressure N (Fig. 8.18).

Beside the distribution of α , Fig 8.7 also contains two criteria that are used to estimate potential subglacial lake locations from radio echo sounding. The data is taken from Humbert et al. (2018) and discussed there in detail. In short those criteria are searching for a change in the power of the basal reflection between inside and outside a sink, hence a potential subglacial lake. Where the change is significant,

the power criterion is full filled and shown as an orange dot. In a similar way, the peak criterion searches in sinks for high correlation of the peakiness (shape of the waveform) of the basal reflection, with high correlation meaning minor change in the type of reflection and hence similar properties of the base which is only expected with vanishing roughness that would itself represent a subglacial lake.

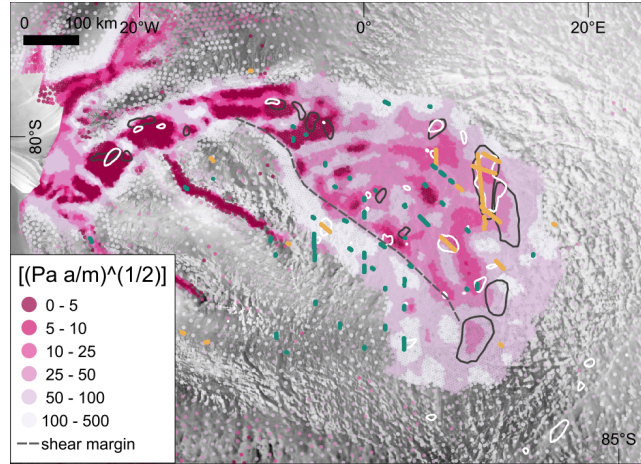


Fig. 8.7: Inferred basal friction coefficient α . The orange and green dots are representing the power and peak criteria similar to Fig. 7 in Humbert et al. (2018). White polygons are locations of sinks updated from Humbert et al. (2018), the dark grey polygons are previously suggested lake outlines. The grey dashed line represents a potential shear margin and is related to Fig. 8.13.

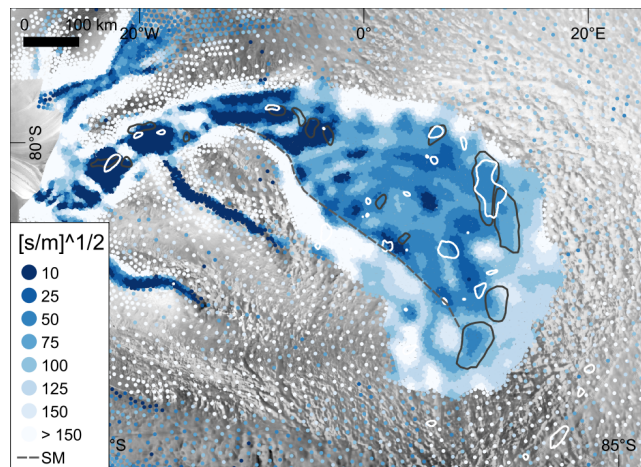


Fig. 8.8: Inferred basal drag coefficient k . White polygons are locations of sinks updated from Humbert et al. (2018), the dark grey polygons are previously suggested lake outlines. The grey dashed line represents a potential shear margin and is related to Fig. 8.13.

8.4.3 Basal drag, driving stress and basal sliding

Driving stress is estimated by assuming a shallow ice driving stress of $\tau_d = \rho_i g H \text{grad } h_s$. Figure 8.9a, displaying the driving stress τ_d , exemplifies the low surface gradient in the onset region of the ice stream leading to low τ_d in this area. Driving stress

is high where the ice is moving into that area, as well as in the main trunk. There, only small patches of low basal drag appear.

The distribution of basal drag (Fig. 8.9b) is consisting of three different regimes: the main trunk with alterations between high and low values, the onset area with a pattern of low and moderate values of τ_b and the transition between both zones. At the onset beyond the Bell-lake area the shear stress is increasing to 50-70 kPa representing the area where the transition from the steeper interior to the onset is taking place. The onset area is a mixture of very low τ_b and spots of localized high basal drag. High basal drag is often, but not always, associated with subglacial hills, low values are found in valleys but also in some instances on slopes in the basal topography. In the transition to the main trunk, the bands with increasing basal drag are located on steep flanks in the basal topography and where a ridge crossing the ice stream is located. Low values are often found in valleys and on flat terraces. At the location of R5–R8 (see Fig. 8.2) the main trunk is in flow direction divided by a zone of high basal drag. This is situated on the steep flank of a subglacial terrace that represents a step elevation change towards the Transantarctic Mountains.

The difference between basal drag and driving stress is often used to infer bed properties. Figure 8.9c is unveiling that in vast areas the driving stress is either exceeding the basal drag or vice versa and only in very limited areas both are balanced out. This is the case in the LA/LB area, although it is also patchy, and along the southern margin of the ice stream. In the onset area exist more locations with $\tau_d > \tau_b$, but due to very localized surface gradients affecting the driving stress, the distribution is rather patchy there, too. The main trunk exhibits then a clearer picture with wider areas of either τ_d or τ_b dominating. In the steep slopes of the ice falls and subglacial ridges the high basal stress is dominating, whereas the low values are found in flatter areas and valleys. This pattern is basically dominated by the magnitude of τ_b .

One of the most interesting parts in studying the dynamics of this ice stream is to look at the contribution of sliding to the flow. Figure 8.10 is presenting the basal velocity. The main trunk reaches speeds of more than 500 m a^{-1} close to the grounding line and even 500 km upstream the grounding line sliding speeds of 100 m a^{-1} are found. Across the onset (see Fig. 8.2) the sliding speed doubles. Between south and north of the grey dotted line the sliding speed is rising by a factor 3-4.

We compare the ratio between surface and basal velocities v_s/v_b . Figure 8.11 displays in dark blue color areas which are either plug flow or close to plug flow. Greenish areas are dominated by deformation. The onset area is dominated by a sliding regime with some patches of plug flow (dark blue). Upstream the Bell-lake area deformation dominates the flow field, however, there are also areas where the sliding

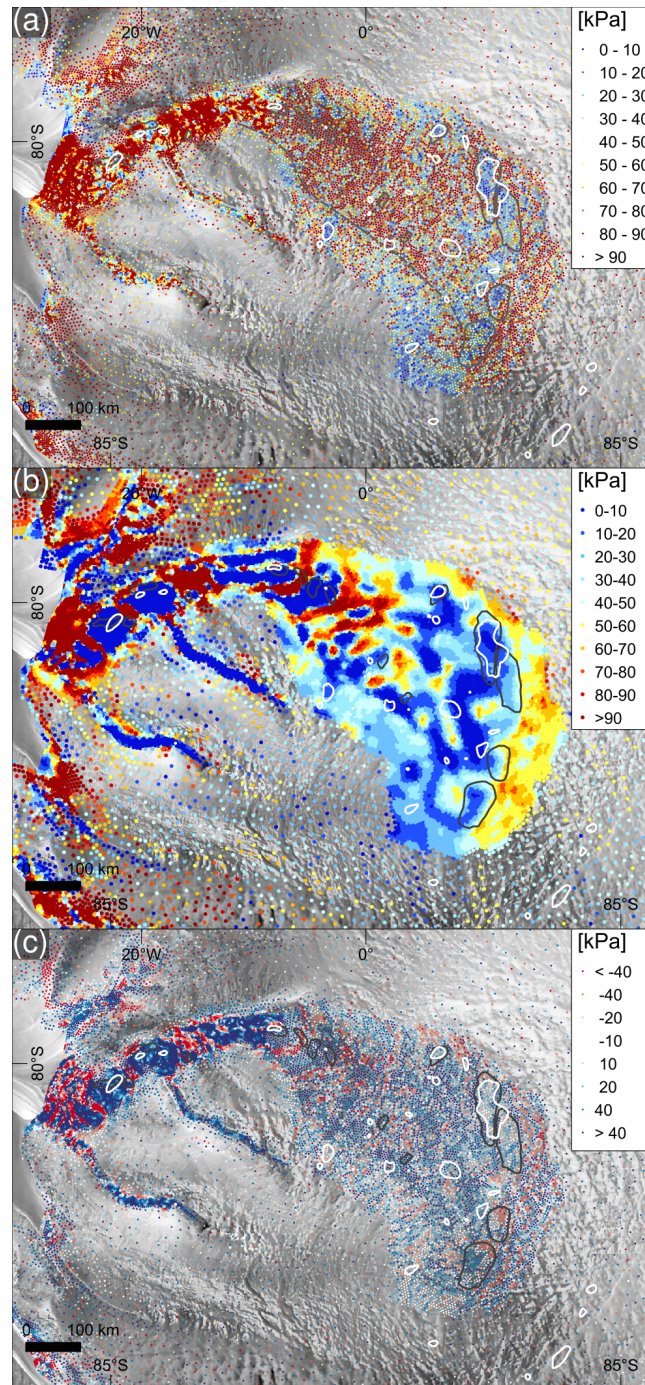


Fig. 8.9: Calculated (a) driving stress τ_d , (b) basal shear stress τ_b and (c) difference $\tau_d - \tau_b$ for the simulation with the best parameter choice. White polygons are locations of sinks updated from Humbert et al. (2018), the dark grey polygons are previously suggested lake outlines.

is prevailing. Fig. 8.11 also marks a potential shear margin (discussed more in detail below) as grey dashed line. This line is connecting several deformation dominated spots. The main trunk exhibits several zones which are dominated by deformation. These zones basically intersect the ice stream over the entire width. Two of them are

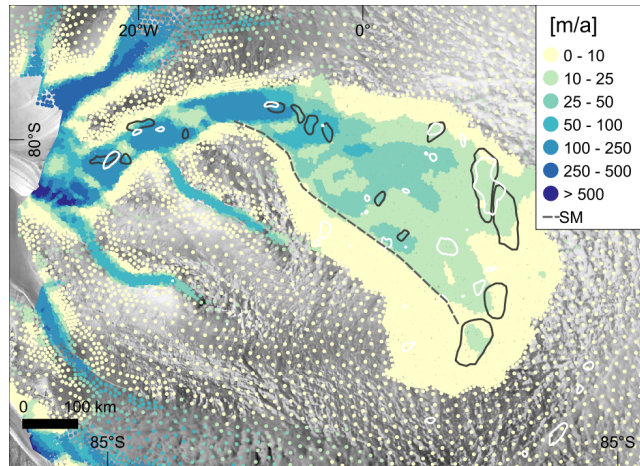


Fig. 8.10: Modelled basal velocity v_b of the simulation with the best parameter choice. White polygons are locations of sinks updated from Humbert et al. (2018), the dark grey polygons are previously suggested lake outlines. The grey dashed line represents a potential shear margin and is related to Fig. 8.13.

coincident with ice falls. The zone just upstream the grounding line is more patchy, representing also the complex basal topography in this area.

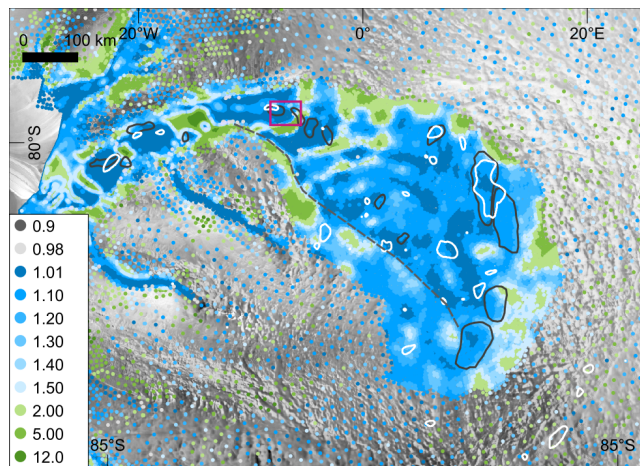


Fig. 8.11: Modelled slip ratio of surface to basal velocity, v_s/v_b for the simulation with the best parameter choice. White polygons are locations of sinks updated from Humbert et al. (2018), the dark grey polygons are previously suggested lake outlines. The grey dashed line represents a potential shear margin and is related to Fig. 8.13. The pink box outlines the region of Fig. 8.12.

8.5 Discussion

The mismatch between modelled and observed surface velocities is quite reasonable, only the main trunk shows differences that are considerably high. This is similar to other studies, which also have large differences in the fast flowing areas (Morlighem, Rignot, Seroussi, et al., 2010), but lower in magnitude. This gives us confidence in interpreting the inverted basal friction coefficient and associated values.

An updated version of sinks (S. Beyer, pers. comm., 2019) based on the new bedrock topography available is not changing the general distribution of sinks (only one is missing), but it slightly shifted and in/decreased the size of the sinks. These sinks match in the lower main trunk with areas of very low friction coefficient. Also the sink at R5 (see Fig. 8.2) is situated in a very low α . Other than those locations are not representing a match between a sink and low basal friction coefficients.

Comparing the distribution of α with the power criterion we find that the area around former LA/LB matches a sink and is also an area where low α represents low friction. This supports the findings of Humbert et al. (2018), which suggested a wet base in this area. There are also two further sinks in which the power criterion matches, however α is not very low, indicating that friction remains a contribution there.

Comparison of our v_s/v_b with Morlighem, Seroussi, et al. (2013) demonstrates that we find more variation in the ratio both in the main trunk, as well as in the onset region. In contrast to Morlighem, Seroussi, et al. (2013) the upstream area is consisting of alterations between high and low basal shear stress with areas below 20 kPa and above 90 kPa. The more complex pattern in our study is strongly attributed to new bed topography being available. An additional contribution is also the high resolution velocity data set and its preprocessing and differences in the viscosity due to different temperature fields. Similar to Morlighem, Seroussi, et al. (2013) we find upstream the former Bell-lake area bands of high basal shear stress and the magnitudes agree well. A prominent difference to Morlighem, Seroussi, et al. (2013) is that the lower parts of the tributaries of Blackwall and Ramp Glacier are subjected to high basal shear stress. The data coverage for ice thickness is limited (and was missing in 2006 entirely), however, the bedrock topography there is unlikely an artefact. All three studies represent the ice fall as an area of high basal shear stress. In contrast to Joughin, Bamber, et al. (2006) we do not find an extensive area in the lower part of the main trunk with low τ_b , but this is most likely to the missing bed topography data back then.

Analysis of the basal shear stress, k and α also needs to consider weaknesses in the modelling approach. There are two issues concerning areas of the ice falls. The higher order approximation may not hold there, as it is not excluded that bridging effects are a strong factor there. This cannot be assessed as no full Stokes simulations are available for this particular region and no comparison of higher order to full Stokes was yet successfully conducted in similar situations. The findings of Morlighem, Rignot, Seroussi, et al. (2010) exemplify a strong influence in the vicinity of the grounding line of Pine Island Glacier, which may support that full Stokes may lead to a lower basal drag and friction coefficient at the ice falls. Furthermore, the ice is heavily crevassed at the surface and hence, the viscosity would be reduced due

to the damage. This has not been taken into account. The strain-softening effect may, however, contribute to lower viscosity in the ice fall, and hence the ratio of surface to basal velocity, is representing a deformation dominated regime.

We find, similar to Morlighem, Rignot, Seroussi, et al. (2010) that the basal drag is high at steep bedrock slopes where the ice needs to flow upwards. In their comparison between full Stokes and higher order approximation based inversion, it becomes clear, that the basal drag at steep slopes is larger using higher order approximation. This is due to the missing bridging effects in the stress balance, which is balanced out in the inversion by increasing τ_b . Our simulations exhibit similar features (which we cannot compare to full Stokes) and as the Recovery Glacier main trunk is by no means a smooth deep trunk, this is likely affecting the simulations here, too.

When comparing α in this study with Morlighem, Seroussi, et al. (2013) the difference in the main trunk is most striking, as we find alterations of low and high basal friction coefficient. The transition between Slessor and Recovery glaciers near the grounding line is in both studies exhibiting a higher α , as well as a branch between both glaciers with medium values. Although our difference between observed and modelled velocities in this area is not very low, we interpret from this comparison that our results in this area are still plausible.

In order to compare the results from the inversion with structural characteristics found in high-resolution satellite remote sensing imagery for two selected locations, we were using TerraSAR-X imagery in stripmap mode that has been transformed with a bi-cubic interpolation to 12.5 m resolution. We focus on two areas, one in the area where Humbert et al. (2018) were not finding the proposed subglacial lakes R5–R8 in their airborne radar survey, another is a newly proposed signature of a shear margin in the upstream area.

Figure 8.12 displays two TerraSAR-X overpasses in 2012, which exhibit the onset of crevasse formation. The formation of crevasses is in an area in which we find a change in the basal drag coefficient k from high to low values and in combination with that a change from low to high basal velocities, indicating that the contribution of sliding is increasing. This is to some extent driven by a slope in the basal topography, as the band of low basal velocities is situated on a bedrock ridge. Up to $8^\circ W$ the crevasse field is constrained by a flow band (comparable to situations on Filchner Ice Shelf (Hulbe et al., 2010)) and west of that wing shape crack formation by shear is visible (mode-II cracks). A subglacial sink west of $9^\circ W$ is coincident with a strong and irregularly crevassed surface that also matches a transition in the basal drag coefficient.

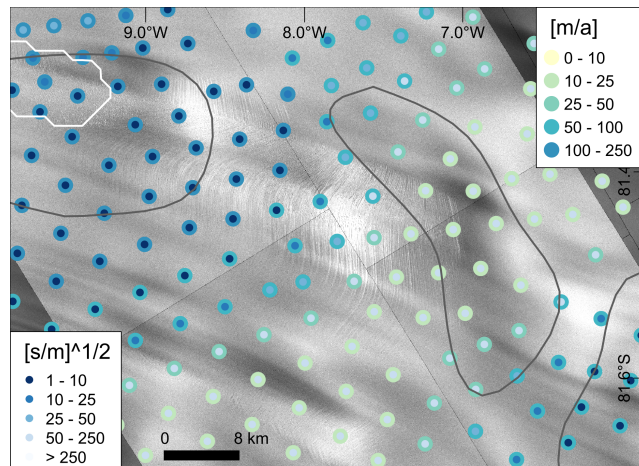


Fig. 8.12: Basal velocity v_b (large dots) and basal drag coefficient k (small dots) superimposed on TerraSAR-X stripmap mode scenes from 2012-11-27. White polygons are locations of sinks updated from Humbert et al. (2018), the dark grey polygons are previously suggested lake outlines. The grey dashed line represents a potential shear margin and is related to Fig. 8.13.

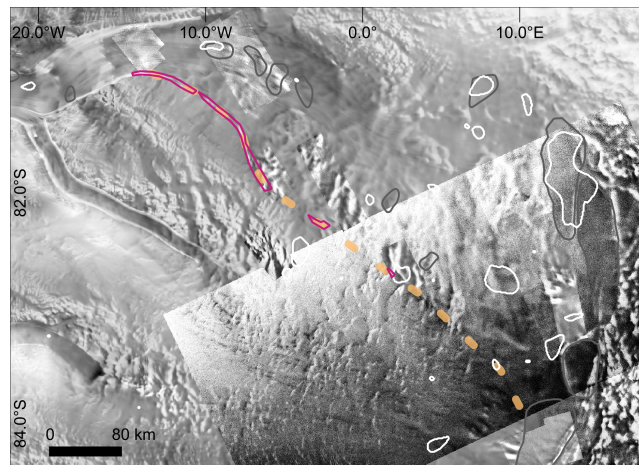


Fig. 8.13: Shear margin detected in TerraSAR-X imagery (smaller patches are in stripmap mode, large tiles are in ScansAR wide swath mode). The orange dotted line indicates the shear margin. Red lines mark crevasse areas. White and grey lines are lake polygons similar to other figures. The background imagery is the RADARSAT mosaic.

Most interesting is the match between the suggested southern shear margin and the onset of higher basal velocities. The coincidence is less prominent with the basal drag coefficient, but again high when comparing to k . As the suggestion of the location of the shear margin is completely independent from any modelling result and has in fact been first made even before the flight campaign, the surface features are seen as plausibility check of the inverted basal properties.

The inversion for k is depending on the effective normal pressure (shown in Fig. 8.18). The choice of the water pressure acting against the ice overburden pressure is thus also having a crucial effect on the inversion results. We are here relying on a widely

used assumption that locations beneath sea level are connected to the ocean and the ocean pressure to be a representative water pressure. This choice may break down wherever subglacial channels are formed or cavities are capturing water leading to pressurized system. The influence of this effect can only be simulated applying a model for subglacial hydrology (as done in Beyer et al. (2018)), which is not only beyond the scope of this study, but has also not be combined with the inversion of a basal drag coefficient so far.

The results of this study will also inform seismic campaigns, which is the ideal method to shade some light into the basal properties of the ice, as well as underlying sediment. Ideally such campaigns retrieve along flow profiles from R5-R8 upstream crossing the onset region. Given that vast parts of the main trunk are heavily crevassed preventing field campaigns, the combination of remote sensing, airborne surveys and modelling will remain the only access to information on basal properties of the main trunk in future.

8.6 Conclusions

A major difference between our study and previous inverse approaches in this area is the availability of a new ice thickness dataset. Former studies were presumably biased by bedrock topography determined from balance velocities and hence, a main trunk that is flatter and more even than the real system. Although Recovery Glacier is deeply incised into the margin of the Transantarctic Mountain range, mountain ridges across the glaciers main trunk are making this ice stream distinct from ice streams along the Siple Coast (Joughin, Bamber, et al., 2006). These ridges are associated with large basal drag and high drag and friction coefficients, which can be a consequence of bridging effects being neglected.

The onset region of Recovery Glacier is characterised by a sliding dominated flow regime with moderate values for basal friction and drag coefficient. A wet base is hence very likely, however, the base is not expected to be smooth. The basal drag in this area exhibits a complex pattern of low and moderate values with higher values found on subglacial hills.

We found a shear margin detected from TerraSAR-X imagery to match with both, the transition from deformation to sliding dominated flow regime and to the onset of lower basal friction coefficient.

Given that it is to be expected that friction is going to vanish over a lake, the distribution of both, basal drag and friction coefficient, precludes lakes at the onset

of the ice stream. This is taking the findings of Humbert et al. (2018) one step further as this approach is not relying on radar data analysis, but is an independent assessment of the existence of lakes.

8.7 Appendix

8.7.1 Effect of Preprocessing of Remote Sensing Data for Inverse Modelling

In the following figures we provide differences of velocity fields for simulations with and without filter as preprocessing of the remote sensing dataset, as well as the effect of the interpolation method.

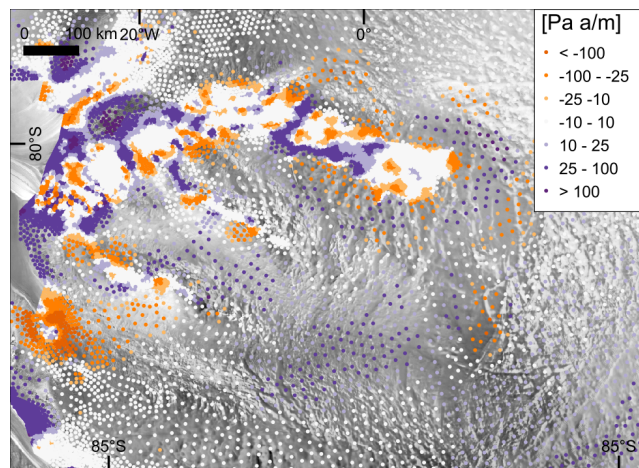


Fig. 8.14: Difference $k_{\text{filt}} - k_{\text{nofilt}}$ between applying a filter (Lüttig et al., 2017) to no filter to the remote sensing velocity fields. Both input fields are mapped onto our mesh using linear interpolation.

8.7.2 Sensitivity to Enhancement Factor and Inversion Parameters

Here we present the rms between measured and modelled surface velocities for simulations conducted with various enhancement factors and a variety of inversion parameters.

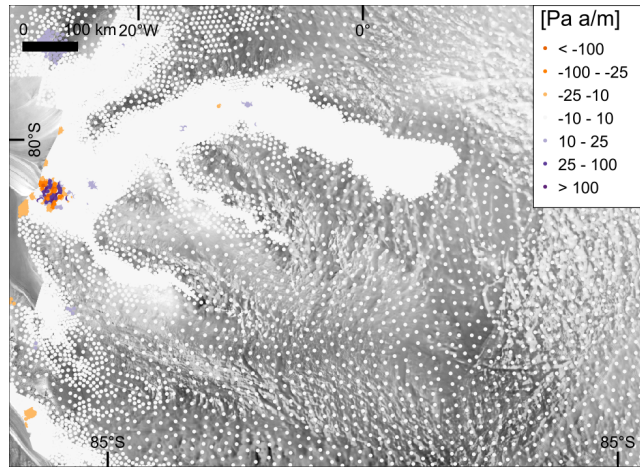


Fig. 8.15: Difference $k_{\text{linint}} - k_{\text{natint}}$ between using a linear interpolation or natural neighbour interpolation to map the filtered velocity field to finite element mesh nodes.

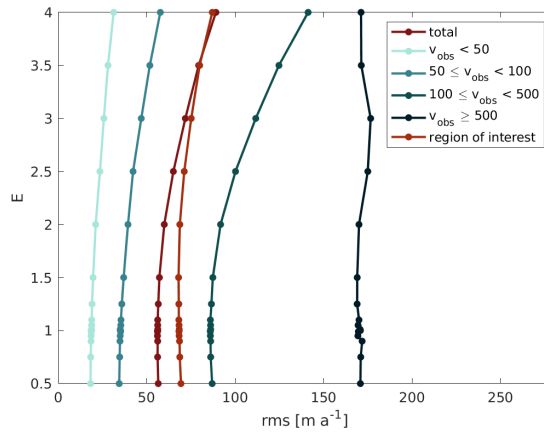


Fig. 8.16: Sensitivity of the inversion on the enhancement factor E : rms of the difference of surface velocity magnitudes for the respective parameter choice. The redish graphs show the rms of the entire data set, while blueish colored graphs indicate subsets classified according to observed surface velocities. Orange marks the region covered by the TerraSAR-X derived velocity field (Fig. 8.3).

8.7.3 Effective Normal Pressure

As the effective normal pressure is influencing the sliding law and hence the inversion for k , we present here the distribution of N , which remains unchanged for all simulations conducted in this study.

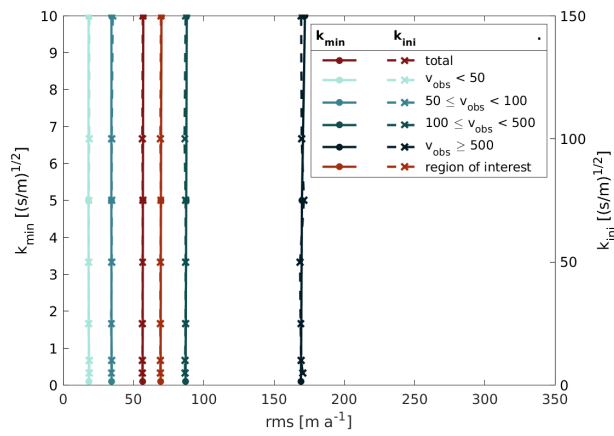


Fig. 8.17: Sensitivity of the inversion on k_{\min} (solid lines) and k_{ini} (dashed lines): rms of the difference of surface velocity magnitudes for the respective parameter choice. The redish graphs show the rms of the entire data set, while blueish colored graphs indicate subsets classified according to observed surface velocities. Orange marks the region covered by the TerraSAR-X derived velocity field (Fig. 8.3).

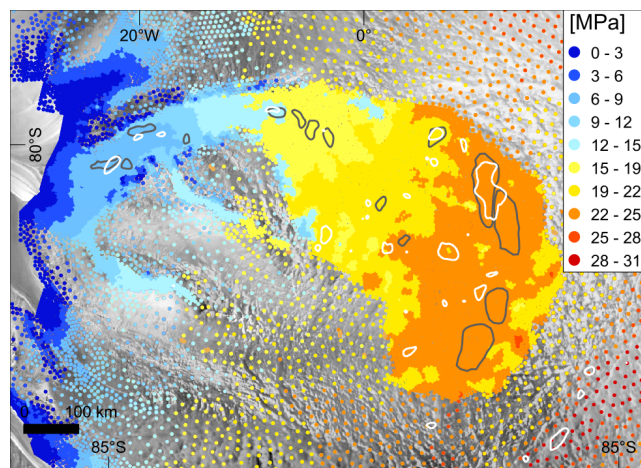


Fig. 8.18: Effective normal pressure N .

Conclusion

” *The important thing is to never stop questioning.*

— **Albert Einstein**
Physicist

9.1 Achievements

In Sect. 2.3 three objectives were formulated. This section highlights the objectives achieved in this work.

1. Deriving the spatial distribution of the basal friction coefficient in the Recovery catchment area by using an inverse method.

The equations of ice dynamics and the boundary conditions are derived in Chapter 4. This includes also the sliding law, which depends on the friction coefficient, the variable, which is the heart of this thesis. Chapter 5 introduces the theory of inverse problems and its application to ice dynamics. The model framework ISSM is used to conduct the inversion of basal friction at Recovery Glacier. For this purpose, the Higher-Order approximation of ice flow is used. ISSM applies the classical adjoint method to minimize the misfit between observed and modelled velocities on the ice surface. The misfit is measured by the weighted sum of three cost functions: linear and logarithmic misfit as well as a regularization term. The results are presented in Chapter 8 and show medium values in the onset area of Recovery Glacier. In the main trunk, basal friction alternates between very high and very low values. Altogether, the results of the study support the findings of Humbert et al. (2018) and raise doubts about the existence of subglacial lakes enhancing Recovery Glaciers flow. Furthermore, the study considers some other glaciological quantities, which can be calculated with the inversion results: driving stress, basal shear stress, and the contribution of sliding.

2. Improvement of the quality of velocity fields derived from remote sensing by application of filtering and interpolation techniques.

The two articles presented in Chapter 6 and 7 present the quality improvement of the TerraSAR-X derived velocity field presented in Sect. 3.3. A new filtering procedure combining three approaches was implemented. In a first step, smooth segments in the velocity field are detected in order to remove segments which are too small. The next step utilizes the median of a moving window to remove points with high deviations from surrounding velocities. The third filtering step removes points with large differences in flow direction. During the procedure 83 % of the data were kept while the majority of false values was removed. The remaining data points served as input for four interpolation methods: linear interpolation, natural neighbor interpolation, Kriging, and minimum curvature. The results were compared in order to determine the most suitable interpolation method for this kind of data, which turned out to be natural neighbor interpolation. Thus, the quality of the initial velocity field was strongly improved by applying these processing steps. However, some stripe features in the velocity field are still present and all interpolation procedures had difficulties filling gaps in the shear margins.

3. Conduct of a sensitivity analysis of the inversion of basal friction with regard to model parameters as well as quality of input surface velocities.

The sensitivity analysis was carried out in the article presented in Chapter 8. The influence of the enhancement factor as well as filtering of the velocities and the choice of the interpolation method were investigated. For this purpose, the inversion was performed with different velocity input fields: the original field of Recovery Glacier presented in Sect. 3.3 and the filtered velocity field, interpolated using linear and natural neighbor interpolation. Major differences can be seen in the basal friction inverted from filtered and unfiltered data due to many patterns of outliers in the unfiltered velocity field. Clear differences result also from varying the interpolation method, in particular near the grounding line and far upstream, however in the interesting onset area of Recovery Glacier the effect is minimal. The sensitivity to three other parameters was tested: the initial value of the basal friction, the minimal basal friction (lower bound), and the enhancement factor. Only for the latter an influence can be seen, showing that the inversion is very robust.

9.2 Outlook

While improving the quality of the velocity field, two steps were necessary: filtering and interpolation. Both can be further developed in order to improve the results even more. In the velocity data stripes are visible, which occur from processing the satellite images. Therefore, more work has to be done in this field of research. Better processing techniques would already prevent the origin of these features. An

alternative is an additional filtering step, which detects the stripes and removes them. In doing so, a challenge would be to decide which values are false, hill or valley of the stripe. Furthermore, such a procedure would maybe unintentionally remove too many data points.

None of the evaluated interpolation methods turned out to be perfect in the application to velocity fields. Shear margins are a problematic terrain for all of them. Techniques which are able to solve these problems have to be further developed, in particular because the choice of interpolation can have an effect on modelling results at least in specific regions. This finding should also lead to overthink the interpolation methods used in models. Although the influence of the interpolation method is not strong in the region of interest of Sect. 8, this choice may have an effect in other studies. It is advisable to utilize natural neighbor interpolation instead of linear interpolation as standard for interpolating velocities or at least to examine the effect of this change.

It would be reasonable to also inspect the influence of the interpolation of other variables, such as ice thickness or surface elevation. Especially when inverting for the ice viscosity parameter B minimizing observation mismatches of ice thickness, improper interpolation can lead to errors, which could be avoided.

To measure the influence of the different inverted basal frictions on quantities like sea level contribution, further simulations have to be carried out. For this purpose, basal friction would serve as input for transient runs using e.g. ISSM. Due to the strong differences obtained from the velocities with varying quality, strong differences in future evolution of Recovery Glacier may be expected.

To ensure smaller errors in the initial states of flow models, more studies like this have to be conducted. The results would improve the knowledge of the effect of errors in the input data and lead to better error estimates of model results.

Bibliography

- Abdel Jaber, W. (2016). „Derivation of mass balance and surface velocity of glaciers by means of high resolution synthetic aperture radar: application to the Patagonian Icefields and Antarctica“. PhD thesis. DLR-Forschungsbericht. 2016-54, 236 S (cit. on pp. 10, 41).
- Amidror, I. (2002). „Scattered data interpolation methods for electronic imaging systems: a survey.“ In: *J. Electronic Imaging* 11.2, pp. 157–176 (cit. on pp. 65, 68, 70).
- Arthern, R. J. and G. H. Gudmundsson (2010). „Initialization of ice-sheet forecasts viewed as an inverse Robin problem“. In: *Journal of Glaciology* 56.197, pp. 527–533 (cit. on pp. 21, 31).
- Balay, S. et al. (2018). *PETSc Web page*. <http://www.mcs.anl.gov/petsc> (cit. on p. 30).
- Bamber, J.L. (2007). „Remote Sensing in Glaciology“. In: *Glacier Science and Environmental Change*. John Wiley & Sons, Ltd. Chap. 73, pp. 370–382 (cit. on pp. 8, 9).
- Bamber, J.L., R.B. Alley, and I. Joughin (2007). „Rapid response of modern day ice sheets to external forcing“. In: *Earth and Planetary Science Letters* 257.1, pp. 1–13 (cit. on p. 1).
- Bell, R. E., M. Studinger, C. A. Shuman, M. A. Fahnestock, and I. Joughin (2007). „Large subglacial lakes in East Antarctica at the onset of fast-flowing ice streams“. In: *Nature* 445, pp. 904–907 (cit. on pp. 4, 5, 87).
- Beyer, S., T. Kleiner, V. Aizinger, M. Rückamp, and A. Humbert (2018). „A confined–unconfined aquifer model for subglacial hydrology and its application to the Northeast Greenland Ice Stream“. In: *The Cryosphere* 12.12, pp. 3931–3947 (cit. on p. 107).
- Blatter, H. (1995). „Velocity and stress fields in grounded glaciers: a simple algorithm for including deviatoric stress gradients“. In: *Journal of Glaciology* 41.138, pp. 333–344 (cit. on pp. 19, 91, 94).
- Bolch, T., B. Menounos, and R. Wheate (2010). „Landsat-based inventory of glaciers in western Canada, 1985-2005“. In: *Remote Sensing of Environment* 114.1, pp. 127–137 (cit. on p. 9).
- Bonan, B., M. Nodet, C. Ritz, and V. Peyaud (2014). „An ETKF approach for initial state and parameter estimation in ice sheet modelling“. In: *Nonlinear Processes in Geophysics* 21.2, pp. 569–582 (cit. on p. 32).
- Brent, R. P. (1971). „An algorithm with guaranteed convergence for finding a zero of a function“. In: *The Computer Journal* 14.4, pp. 422–425 (cit. on p. 26).

- Brondex, J., F. Gillet-Chaulet, and O. Gagliardini (2019). „Sensitivity of centennial mass loss projections of the Amundsen basin to the friction law“. In: *The Cryosphere* 13.1, pp. 177–195 (cit. on p. 89).
- Bueler, E. and J. Brown (2009). „Shallow shelf approximation as a "sliding law" in a thermomechanically coupled ice sheet model“. In: *Journal of Geophysical Research* 114.F3, F03008 (cit. on p. 94).
- Burgess, E. W., R. R. Forster, C. F. Larsen, and M. Braun (2012). „Surge dynamics on Bering Glacier, Alaska, in 2008-2011“. In: *The Cryosphere* 6.6, pp. 1251–1262 (cit. on pp. 54, 55).
- Campbell, J.B. and R.H. Wynne (2011). *Introduction to Remote Sensing, Fifth Edition*. Guilford Publications (cit. on p. 8).
- Chandler, D. M., A. L. Hubbard, B. P. Hubbard, and P. W. Nienow (2006). „A Monte Carlo error analysis for basal sliding velocity calculations“. In: *Journal of Geophysical Research: Earth Surface* 111.F4 (cit. on p. 32).
- Cressie, N. (1990). „The origins of kriging“. In: *Mathematical Geology* 22.3, pp. 239–252 (cit. on p. 65).
- Cuffey, K.M. and W.S.B. Paterson (2010). *The Physics of Glaciers*. Elsevier Science (cit. on pp. 8, 9, 13, 15, 17, 18, 92).
- Darelius, E., I. Fer, and K. W. Nicholls (2016). „Observed vulnerability of Filchner-Ronne Ice Shelf to wind-driven inflow of warm deep water“. In: *Nature Communications* 7. Article, p. 12300 (cit. on p. 2).
- DeConto, R. M. and D. Pollard (2016). „Contribution of Antarctica to past and future sea-level rise“. In: *Nature* 531. Article, pp. 591–597 (cit. on p. 2).
- Diez, A., K. Matsuoka, F. Ferraccioli, T. A. Jordan, H. F. Corr, J. Kohler, A. V. Olesen, and R. Forsberg (2018). „Basal Settings Control Fast Ice Flow in the Recovery/Slessor/Bailey Region, East Antarctica“. In: *Geophysical Research Letters* 45.6, pp. 2706–2715 (cit. on p. 6).
- Eis, C. and A. Humbert (submitted, 2019). „An evaluation of gap filling methods for glacier surface velocity fields derived by remote sensing“. In: *Journal of Glaciology* * (cit. on pp. 88, 97).
- Fahnestock, M., T. Scambos, T. Moon, A. Gardner, T. Haran, and M. Klinger (2015). „Rapid large-area mapping of ice flow using Landsat 8“. In: *Remote Sensing of Environment* (cit. on pp. 36, 63).
- Faria, S.H., S. Kipfstuhl, and A. Lambrecht (2018). *The EPICA-DML Deep Ice Core, A Visual Record*. Springer, Berlin, Heidelberg (cit. on p. 1).
- Ferraccioli, F. et al. (2018). *Bed, surface elevation and ice thickness measurements derived from Radar acquired during the ICEGRAV-2013 airborne geophysics campaign* (cit. on p. 94).
- Floricioiu, D., W. Abdel Jaber, and K.C. Jezek (2014). „TerraSAR-X and TanDEM-X observations of the Recovery Glacier system, Antarctica“. In: *Proceedings of IGARSS 2014 IEEE Xplore*. IGARSS 2014, Quebec, City, QC, Canada, pp. 4852–4855 (cit. on pp. 5, 10, 41, 66, 88, 94, 97).
- Fogwill, C.J., M.J. Bentley, D.E. Sugden, A.R. Kerr, and P.W. Kubik (2004). „Cosmogenic nuclides ^{10}Be and ^{26}Al imply limited Antarctic Ice Sheet thickening and low erosion in the Shackleton Range for >1 m.y.“ In: *Geology* 32.3, p. 265 (cit. on p. 4).

- Forsberg, R., A. V. Olesen, F. Ferraccioli, T. A. Jordan, K. Matsuoka, A. Zakrajsek, M. Ghidella, and J. S. Greenbaum (2018). „Exploring the Recovery Lakes region and interior Dronning Maud Land, East Antarctica, with airborne gravity, magnetic and radar measurements“. In: *Geological Society, London, Special Publications* 461.1, pp. 23–34 (cit. on pp. 6, 89, 94).
- Fretwell, P. et al. (2013a). „Bedmap2: improved ice bed, surface and thickness datasets for Antarctica“. In: *The Cryosphere* 7.1, pp. 375–393 (cit. on pp. 1, 2).
- (2013b). „Bedmap2: improved ice bed, surface and thickness datasets for Antarctica“. In: *The Cryosphere* 7.1, pp. 375–393 (cit. on p. 94).
- Fricker, H. A., S. P. Carter, R. E. Bell, and T. Scambos (2014). „Active lakes of Recovery Ice Stream, East Antarctica: a bedrock-controlled subglacial hydrological system“. In: *Journal of Glaciology* 60.223, pp. 1015–1030 (cit. on pp. 6, 87).
- Furrer, R., M.G. Genton, and D. Nychka (2006). „Covariance Tapering for Interpolation of Large Spatial Datasets“. In: *Journal of Computational and Graphical Statistics* 15.3, pp. 502–523 (cit. on p. 65).
- Gagliardini, O. et al. (2013). „Capabilities and performance of Elmer/Ice, a new-generation ice sheet model“. In: *Geoscientific Model Development* 6.4, pp. 1299–1318 (cit. on p. 17).
- Gilbert, J. C. and C. Lemaréchal (1989). „Some numerical experiments with variable-storage quasi-Newton algorithms“. In: *Mathematical Programming* 45.1, pp. 407–435 (cit. on pp. 30, 93).
- Gillet-Chaulet, F., O. Gagliardini, H. Seddik, M. Nodet, G. Durand, C. Ritz, T. Zwinger, R. Greve, and D. G. Vaughan (2012). „Greenland ice sheet contribution to sea-level rise from a new-generation ice-sheet model“. In: *The Cryosphere* 6.6, pp. 1561–1576 (cit. on p. 31).
- Glen, J.W. (1953). „Rate of Flow of Polycrystalline Ice“. In: *Nature* 172.4381, pp. 721–722 (cit. on p. 17).
- Glen, J.W. and M.F. Perutz (1955). „The creep of polycrystalline ice“. In: *Proceedings of the Royal Society of London. Series A. Mathematical and Physical Sciences* 228.1175, pp. 519–538 (cit. on p. 17).
- Goelzer, H. et al. (2018). „Design and results of the ice sheet model initialisation experiments initMIP-Greenland: an ISMIP6 intercomparison“. In: *The Cryosphere* 12.4, pp. 1433–1460 (cit. on pp. 32, 89).
- Goldberg, D. N. and O. V. Sergienko (2011). „Data assimilation using a hybrid ice flow model“. In: *The Cryosphere* 5.2, pp. 315–327 (cit. on p. 31).
- Golledge, N. R., R. H. Levy, R. M. McKay, and T. R. Naish (2017). „East Antarctic ice sheet most vulnerable to Weddell Sea warming“. In: *Geophysical Research Letters* 44.5, pp. 2343–2351 (cit. on pp. 6, 87).
- Gray, A. L., K. E. Mattar, and G. Sofko (2000). „Influence of ionospheric electron density fluctuations on satellite radar interferometry“. In: *Geophysical Research Letters* 27.10, pp. 1451–1454 (cit. on p. 36).

- Gray, A. L., K. E. Mattar, P. W. Vachon, R. Bindshadler, K. C. Jezek, R. Forster, and J. P. Crawford (1998). „InSAR results from the RADARSAT Antarctic Mapping Mission data: estimation of glacier motion using a simple registration procedure“. In: *IGARSS '98. Sensing and Managing the Environment. 1998 IEEE International Geoscience and Remote Sensing. Symposium Proceedings. (Cat. No.98CH36174)*. Vol. 3, 1638–1640 vol.3 (cit. on p. 10).
- Greve, R. and H. Blatter (2009). *Dynamics of Ice Sheets and Glaciers*. Springer-Verlag Berlin Heidelberg (cit. on pp. 13, 19).
- Gudmundsson, G. H. and M. J. Raymond (2008). „On the limit to resolution and information on basal properties obtainable from surface data on ice streams“. In: *The Cryosphere* 2.2, pp. 167–178 (cit. on p. 32).
- Gupta, R.P. (2003). *Remote Sensing Geology*. Springer Berlin Heidelberg (cit. on p. 10).
- Habermann, M., D. Maxwell, and M. Truffer (2012). „Reconstruction of basal properties in ice sheets using iterative inverse methods“. In: *Journal of Glaciology* 58.210, pp. 795–808 (cit. on p. 31).
- Hadamard, J. (1902). „Sur les Problèmes aux Dérivées Partielles et Leur Signification Physique“. In: *Princeton University Bulletin* 13, pp. 49–52 (cit. on p. 22).
- Hansen, P.C. (2001). „The L-Curve and its Use in the Numerical Treatment of Inverse Problems“. English. In: *Computational Inverse Problems in Electrocardiology*. Ed. by P. Johnston. WIT Press, pp. 119–142 (cit. on p. 30).
- Heid, T. and A. Kääb (2012a). „Evaluation of existing image matching methods for deriving glacier surface displacements globally from optical satellite imagery“. In: *Remote Sensing of Environment* 118, pp. 339–355 (cit. on p. 55).
- (2012b). „Repeat optical satellite images reveal widespread and long term decrease in land-terminating glacier speeds“. In: *The Cryosphere* 6.2, pp. 467–478 (cit. on p. 9).
- Hellmer, H.H., F. Kauker, R. Timmermann, J. Determann, and J. Rae (2012). „Twenty-first-century warming of a large Antarctic ice-shelf cavity by a redirected coastal current“. In: *Nature* 485, pp. 225–228 (cit. on p. 6).
- Hindmarsh, R. C. A. (2004). „A numerical comparison of approximations to the Stokes equations used in ice sheet and glacier modeling“. In: *Journal of Geophysical Research: Earth Surface* 109.F1 (cit. on p. 91).
- Hooke, R.L.B. (2005). *Principles of Glacier Mechanics*. Principles of Glacier Mechanics. Cambridge University Press (cit. on pp. 16, 17).
- Hulbe, Christina L., Christine LeDoux, and Kenneth Cruikshank (2010). „Propagation of long fractures in the Ronne Ice Shelf, Antarctica, investigated using a numerical model of fracture propagation“. In: *Journal of Glaciology* 56.197, pp. 459–472 (cit. on p. 105).
- Humbert, A., D. Steinhage, V. Helm, S. Beyer, and T. Kleiner (2018). „Missing Evidence of Widespread Subglacial Lakes at Recovery Glacier, Antarctica“. In: *Journal of Geophysical Research: Earth Surface* (cit. on pp. 6, 88–90, 94, 99, 100, 102–106, 108, 111).
- Hutter, K. (1983). *Theoretical glaciology : material science of ice and the mechanics of glaciers and ice sheets*. Dordrecht ; Boston : Reidel ; Tokyo, Japan : Terra Scientific Pub. Co. ; Hingham, MA : Sold, distributed in the U.S.A., and Canada by Kluwer Academic Publishers (cit. on pp. 13, 16).

- IPCC (2014). *Climate Change 2014: Synthesis Report. Contribution of Working Groups I, II and III to the Fifth Assessment Report of the Intergovernmental Panel on Climate Change*. 151 pp. IPCC, Geneva, Switzerland: Core Writing Team, Pachauri, R.K., and Meyer, L.A. (eds.) (cit. on p. 1).
- Jay-Allemand, M., F. Gillet-Chaulet, O. Gagliardini, and M. Nodet (2011). „Investigating changes in basal conditions of Variegated Glacier prior to and during its 1982-1983 surge“. In: *The Cryosphere* 5.3, pp. 659–672 (cit. on p. 31).
- Jezek, K.C. (1999). „Glaciological properties of the Antarctic ice sheet from RADARSAT-1 synthetic aperture radar imagery“. In: *Annals of Glaciology* 29, pp. 286–290 (cit. on pp. 4, 5, 87, 88).
- Jezek, K.C., D. Floricioiu, K. Farness, N. Yague-Martinez, and M. Eineder (2009). „TerraSAR-X observations of the recovery glacier system, Antarctica“. In: *IEEE International Geoscience and Remote Sensing Symposium*. Vol. 2, pp. 226–229 (cit. on pp. 5, 56).
- Jezek, K.C., H.G. Sohn, and K.F. Noltimier (1998). „The RADARSAT Antarctic Mapping Project“. In: *IGARSS '98. Sensing and Managing the Environment. 1998 IEEE International Geoscience and Remote Sensing. Symposium Proceedings. (Cat. No.98CH36174)*. Vol. 5, pp. 2462–2464 (cit. on p. 4).
- Joughin, I. (2002). „Ice-sheet velocity mapping: a combined interferometric and speckle-tracking approach“. In: *Annals of Glaciology* 34, pp. 195–201 (cit. on p. 9).
- Joughin, I., J.L. Bamber, T. Scambos, S. Tulaczyk, M. Fahnestock, and D.R. MacAyeal (2006). „Integrating satellite observations with modelling: basal shear stress of the Filcher-Ronne ice streams, Antarctica“. In: *Philosophical Transactions of the Royal Society A: Mathematical, Physical and Engineering Sciences* 364.1844, pp. 1795–1814 (cit. on pp. 89, 104, 107).
- Joughin, I., D. R. MacAyeal, and S. Tulaczyk (2004). „Basal shear stress of the Ross ice streams from control method inversions“. In: *Journal of Geophysical Research: Solid Earth* 109.B9 (cit. on pp. 31, 89).
- Joughin, I., B.E. Smith, I. Howat, and T. Scambos (2016). *MEaSUREs Multi-year Greenland Ice Sheet Velocity Mosaic, Version 1. Boulder, Colorado USA. NASA National Snow and Ice Data Center Distributed Active Archive Center*. (Cit. on p. 49).
- Joughin, I., B.E. Smith, I. Howat, T. Scambos, and T. Moon (2010). „Greenland flow variability from ice-sheet-wide velocity mapping“. In: *Journal of Glaciology* 56.197, pp. 415–430 (cit. on pp. 9, 35, 36, 50, 63).
- Kääb, A., S. Winsvold, B. Altena, C. Nuth, T. Nagler, and J. Wuite (2016). „Glacier Remote Sensing Using Sentinel-2. Part I: Radiometric and Geometric Performance, and Application to Ice Velocity“. In: *Remote Sensing* 8.7, p. 598 (cit. on pp. 36, 63).
- Kamb, B. (2001). „Basal Zone of the West Antarctic Ice Streams and its Role in Lubrication of Their Rapid Motion“. In: *The West Antarctic Ice Sheet: Behavior and Environment*. American Geophysical Union (AGU), pp. 157–199 (cit. on p. 89).
- Karush, W. (1939). „Minima of Functions of Several Variables with Inequalities as Side Constraints“. MA thesis. University of Chicago, Department of Mathematics (cit. on p. 24).
- King, J. C. and J. Turner (1997). *Antarctic Meteorology and Climatology*. Cambridge Atmospheric and Space Science Series. Cambridge University Press (cit. on pp. 1, 2).

- Kuhn, H. W. and A. W. Tucker (1951). „Nonlinear Programming“. In: *Proceedings of the Second Berkeley Symposium on Mathematical Statistics and Probability*. Berkeley, Calif.: University of California Press, pp. 481–492 (cit. on p. 24).
- Langley, K., J. Kohler, K. Matsuoka, A. Sinisalo, T. Scambos, T. Neumann, A. Muto, J.-G. Winther, and M. Albert (2011). „Recovery Lakes, East Antarctica: Radar assessment of sub-glacial water extent“. In: *Geophysical Research Letters* 38.5 (cit. on p. 6).
- Larour, E., H. Seroussi, M. Morlighem, and E. Rignot (2012). „Continental scale, high order, high spatial resolution, ice sheet modeling using the Ice Sheet System Model (ISSM)“. In: *Journal of Geophysical Research: Earth Surface* 117.F1 (cit. on pp. 20, 31, 94, 95).
- Le Brocq, A. M., A. Hubbard, M. J. Bentley, and J.L. Bamber (2008). „Subglacial topography inferred from ice surface terrain analysis reveals a large un-surveyed basin below sea level in East Antarctica“. In: *Geophysical Research Letters* 35.16 (cit. on p. 5).
- Leuschen, C., P. Gogineni, F. Rodriguez-Morales, J. Paden, and C. Allen (2010, updated 2017). *IceBridge MCoRDS L2 Ice Thickness (Antarctica 2011/12, 2012/13)*. Tech. rep. Boulder, Colorado USA: NASA National Snow and Ice Data Center Distributed Active Archive Center (cit. on pp. 89, 94).
- Lister, H. and G. Pratt (1959). „Geophysical Investigations of the Commonwealth Trans-Antarctic Expedition“. In: *The Geographical Journal* 125.3/4, pp. 343–354 (cit. on p. 5).
- Liu, I.-S. (2002). *Continuum Mechanics*. Springer-Verlag Berlin Heidelberg (cit. on p. 13).
- Lubin, D. and R. Massom (2006). *Polar remote sensing*. English. Springer Berlin ; London, p. 2 v. (Cit. on pp. 8, 9).
- Lüttig, C., N. Neckel, and A. Humbert (2017). „A Combined Approach for Filtering Ice Surface Velocity Fields Derived from Remote Sensing Methods“. In: *Remote Sensing* 9.10 (cit. on pp. 66, 88, 94, 108).
- MacAyeal, D. R. (1992). „The basal stress distribution of Ice Stream E, Antarctica, inferred by control methods“. In: *Journal of Geophysical Research: Solid Earth* 97.B1, pp. 595–603 (cit. on p. 31).
- (1993). „A tutorial on the use of control methods in ice-sheet modeling“. In: *Journal of Glaciology* 39.131, pp. 91–98 (cit. on pp. 28, 31).
- MacAyeal, D. R., R. A. Bindschadler, and T. A. Scambos (1995). „Basal friction of Ice Stream E, West Antarctica“. In: *Journal of Glaciology* 41.138, pp. 247–262 (cit. on p. 89).
- McNabb, R.W. et al. (2012). „Using surface velocities to calculate ice thickness and bed topography: a case study at Columbia Glacier, Alaska, USA“. In: *Journal of Glaciology* 58.212, pp. 1151–1164 (cit. on p. 54).
- Michel, R. and E. Rignot (1999). „Flow of Glaciar Moreno, Argentina, from repeat-pass Shuttle Imaging Radar images: comparison of the phase correlation method with radar interferometry“. In: *Journal of Glaciology* 45.149, pp. 93–100 (cit. on p. 10).
- Morlighem, M. (2011). „Ice sheet properties inferred by combining numerical modeling and remote sensing data“. Theses. Ecole Centrale Paris (cit. on pp. 26, 28, 29).
- Morlighem, M., E. Rignot, H. Seroussi, E. Larour, H. Ben Dhia, and D. Aubry (2010). „Spatial patterns of basal drag inferred using control methods from a full-Stokes and simpler models for Pine Island Glacier, West Antarctica“. In: *Geophysical Research Letters* 37.14 (cit. on pp. 31, 89, 103–105).

- Morlighem, M., H. Seroussi, E. Larour, and E. Rignot (2013). „Inversion of basal friction in Antarctica using exact and incomplete adjoints of a higher-order model“. In: *Journal of Geophysical Research: Earth Surface* 118.3, pp. 1746–1753 (cit. on pp. 92, 93, 98, 104, 105).
- Morlighem, M., E. Rignot, J. Mouginot, H. Seroussi, and E. Larour (2014). „Deeply incised submarine glacial valleys beneath the Greenland ice sheet“. In: *Nature Geosci* 7.6, pp. 418–422 (cit. on p. 48).
- (2015). *IceBridge BedMachine Greenland, Version 2. Boulder, Colorado USA: NASA DAAC at the National Snow and Ice Data Center*. (Cit. on p. 48).
- Mouginot, J., E. Rignot, B. Scheuchl, and R. Millan (2017). „Comprehensive Annual Ice Sheet Velocity Mapping Using Landsat-8, Sentinel-1, and RADARSAT-2 Data“. In: *Remote Sensing* 9.4, p. 20 (cit. on pp. 36, 63).
- Mouginot, J., B. Scheuchl, and E. Rignot (2012). „Mapping of Ice Motion in Antarctica Using Synthetic-Aperture Radar Data“. In: *Remote Sensing* 4.9, pp. 2753–2767 (cit. on pp. 54, 64).
- Nagler, T., H. Rott, M. Hetzenecker, J. Wuite, and P. Potin (2015). „The Sentinel-1 Mission: New Opportunities for Ice Sheet Observations“. In: *Remote Sensing* 7.7, pp. 9371–9389 (cit. on pp. 36, 50, 54, 56, 63).
- Neckel, N., D. Loibl, and M. Rankl (2017). „Recent slowdown and thinning of debris-covered glaciers in south-eastern Tibet“. In: *Earth and Planetary Science Letters* 464, pp. 95–102 (cit. on p. 55).
- Nogueira, J., A. Lecuona, and P. A. P A Rodríguez (1997). „Data validation, false vectors correction and derived magnitudes calculation on PIV data“. In: *Measurement Science and Technology* 8.12, p. 1493 (cit. on p. 65).
- Nye, J.F. and M.F. Perutz (1957). „The distribution of stress and velocity in glaciers and ice-sheets“. In: *Proceedings of the Royal Society of London. Series A. Mathematical and Physical Sciences* 239.1216, pp. 113–133 (cit. on p. 17).
- Oerlemans, J. (2001). *Glaciers and Climate Change*. Taylor & Francis (cit. on p. 1).
- Parish, T.R. and D.H. Bromwich (1987). „The surface windfield over the Antarctic ice sheets“. In: *Nature* 328, pp. 51–54 (cit. on p. 1).
- Pattyn, F. (2003). „A new three-dimensional higher-order thermomechanical ice sheet model: Basic sensitivity, ice stream development, and ice flow across subglacial lakes“. In: *Journal of Geophysical Research: Solid Earth* 108.B8 (cit. on pp. 19, 91, 94).
- Pebesma, Edzer J. (2004). „Multivariable geostatistics in S: the gstat package“. In: *Computers & Geosciences* 30, pp. 683–691 (cit. on p. 73).
- Petrat, N., H. Zhu, G. Stadler, T. J.R. Hughes, and O. Ghattas (2012). „An inexact Gauss-Newton method for inversion of basal sliding and rheology parameters in a nonlinear Stokes ice sheet model“. In: *Journal of Glaciology* 58.211, pp. 889–903 (cit. on p. 31).
- Pfeffer, W. T. et al. (2014). „The Randolph Glacier Inventory: a globally complete inventory of glaciers“. In: *Journal of Glaciology* 60.221, pp. 537–552 (cit. on p. 9).
- Pollard, D. and R. M. DeConto (2012). „A simple inverse method for the distribution of basal sliding coefficients under ice sheets, applied to Antarctica“. In: *The Cryosphere* 6.5, pp. 953–971 (cit. on p. 32).

- Pritchard, H. (2005). „Glacier surge dynamics of Sortebræ, east Greenland, from synthetic aperture radar feature tracking“. In: *Journal of Geophysical Research* 110.F3, p. 13 (cit. on p. 56).
- R Core Team (2017). *R: A Language and Environment for Statistical Computing*. R Foundation for Statistical Computing. Vienna, Austria (cit. on p. 73).
- Rankl, M., C. Kienholz, and M. Braun (2014). „Glacier changes in the Karakoram region mapped by multimission satellite imagery“. In: *The Cryosphere* 8.3, pp. 977–989 (cit. on p. 51).
- Raymond, M. J. and G. H. Gudmundsson (2009). „Estimating basal properties of ice streams from surface measurements: a non-linear Bayesian inverse approach applied to synthetic data“. In: *The Cryosphere* 3.2, pp. 265–278 (cit. on p. 32).
- Rignot, E. (2006). „Changes in ice dynamics and mass balance of the Antarctic ice sheet“. In: *Philosophical Transactions of the Royal Society of London A: Mathematical, Physical and Engineering Sciences* 364.1844, pp. 1637–1655 (cit. on p. 63).
- Rignot, E., J.L. Bamber, M.R. van den Broeke, C. Davis, Y. Li, and E. van de Berg W.J. and van Meijgaard (2008). „Recent Antarctic ice mass loss from radar interferometry and regional climate modelling“. In: *Nature Geoscience* 1, pp. 106–110 (cit. on pp. 4, 87).
- Rignot, E., J. Mouginot, and B. Scheuchl (2011a). „Antarctic grounding line mapping from differential satellite radar interferometry“. In: *Geophysical Research Letters* 38.10 (cit. on p. 94).
- (2011b). „Ice Flow of the Antarctic Ice Sheet“. In: *Science* 333.6048, pp. 1427–1430 (cit. on pp. 10, 41, 68, 88, 94, 97).
- (2011c). *MEaSURES InSAR-Based Antarctica Ice Velocity Map*. Boulder, Colorado USA: NASA DAAC at the National Snow and Ice Data Center. doi:10.5067/MEASURES/CRYOSPHERE/nsidc-0484.001 (cit. on pp. 10, 41, 68).
- (2017). *MEaSURES InSAR-Based Antarctica Ice Velocity Map, Version 2*. Boulder, Colorado USA. NASA National Snow and Ice Data Center Distributed Active Archive Center. doi: <https://doi.org/10.5067/D7GK8F5J8M8R>. (Cit. on p. 5).
- Rintoul, S.R., A. Silvano, B. Pena-Molino, E. van Wijk, M. Rosenberg, J.S. Greenbaum, and D.D. Blankenship (2016). „Ocean heat drives rapid basal melt of the Totten Ice Shelf“. In: *Science Advances* 2.12 (cit. on p. 2).
- Rosenau, R., M. Scheinert, and R. Dietrich (2015). „A processing system to monitor Greenland outlet glacier velocity variations at decadal and seasonal time scales utilizing the Landsat imagery“. In: *Remote Sensing of Environment* (cit. on pp. 37, 53, 54).
- Rückamp, M., U. Falk, K. Frieler, S. Lange, and A. Humbert (2018). „The effect of overshooting 1.5 °C global warming on the mass loss of the Greenland ice sheet“. In: *Earth System Dynamics* 9.4, pp. 1169–1189 (cit. on pp. 32, 89).
- Scherler, D., S. Leprince, and M. R. Strecker (2008). „Glacier-surface velocities in alpine terrain from optical satellite imagery-Accuracy improvement and quality assessment“. In: *Remote Sensing of Environment* 112.10, pp. 3806–3819 (cit. on pp. 54, 55).
- Schwerdtfeger, W. (1984). *Weather and climate of the Antarctic*. Amsterdam ; New York : Elsevier : Distributors for the U.S. and Canada, Elsevier Science Pub. Co (cit. on p. 2).

- Seehaus, T., S. Marinsek, V. Helm, P. Skvarca, and M. Braun (2015). *Changes in ice dynamics, elevation and mass discharge of Dinsmoor-Bombardier-Edgeworth glacier system, Antarctic Peninsula*. Supplemental material to manuscript (cit. on pp. 37, 38, 51, 54).
- Shapiro, N. M. and M. H. Ritzwoller (2004). „Inferring surface heat flux distributions guided by a global seismic model: Particular application to Antarctica“. In: *Earth and Planetary Science Letters* 223, pp. 213–224 (cit. on p. 94).
- Shepard, Donald (1968). „A Two-dimensional Interpolation Function for Irregularly-spaced Data“. In: *Proceedings of the 1968 23rd ACM National Conference*. ACM '68. New York, NY, USA: ACM, pp. 517–524 (cit. on p. 65).
- Slater, T., A. Shepherd, M. McMillan, A. Muir, L. Gilbert, A. E. Hogg, H. Konrad, and T. Parrinello (2018). „A new digital elevation model of Antarctica derived from CryoSat-2 altimetry“. In: *The Cryosphere* 12.4, pp. 1551–1562 (cit. on p. 1).
- Smith, B.E., H.A. Fricker, I. Joughin, and S. Tulaczyk (2009). „An inventory of active subglacial lakes in Antarctica detected by ICESat (2003–2008)“. In: *Journal of Glaciology* 55.192, pp. 573–595 (cit. on pp. 5, 87).
- Smith, W. H. F. and P. Wessel (1990). „Gridding with continuous curvature splines in tension“. In: *Geophysics* 55.3, pp. 293–305 (cit. on pp. 65, 69).
- Spedding, G. R. and E. Rignot (1993). „Performance analysis and application of grid interpolation techniques for fluid flows“. In: *Experiments in Fluids* 15.6, pp. 417–430 (cit. on p. 65).
- Stein, B. van, H. Wang, W. Kowalczyk, T. Bäck, and M. Emmerich (2015). „Optimally Weighted Cluster Kriging for Big Data Regression“. In: *Advances in Intelligent Data Analysis XIV*. Ed. by Elisa Fromont, Tjil De Bie, and Matthijs van Leeuwen. Cham: Springer International Publishing, pp. 310–321 (cit. on p. 65).
- Steinemann, S. (1954). „Results of Preliminary Experiments on the Plasticity of Ice Crystals“. In: *Journal of Glaciology* 2.16, pp. 404–416 (cit. on p. 17).
- Strozzi, T., A. Luckman, T. Murray, U. Wegmüller, and C.L. Werner (2002). „Glacier motion estimation using SAR offset-tracking procedures“. In: *IEEE Transactions on Geoscience and Remote Sensing* 40.11, pp. 2384–2391 (cit. on pp. 9, 56).
- Van Der Veen, C.J. and I.M. Whillans (1989). „Force Budget: I. Theory and Numerical Methods“. In: *Journal of Glaciology* 35.119, pp. 53–60 (cit. on p. 19).
- van Wessem, J. M. et al. (2014). „Improved representation of East Antarctic surface mass balance in a regional atmospheric climate model“. In: *Journal of Glaciology* 60.222, pp. 761–770 (cit. on p. 94).
- Vaughan, D.G., J.L. Bamber, M. Giovinetto, J. Russell, and A. P. R. Cooper (1999). „Reassessment of Net Surface Mass Balance in Antarctica“. In: *Journal of Climate* 12.4, pp. 933–946 (cit. on p. 1).
- Vaughan, D.G., J.C. Comiso, et al. (2013). „Observations: Cryosphere“. In: *Climate Change 2013: The Physical Science Basis. Contribution of Working Group I to the Fifth Assessment Report of the Intergovernmental Panel on Climate Change*. Ed. by T.F. Stocker, D. Qin, G.-K. Plattner, M. Tignor, S.K. Allen, J. Boschung, A. Nauels, Y. Xia, V. Bex, and P.M. Midgley. Cambridge, United Kingdom and New York, NY, USA: Cambridge University Press. Chap. 4, pp. 317–382 (cit. on pp. 1, 2).

- Vieli, Andreas and Antony J. Payne (2003). „Application of control methods for modelling the flow of Pine Island Glacier, West Antarctica“. In: *Annals of Glaciology* 36, pp. 197–204 (cit. on p. 31).
- Wang, G., D. Garcia, Y. Liu, R. de Jeu, and A.J. Dolman (2012). „A three-dimensional gap filling method for large geophysical datasets: Application to global satellite soil moisture observations“. In: *Environmental Modelling and Software* 30, pp. 139–142 (cit. on p. 63).
- WCRP Global Sea Level Budget Group (2018). „Global sea-level budget 1993–present“. In: *Earth System Science Data* 10.3, pp. 1551–1590 (cit. on p. 1).
- Weertman, J. (1957). „On the Sliding of Glaciers“. In: *Journal of Glaciology* 3.21, pp. 33–38 (cit. on p. 18).
- Weertman, J. and G. E. Birchfield (1983). „Subglacial Water flow Under Ice Streams and West Antarctic Ice-Sheet Stability“. In: *Annals of Glaciology, vol.3, pp.316-320* 3, pp. 316–320 (cit. on p. 18).
- Wegmüller, U., C. Werner, T. Strozzi, and A. Wiesmann (2006). „Ionospheric Electron Concentration Effects on SAR and INSAR“. In: *2006 IEEE International Symposium on Geoscience and Remote Sensing*, pp. 3731–3734 (cit. on p. 36).
- Wei, J., L. Shiyin, G. Wanqin, Y. Xiaojun, X. Junli, B. Weijia, and J. Zongli (2014). „Surface-area changes of glaciers in the Tibetan Plateau interior area since the 1970s using recent Landsat images and historical maps“. In: *Annals of Glaciology* 55.66, pp. 213–222 (cit. on p. 9).
- Wessel, P., W. H. F. Smith, R. Scharroo, J. Luis, and F. Wobbe (2013). „Generic Mapping Tools: Improved Version Released“. In: *Eos, Transactions American Geophysical Union* 94.45, pp. 409–410 (cit. on pp. 41, 66, 69).
- Yan, S., G. Liu, Y. Wang, and Z. Ruan (2015). „Accurate Determination of Glacier Surface Velocity Fields with a DEM-Assisted Pixel-Tracking Technique from SAR Imagery“. In: *Remote Sensing* 7.8, pp. 10898–10916 (cit. on p. 36).
- Zhao, C., R. M. Gladstone, R. C. Warner, M. A. King, T. Zwinger, and M. Morlighem (2018). „Basal friction of Fleming Glacier, Antarctica – Part 1: Sensitivity of inversion to temperature and bedrock uncertainty“. In: *The Cryosphere* 12.8, pp. 2637–2652 (cit. on p. 89).

List of Figures

1.1	Map of Antarctica	2
2.1	Map of the Filchner ice shelf region	5
5.1	Schematic glacier	26
6.1	Filter performance: artificial velocity field	40
6.2	Filter sensitivity to α	40
6.3	Three step filtering results of Recovery Glacier	42
6.4	Boxplots of Recovery Glacier test region filtering	43
6.5	Three step filtering results in a shear margin	44
6.6	Three step filtering results in a fast flowing region	45
6.7	Three step filtering results in a slow flowing region	46
6.8	Three step filtering results in a region with a line of outliers	47
6.9	Filter results of the Greenland Ice Sheet	48
6.10	Boxplots of the test regions in Greenland	49
6.11	Three step filtering results of Petermann Glacier	51
6.12	Three step filtering results of the NEGIS subset	52
6.13	Flowchart of the filter algorithm	57
6.14	Sensitivity of the filter to w	58
6.15	Sensitivity of the filter to a	59
6.16	Sensitivity of the filter to n_{min}	59
6.17	Sensitivity of the filter to ϵ_m	59
6.18	Sensitivity of the filter to $window_{dir}$	60
7.1	Interpolation of an artificial flow field	67
7.2	Input velocity field of Recovery Glacier	68
7.3	Interpolation errors	75
7.4	Histograms of interpolation errors	76
7.5	NatInt results of Recovery Glacier	77
7.6	Difference between NatInt and LinInt	77
7.7	MinCurv along the profile	78
7.8	Difference between NatInt and MinCurv	79
7.9	Results along the profile	80
7.10	Difference between NatInt and Kriging	80
7.11	Kriging variance	81

7.12	Close-up of results at Recovery Glacier	81
8.1	Overview map of the Recovery Glacier system	88
8.2	Overview map of Recovery Glacier with velocities	88
8.3	Basal topography	90
8.4	L-Curve	96
8.5	Modelled surface velocity	99
8.6	Difference in surface velocity magnitude	99
8.7	Basal friction coefficient	100
8.8	Basal drag coefficient	100
8.9	Driving stress and basal shear stress	102
8.10	Modelled basal velocity	103
8.11	Modelled slip ratio of surface to basal velocity	103
8.12	Basal velocity and basal drag coefficient superimposed on TerraSAR-X stripmap mode scenes	106
8.13	Shear margin	106
8.14	Difference in the basal drag coefficient between applying a filter to no filter	108
8.15	Difference in the basal drag coefficient between using a linear interpo- lation or natural neighbour interpolation	109
8.16	Sensitivity of the inversion on the enhancement factor	109
8.17	Sensitivity of the inversion on the basal drag coefficient	110
8.18	Effective normal pressure	110

List of Tables

6.1	Filter statistics	50
6.2	Number of data points before and after application of the filter	53
7.1	Characteristics of the four different methods.	73
7.2	Statistics of interpolation errors	74
7.3	Computational costs	75
7.4	Performance criteria	83

Affirmation in Lieu of an Oath

Versicherung an Eides Statt / *Affirmation in lieu of an oath*

gem. § 5 Abs. 5 der Promotionsordnung vom 15.07.2015 /
according to § 5 (5) of the Doctoral Degree Rules and Regulations of 15 July, 2015

Ich / I, _____
(Vorname / First Name, Name / Name, Anschrift / Address, ggf. Matr.-Nr. / student ID no., if applicable)

versichere an Eides Statt durch meine Unterschrift, dass ich die vorliegende Dissertation selbständig und ohne fremde Hilfe angefertigt und alle Stellen, die ich wörtlich dem Sinne nach aus Veröffentlichungen entnommen habe, als solche kenntlich gemacht habe, mich auch keiner anderen als der angegebenen Literatur oder sonstiger Hilfsmittel bedient habe und die zu Prüfungszwecken beigelegte elektronische Version (PDF) der Dissertation mit der abgegebenen gedruckten Version identisch ist. / *With my signature I affirm in lieu of an oath that I prepared the submitted dissertation independently and without illicit assistance from third parties, that I appropriately referenced any text or content from other sources, that I used only literature and resources listed in the dissertation, and that the electronic (PDF) and printed versions of the dissertation are identical.*

Ich versichere an Eides Statt, dass ich die vorgenannten Angaben nach bestem Wissen und Gewissen gemacht habe und dass die Angaben der Wahrheit entsprechen und ich nichts verschwiegen habe. / *I affirm in lieu of an oath that the information provided herein to the best of my knowledge is true and complete.*

Die Strafbarkeit einer falschen eidesstattlichen Versicherung ist mir bekannt, namentlich die Strafandrohung gemäß § 156 StGB bis zu drei Jahren Freiheitsstrafe oder Geldstrafe bei vorsätzlicher Begehung der Tat bzw. gemäß § 161 Abs. 1 StGB bis zu einem Jahr Freiheitsstrafe oder Geldstrafe bei fahrlässiger Begehung. / *I am aware that a false affidavit is a criminal offence which is punishable by law in accordance with § 156 of the German Criminal Code (StGB) with up to three years imprisonment or a fine in case of intention, or in accordance with § 161 (1) of the German Criminal Code with up to one year imprisonment or a fine in case of negligence.*

Ort / Place, Datum / Date

Unterschrift / Signature